IMPERIAL COLLEGE LONDON
Physics Department
Experimental Solid State Physics

Giuliana Di Martino

QUANTUM PLASMONICS: FROM QUANTUM STATISTICS TO QUANTUM INTERFERENCES

A Thesis presented for the Degree of Doctor of Philosophy of the University of London and the Diploma of Imperial College London

Supervisors:
Prof. S. Maier
Dr. Y. Sonnefraud

January 2014

Declaration of Originality

I hereby certify that the material presented in this thesis, which I now submitted for the award of Doctor of Philosophy of Imperial College London, is my own work unless otherwise cited or acknowledged within the body of the text.

Giuliana Di Martino

Copyright Declaration

The copyright of this thesis rests with the author and is made available under a Creative Commons Attribution Non-Commercial No Derivatives licence. Researchers are free to copy, distribute or transmit the thesis on the condition that they attribute it, that they do not use it for commercial purposes and that they do not alter, transform or build upon it. For any reuse or redistribution, researchers must make clear to others the licence terms of this work

Contents

Abstract **7**

Introduction **9**

1 Introduction to surface plasmon polaritons **13**

1.1 Surface plasmon polaritons at metal/insulator interface 14

1.2 Excitation of surface plasmon polaritons at planar interfaces . 17

1.2.1 Prism coupling 18

1.2.2 Excitation using high numerical aperture objectives . . 19

1.2.3 Near-field excitation 20

1.2.4 Grating coupling 20

1.3 Surface Plasmon Polariton Propagation Along Metal Stripes . 25

1.4 SPPs in the quantum regime: State of the art 27

2 Quantum optics and Quantum plasmonics **35**

2.1 Coherence in the classical and quantum regime 35

2.1.1 Classical coherence functions 36

2.1.2 Quantum coherence functions 38

2.1.3 Second-order coherence function $g^{(2)}(\tau)$ 40

2.2 Single photon sources 41

2.2.1 Spontaneous parametric down-conversion and heralded single photons 43

2.3 Quantization of surface plasma waves 45

2.3.1 Classical mode description 46

2.3.2 Discretization of classical modes 47

2.3.3 Quantization via the correspondence principle 47

2.4 Hong-Ou-Mandel interferometer 48
2.4.1 Photonic bunching 49

3 Experimental details **55**
3.1 Single photon source 55
3.1.1 Description of the source 55
3.1.2 Alignment procedure 57
3.2 The samples 60
3.2.1 Fabrication 63
3.2.2 Propagation length 63
3.2.3 Grating characterization 65
3.2.4 Splitting characterization 66

4 Results and Discussions **71**
4.1 Quantum Statistics of Surface Plasmon Polaritons in Metallic Stripe Waveguides 71
4.1.1 Experimental setup 71
4.1.2 Experimental measurement of $g^{(2)}(\tau)$ 72
4.1.3 Characterization of the effects of loss on the quantum statistics of waveguided SPPs 74
4.1.4 Fock state population tomography 78
4.1.5 Conclusions 81
4.2 Quantum interference in the plasmonic Hong-Ou-Mandel effect 82
4.2.1 HOM dip experiment in free space 82
4.2.2 Plasmonic HOM dip experiment 86
4.2.3 Conclusions 96

5 Conclusions and Future work **98**

Bibliography **101**

Appendices **111**

List of publications

Portions of this thesis have been drawn from the following publications and manuscripts:

Di Martino, Giuliana; Sonnefraud, Yannick; Tame, Mark; Kéna-Cohen, Stéphane; Dielman, Frederick; Ozdemir, Sahin; Kim, Myungshik; Maier, Stefan. *Observation of quantum interference in the plasmonic Hong-Ou-Mandel effect.* Submitted (2013)

Vercruysse, Dries; Sonnefraud, Yannick; Verellen, Niels; Fuchs, Fabian; Di Martino, Giuliana; Lagae, Liesbet; Moshchalkov, Victor; Maier, Stefan; Van Dorpe, Pol. *Unidirectional Side Scattering of Light by a Single-Element Nanoantenna.* Nano Lett. 13, 3843-3849(2013)

Di Martino, Giuliana; Sonnefraud, Yannick; Kéna-Cohen, Stéphane; Tame, Mark; Ozdemir, Sahin; Kim, Myungshik; Maier, Stefan. *Quantum statistics of surface plasmons in metallic stripe waveguides.* Nano Lett. 12, 2504-2508 (2012)

Sonnefraud, Yannick; Kerman, Sarp; Di Martino, Giuliana; Lei, Dang Yuan; Maier, Stefan. *Directional excitation of surface plasmon polaritons via*

nanoslits under varied incidence observed using leakage radiation microscopy. Optics Express, Vol. 20, Iss. 5, pp. 4893-4902 (2012)

Abstract

In this thesis, we focus our attention on the excitation of Surface Plasmon Polaritons (SPPs) and their propagation along metal stripes. Plasmons are characterized by losses into the metal, therefore an important step is to investigate the effect of these losses on their quantum properties. This is a field not yet fully investigated and the work presented here will give us the possibility to understand the effect of losses on the plasmons quantum properties. This will allow us to prove that plasmons can be used in the quantum information technology field, since they keep the quantum information regardless of their lossy character.

Another key property yet to be fully investigated is the bosonic character of single surface plasmon polaritons (SPPs). The quasi-particle nature of SPPs, consisting of a photon (boson) coupled to a charge density wave of electrons (fermions), makes them an unusual type of quantum excitation. It is, as of yet, unclear whether SPPs are bosons, fermions, or a hybrid mixture [1]. Here, we will prove the bosonic character of plasmons, making use of interference experiments. This study will open opportunities for controlling quantum states of light in ultra-compact nanophotonic plasmonic circuitry.

First of all, the mean excitation rates, intensity correlations and Fock state populations are studied by using heralded single photons generated via spontaneous parametric down conversion as sources of light. One downconverted beam is used as a trigger, the other one is the signal we send to the metal stripes to excite the plasmons. After an introduction on the meaning of coherence functions, we explain how we couple photons into a gold waveguide with gratings on both sides, where the coupled plasmon is confined at the interface between gold and air. By measuring the second-order quantum

coherence function $g^2(t)$, we demonstrated the ability to excite single SPPs. Moreover, the effect of losses incurred during propagation of the single SPPs is consistent with the classical exponential behaviour and does not change the value of $g^2(t)$, providing evidence that a linear uncorrelated Markovian loss model is valid for SPP damping at the single quanta level.

Then, we move onto more complicated devices, such as X-shaped stripes that act as a plasmonic beamsplitter, in order to observe nonclassical effects in the interference of two single plasmons. This is an important step along the way to understanding better the behaviour of single surface plasmons at the quantum level and how one can build more complicated quantum interference networks, such as plasmonic-based quantum logic gates. In order to fully verify the bosonic nature of single excitations in the quantum regime it is vital to observe quantum interference. A natural thing to probe in the most basic type of scatterer (a 50/50 beamsplitter) operating in the quantum regime, is how it acts on two separate single surface plasmons. Here the launching method is the same as for the previous experiment, except that the waveguide structure is in the form of a 50/50 beamsplitter (X-shape) and both photons from the parametric down-conversion type-I generation are sent onto the two inputs of the plasmonic beamsplitter. By this way, both the beams, generated by the nonlinear crystal, act as signal beams.

If the SPPs are truly bosonic and indistinguishable then they tend to bunch together when they interact at the beamsplitter -this is the well-known Hong-Ou and Mandel quantum interference effect. In this work we report the first direct observation of quantum interference in the HOM effect for single SPPs, demonstrating by this way the bosonic nature of plasmons.

Introduction

Since its formulation in the early 1920's, quantum mechanics has played a fundamental role in our understanding of how Nature behaves on the microscopic scale and smaller. 'Puzzling' and 'non-intuitive' are words that were often used by scientists to describe quantum theory when it was first proposed and these sentiments are still held by researchers in the field of quantum physics today. However, compelling evidence for its correctness has been found over the last century in the form of its predictive power in a wide range of experimental settings. It has been successful in explaining many physical phenomena, such as experiments probing the structure of the atom during the 1930's, nuclear fusion in stars in the late 1930's, the behaviour of elementary particles since the 1940's and superconductors since the 1950's, to name only a few examples. Quantum mechanics is in essence a mathematical framework or set of rules that can be applied in order to describe a given physical system. Its use is not always necessary and depends on various factors such as the scale of the system and how well it is isolated from everything else. Since the 1970's, the ability to investigate the behaviour of single quantum systems has become possible. Scientists have developed the capability to control and manipulate these systems with numerous methods in a range of different experimental setups. The invention of the Laser [2] and its development over the years has played a crucial role in this. Techniques such as trapping single atoms in 'atom traps' [3–9] have allowed atoms to be isolated from the rest of the world and their individual behaviour to be studied by probing with laser light. Devices that enable the transfer of single electrons [10, 11] and photons (quanta of light) [12] have also been demonstrated experimentally with great success. These advances

have stimulated theoretical interest in the use of quantum controlled devices for investigating and probing deeper into the intricate features of quantum physics. This interest, together with the development of quantum mechanics from a new information-theoretic point of view, has led physicists to the possibility of using quantum-based devices for carrying out information processing tasks. Technologies such as quantum computing (QC) and quantum cryptography have also emerged, offering unique advantages over their classical (non-quantum) counterparts. These advantages include a vast decrease in the running time of various mathematical algorithms and significantly higher levels of security for communication. The properties of quantum physics that at first seemed strange and rather curious to its founders are now being exploited in the design of novel schemes for quantum information protocols. The development of quantum information theory has also led to new fundamental insights into quantum physics itself, such as the roles of entanglement (quantum correlations) and measurements in the dynamics of quantum systems, both isolated and in contact with the rest of the world. Apart from the potential advantages quantum information processing (QIP) offers, there are practical reasons why microscopic scale information protocols based on quantum mechanics are needed. In 1965 Moore predicted [13] that the number of transistors per integrated circuit (for minimum component cost) would double every two years. This rate has now been maintained for over 40 years, with the size of the transistors becoming smaller and smaller. There will come a point, within the next decade, when quantum effects in the circuits will be unavoidable. It was first recognised by Benioff [14–16] in the early 1980's that quantum mechanical computational processes could be at least as powerful as classical computational processes. Around the same time, Feynman [17] suggested that computers based on the principles of quantum mechanics could actually overcome the essential difficulties faced when trying to simulate complex quantum systems on classical computers. In 1985, Deutsch [18] was naturally led to consider computational devices based on the framework of quantum mechanics. This work, together with Benioff's and Feynman's insights, laid the foundations of modern-day quantum computing.

The great progress of quantum cryptography is due largely to the minimal quantum resources that the protocols require. Quantum computing on the other hand requires much larger resources for performing its algorithms and numerous problems still need to be overcome, both at the experimental and theoretical level. From an experimental perspective, physically scalable qubit systems need to be identified and developed. The systems also need to allow universal sets of operations to be implemented and have the ability to initialise and read out the information being processed [19]. Unavoidable errors occur in many places in quantum systems. Effects such as decoherence (environment-induced noise) and the imperfect operation of key components in the setup act to destroy or modify the quantum information in a way that produces undesired protocol outcomes. However, it remains to be seen how these methods can be implemented in practice, given the high demand of control and isolation that even small quantum resources require. Scaling to larger resources in order to perform more computationally useful tasks also increases the quantum system's susceptibility to imperfections. There is still much work to be done before QC can be put to practical use.

It is in this framework that a new and very promising field can be introduced. Quantum plasmonics is a rapidly growing field of research that involves the study of the quantum properties of light and its interaction with matter at the nanoscale. Here, surface plasmons - electromagnetic excitations coupled to electron charge density waves on metal-dielectric interfaces or localized on metallic nanostructures - enable the confinement of light to scales far below that of conventional optics. Nanophotonic systems based on plasmonic components are currently attracting considerable attention due to the novel ways in which the electromagnetic field can be localised and controlled [20, 21]. In the classical regime, a wide range of applications are being actively pursued, including near-field nano-imaging [22], biosensing [23] and solar cells [24]. Recently, researchers have also started to investigate plasmonics in the quantum regime [25]. Devices have been proposed for a variety of applications in quantum information science such as single-photon sources [26], transistors [27] and ultra-compact quantum circuitry [28].

Despite the significant progress made so far, there are many fundamental aspects of quantum plasmonic systems that remain unexplored. Plasmons are characterized by losses into the metal, therefore a crucial step is to investigate the effect of these losses on their quantum properties. This is a field not yet fully investigated and the work presented here will give us the possibility to understand the effect of losses on the plasmons quantum properties. This will show that plasmons can be used in the quantum information technology field, since they keep the quantum information regardless their lossy character.

Another key property yet to be fully investigated is the bosonic character of single surface plasmon polaritons (SPPs). The quasi-particle nature of SPPs, consisting of a photon (boson) coupled to a charge density wave of electrons (fermions), makes them an unusual type of quantum excitation. It is, as of yet, unclear whether SPPs are bosons, fermions, or a hybrid mixture [1]. Here, we will prove the bosonic character of plasmons, making use of interferences experiments. This study will open opportunities for controlling quantum states of light in ultra-compact nanophotonic plasmonic circuitry.

We will structure this thesis as follow. First, an introduction to the main concepts of plasmonics is given. Here, we illustrate the distinctive potentiality which can come from the use of plasmonics. A brief overview of plasmonic basic physical concepts is given, starting from the excitation of surface plasmon polaritons at planar interfaces till surface plasmon polariton propagation along metal stripes.

Then, an overview on quantum photonics and quantum plasmonics is presented. This will give to the reader some tools to go through the following core chapters where we present the results of this PhD project: our findings on quantum statistics of surface plasmon polaritons in metallic stripe waveguides, and our results on quantum interference in the plasmonic Hong-Ou-Mandel effect.

Chapter 1

Introduction to surface plasmon polaritons

The term 'plasmonics' was coined just about a decade ago to describe a promising new device technology that aims to exploit the unique optical properties of metallic nanostructures to enable routing and active manipulation of photons at the nanoscale.

Plasmonics can play an important role in future device technologies as illustrated in Figure 1.1. The different domains in terms of operating speed and device sizes rely on the unique material properties of semiconductors (electronics), insulators (photonics), and metals (plasmonics). Semiconductor electronics is limited in speed, dielectric photonics is limited in size by the fundamental laws of diffraction. Plasmonics can serve as a bridge between photonics and nanoelectronics. The electrical properties of semiconductors enable the realization of truly nanoscale elements for computation and information storage. The high transparency of dielectrics facilitates information transport over long distances and at incredible data rates. Plasmonics offers the opportunity to combine the size of nanoelectronics and the speed of dielectric photonics, enabling devices that might naturally interface with similar-speed photonic devices and with similar-size electronic components, thus enhancing the synergy between these technologies.

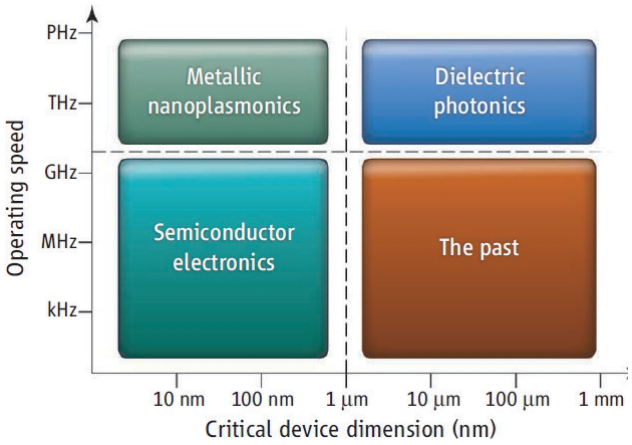


Figure 1.1: Devices dimention vs. operating speed. The dashed lines indicate physical limitations of different technologies; semiconductor electronics is limited in speed by heat generation and interconnect delay time issues to about 10 GHz. Dielectric photonics is limited in size by the fundamental laws of diffraction. Plasmonics can serve as a bridge between photonics and nanoelectronics. [29]

1.1 Surface plasmon polaritons at metal/insulator interface

Surface plasmon polaritons are electromagnetic excitations propagating at the interface between a dielectric and a conductor, evanescently confined in the direction perpendicular to the interface. These electromagnetic surface waves arise via the coupling of the electromagnetic fields to oscillations of the conductor's electron plasma. Surface plasmons propagate along the interface with electromagnetic fields, energy and charges highly localized and possessing maximum intensity at the interface, as shown in Figure 1.2. These properties depend strongly on the optical properties of both the metal (complex dielectric function, corrugations, roughness) and the dielectric (refractive index). At the base of our following discussions, we will always find the fundamental wave equation for the electric field $\mathbf{E}$:

$$\nabla^2\mathbf{E} = -\frac{\epsilon}{c^2}\frac{\partial^2\mathbf{E}}{\partial t^2} = 0 \tag{1.1}$$

with ϵ the dielectric constant of the medium in which the wave propagates. Practically, this equation has to be solved separately in regions of constant ϵ, and the solutions obtained have to be matched using appropriate boundary

conditions. We can now assume in all generality a harmonic time dependence $\mathbf{E}(\mathbf{r},t) = \mathbf{E}(\mathbf{r})e^{-i\omega t}$ of the electric field. Inserted into eq.1.1, this yields:

$$\nabla^2 + k_0^2 \epsilon \mathbf{E} = 0 \tag{1.2}$$

where $k_0 = \frac{\omega}{c}$ is the wave vector of the propagating wave in vacuum.

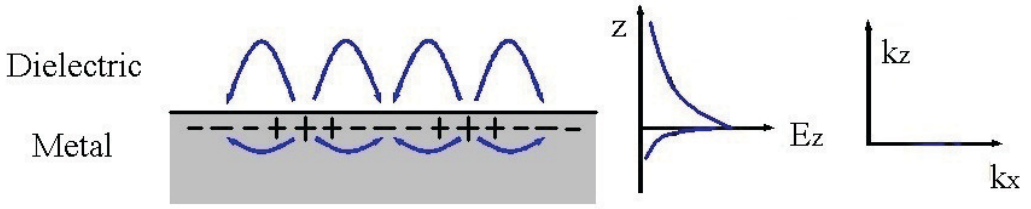


Figure 1.2: The charges and the electromagnetic field of surface plasmons propagating on a surface in the x direction. The exponential dependence of the field E_z is seen on the right [30].

For waves that propagate along the x-direction of a cartesian coordinate system (see Figure 1.2), and show no spatial variation in the perpendicular, in-plane y-direction, the frequency ω of these longitudinal oscillations is tied to its wave vector k_x by a dispersion relation $\omega(k_x)$ [30]. The field is described by

$$\mathbf{E} = E_0^{\pm} exp[+i(k_x x \pm k_z - \omega t)] \tag{1.3}$$

with + for $z > 0$, - for $z < 0$ and with imaginary k_z which causes the exponential decay of the field E_z. The complex parameter k_x is called the *propagation constant* of the traveling waves and corresponds to the component of the wave vector in the direction of propagation; $k_x = 2\pi/\lambda_p$, where λ_p is the wavelength of the plasma oscillation. Inserting this expression into eq.1.2 yields the desired form of the wave equation

$$\frac{\partial^2 E(z)}{\partial z^2} + (k_0^2 \epsilon - k_x^2)\mathbf{E} = 0 \tag{1.4}$$

Naturally, a similar equation exists for the magnetic field $\mathbf{H}$.

It can easily be shown [31] that this system allows two sets of self-consistent solutions with different polarization properties of the propagating waves. The first set are the transverse magnetic (TM or p) modes, where

only the field components E_x , E_z and H_y are nonzero, and the second set the transverse electric (TE or s) modes, with only H_x , H_z and E_y being nonzero.

For the TM modes we have

$$E_x = -i\frac{1}{\omega\epsilon_0\epsilon}\frac{\partial H_y}{\partial z} \tag{1.5}$$

$$E_z = -\frac{k_x}{\omega\epsilon_0\epsilon}H_y \tag{1.6}$$

and the wave equation for the TM modes is

$$\frac{\partial^2 H_y}{\partial z^2} + (k_0^2\epsilon - k_x^2)H_y = 0 \tag{1.7}$$

For the TE modes we have

$$H_x = i\frac{1}{\omega\mu_0}\frac{\partial E_y}{\partial z} \tag{1.8}$$

$$H_z = -\frac{k_x}{\omega\mu_0}E_y \tag{1.9}$$

and the wave equation for the TE modes is

$$\frac{\partial^2 E_y}{\partial z^2} + (k_0^2\epsilon - k_x^2)E_y = 0 \tag{1.10}$$

Now we consider a plane surface of a semi-infinite metal with the complex dielectric function $\epsilon_1 = \epsilon_1' + i\epsilon_1''$, adjacent to a medium ϵ_2 as air or vacuum.

From the solutions of the TM modes, the continuity of H_y and $\epsilon_i E_z$ at the interface requires that

$$\frac{k_{z1}}{\epsilon_1} + \frac{k_{z2}}{\epsilon_2} = 0 \tag{1.11}$$

$$\epsilon_i\left(\frac{\omega}{c}\right)^2 = k_x^2 + k_{zi}^2 \quad or \quad k_{zi} = \left[\epsilon_i\left(\frac{\omega}{c}\right)^2 - k_x^2\right]^{1/2} \tag{1.12}$$

The dispersion relation (1.11) can be written as

$$k_x = \frac{\omega}{c}\left(\frac{\epsilon_1\epsilon_2}{\epsilon_1+\epsilon_2}\right)^{1/2} \tag{1.13}$$

If we assume besides a real ω and ϵ_2 that $\epsilon_1'' < |\epsilon_1'|$ [30], we obtain a complex $k_x = k_x' + ik_x''$ with

$$k_x' = \frac{\omega}{c}\left(\frac{\epsilon_1'\epsilon_2}{\epsilon_1'+\epsilon_2}\right)^{1/2} \tag{1.14}$$

$$k_x'' = \frac{\omega}{c}\left(\frac{\epsilon_1'\epsilon_2}{\epsilon_1'+\epsilon_2}\right)^{3/2}\frac{\epsilon_1''}{2(\epsilon_1')^2} \tag{1.15}$$

We now briefly analyze the possibility of TE surface modes. Continuity of E_y and H_x at the interface leads to the condition

$$A(k_1 + k_2) = 0 \tag{1.16}$$

with A being a constant. Since confinement to the surface requires $Re[k_1] > 0$ and $Re[k_2] > 0$, this condition is only fulfilled if $A = 0$. Thus, no surface modes exist for TE polarization. Surface plasmon polaritons only exist for TM polarization.

Let us analyze the spatial extension of the SP fields. Wave vectors k_{z2} and k_{z1} are imaginary due to the relations $\omega/c < k_x$ and $\epsilon_1' < 0$ (see eq.1.12), so that the field amplitude of the SPs decreases exponentially as $exp(-|k_{zi}|\,|z|)$, normal to the surface. The value of the depth at which the field falls to 1/e becomes

$$z = \frac{1}{|k_{zi}|}\ or \tag{1.17}$$

$$\begin{aligned} in\ the\ medium\ with\ \epsilon_2: \quad z_2 &= \frac{\lambda}{2\pi}\left(\frac{\epsilon_1'+\epsilon_2}{\epsilon_2^2}\right)^{1/2} \\ in\ the\ medium\ with\ \epsilon_1: \quad z_1 &= \frac{\lambda}{2\pi}\left(\frac{\epsilon_1'+\epsilon_2}{\epsilon_2'^2}\right)^{1/2} \end{aligned} \tag{1.18}$$

The intensity of SPs propagating along a smooth surface decreases as $e^{-2k_x''x}$ with k_x'' from (1.15). The length L_i after which the intensity decreases to 1/e is given by

$$L_i = (2k_x''x)^{-1} \tag{1.19}$$

More detailed informations can be found in [30].

1.2 Excitation of surface plasmon polaritons at planar interfaces

Confinement is achieved since the propagation constant β is greater than the wave vector k in the dielectric, leading to evanescent decay on both sides of the interface. The application of photons to excite surface plasmons meets

the difficulty that at a given photon energy $\hbar\omega$ the wave vector $\hbar\omega/c$ has to be increased by a Δk_x value in order to couple the photons into surface plasmons. In the following sections we will give a brief overview of the different coupling techniques, and lastly, we will focus our attention on the one we used for our project: the so called *grating coupling*.

1.2.1 Prism coupling

Surface plasmon polaritons on a flat metal/dielectric interface cannot be excited directly by light beams since $\beta > k$, where k is the wave vector of light on the dielectric side of the interface. Therefore, the projection along the interface of the momentum $k_x = ksin\theta$ of photons impinging under an angle θ to the surface normal is always smaller than the SPP propagation constant β, even at grazing incidence, prohibiting phase-matching. However, phase-matching to SPPs can be achieved in a three-layer system consisting of a thin metal film sandwitched between two insulators of different dielectric constants. For simplicity, we will take one of the insulators to be air ($\epsilon = 1$). A beam reflected at the interface between the insulator of higher dielectric constant ϵ, usually in the form of a prism (Figure 1.3). This cou-

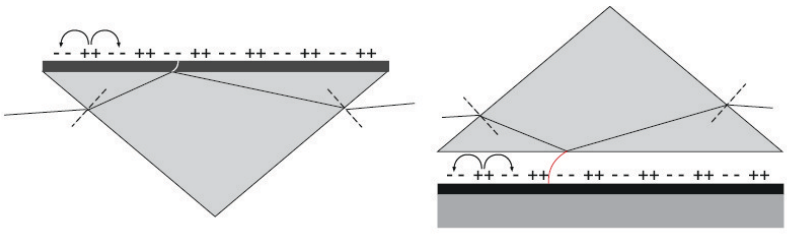


Figure 1.3: Prism coupling to SPPs using attenuated total internal reflection in the Kretschmann (left) and Otto (right) configuration. Also drawn are possible light paths for excitation [31].

pling scheme - also known as attenuated total internal reflection - therefore involves tunneling of the fields of the excitation beam to the metal/air interface where SPP excitation takes place. Two different geometries for prism coupling are possible, depicted in Figure 1.3. The most common configuration is the Kretschmann method [32], in which a thin metal film is evaporated on top of a glass prism. Photons from a beam impinging from the glass side

at an angle greater than the critical angle of total internal reflection tunnel through the metal film and excite SPPs at the metal/air interface. Another geometry is the Otto configuration [33], in which the prism is separated from the metal film by a thin air gap. Total internal reflection takes place at the prism/air interface, exciting SPPs via tunneling to the air/metal interface. This configuration is preferable when direct contact with the metal surface is undesirable, for example for studies of surface quality. We want to stress that SPPs excited using phase-matching via $\beta = k\sqrt{\epsilon}\sin\,\theta$ are inherently leaky waves, i.e. they lose energy not only due to the inherent absorption inside the metal, but also due to leakage of radiation into the prism.

1.2.2 Excitation using high numerical aperture objectives

As a variant of the traditional prism coupling technique, a microscope objective of high numerical aperture can be used for SPP excitation. Fig 1.4 shows a typical setup. An oil-immersion objective is brought into contact with the glass substrate (of refractive index n) of a thin metal film via a layer of index-matched immersion oil. The high numerical aperture of the objective ensures a large angular spread of the focused excitation beam, including angles $\theta > \theta_c$ greater than the critical angle of total internal reflection at a glass/air interface. This way, wave vectors $k_x = \beta$ are available for phase-matching to SPPs at the metal/air interface at the corresponding angle $\theta_{SPP} = \arcsin(\beta/nk_0) > \theta_c$. The excited SPPs will radiate back into

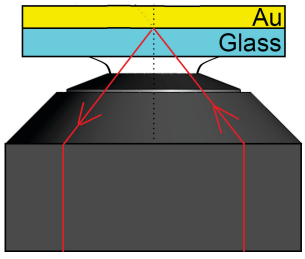


Figure 1.4: Schematic of the excitation with a light beam of SPPs and their observation via detection of the leakage radiation using an index-matched oil immersion lens.

the glass substrate in the form of leakage radiation at an angle $\theta_{SPP} > \theta_c$,

which can be collected through the immersion oil layer via the objective [34].

1.2.3 Near-field excitation

Excitation schemes such as prism or grating coupling excite SPPs over a macroscopic area defined by the dimensions of the (at best diffraction-limited) spot of the coupling beam of wavelength λ_0. In contrast, near-field optical microscopy techniques allow for the local excitation of SPPs over an area $a << \lambda_0$. A small probe tip of aperture size $a \leq \lambda_{SPP} \leq \lambda_0$ illuminates the surface of a metal film in the near field. Due to the small aperture size, the light going through the tip will contain larger wave vector components $k \geq \beta \geq k_0$, thus allowing phase-matched excitation of SPPs with propagation constant β. Due to the ease of lateral positioning of such probes in scanning near-field optical microscopes, SPPs at different locations of the metal surface can be excited [35].

1.2.4 Grating coupling

The grating coupling is a technique used largely in the plasmonics community, for its simplicity of fabrication and implementation in optical alignments. Here we will describe how this technique works.

Infinite grating

The mismatch in wave vector between the in-plane momentum of impinging photons and the propagation constant of the plasmon k_x can also be overcome by patterning the metal surface with a shallow grating of grooves or holes with lattice constant a. For the simple grating of grooves depicted in Figure 1.5, the coupling of the photon into a plasmon takes place whenever the condition

$$k_x = k\ sin\Theta \pm \nu g \tag{1.20}$$

is fulfilled, where Θ is defined as in Figure 1.5, $g = \frac{2\pi}{a}$ is the reciprocal vector of the grating and $\nu = (1, 2, 3...)$. The reverse process can also take place: SPPs propagating along a surface modulated with a grating can couple to light and thus radiate.

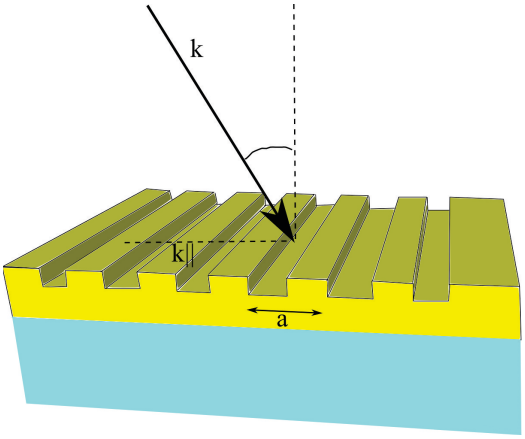


Figure 1.5: Phase-matching of light to SPPs using a grating.

Single ridge scattering

Ideally we would like to maximize the amount of light converted into plasmons, enabling an efficient grating coupling. In order to achieve this target, different grating parameters need to be studied. The first investigation of the coupling efficiency of surface plasmon polaritons on a gold film by a grating of gold ridges was done with a leakage radiation set-up by Ditlbacher et al.[36]. They investigate the light/SPP coupling efficiency for single ridges and ensembles of three parallel oriented ridges separated by the (center-to-center) distance Λ. In a simple set-up they measured the leakage radiation from SPPs excited on 1 and 3 ridges on a gold film illuminated by a laser with $\lambda_0 = 800$ nm and full width half maximum beam diameter of $1\mu m$ with a sensitivity calibrated photodiode. The exciting laser is focused with an intensity profile of a Gaussian shape.

In Figure 1.6 we report the results of Ditlbacher et al.[36], where the SPPs leakage radiation profiles for different grating structures, which extend over a distance y, are shown. The measured intensity of the total structure can be modeled as a coherent sum of the three ridges. The similarity between the experiments and the theory, see Figure 1.6, is a strong indication that this idea of coherent interference of the SPPs excited at different ridges is a solid one and, therefore, constructive interference of locally excited SPPs at the different ridges creates an efficient light-plasmon coupling.

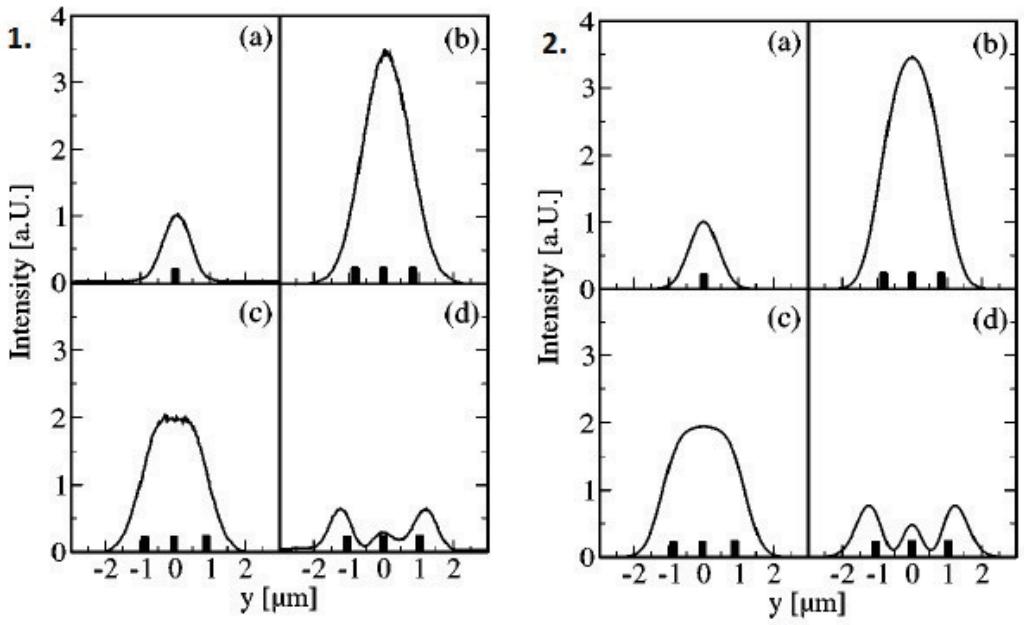


Figure 1.6: Comparison between 1, experimental and 2, calculated leakage radiation profiles. In both: (a) single ridge, (b) Λ= 780nm, (c) Λ= 900nm, (d) Λ= 1110nm. The results are normalized such that (a) peaks at 1 [36].

Grating parameters

After this rather simple evidence for the coherent excitation of SPPs on a grating, it is important to get an idea of the optimum shape of the grating and the influence of experimental parameters, for example the illumination spot size and position. A monochromatic beam focused on the sample at normal incidence is considered. Because of the TM dependency of surface plasmon propagation, the electric field has to be polarized perpendicularly to the ridges, the SPPs only propagate in the direction of the electric field[37].

A first step in finding the optimal grating structure is finding the preferred height and width of a single ridge. Then, more scattering from each ridge separately will create a higher output from the coherent interference from the different ridges of the grating. A basic description of the scattering on a single ridge is one in which the ridge is considered acting as a subwavelenght dipole along its height. This means that a stronger interaction for shorter wavelengths is expected, since pure dipole scattering has a λ^{-4} dependency [38, 39]. In Figure 1.7, concerning gold ridges on a single interface with λ_0

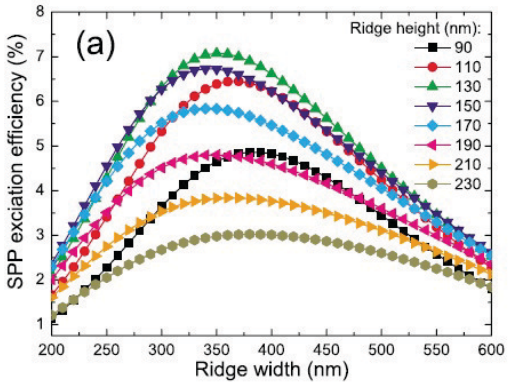


Figure 1.7: Calculation of efficiency of SPP excitation on a single ridge versus its width, free space wavelength is 800 nm[38].

= 800 nm, we see the strong dependence of the SPP excitation efficiency on both the ridge height as the ridge width. The optimum ridge width does not seem to depend on the height of it, and is always around 350 nm, so close to half the wavelength [38]. In ref.[40] the authors suggest similar widths, with duty cycles values, the ratio of the ridge width to the period of the grating, around 0.5.

To estimate the coupling efficiency Radko et al. [38] measure the leakage radiation from the SPP into the glass substrate where the gold structures have been deposited. The coupling efficiency is calculated from the ratio between the SPP intensity and the laser intensity. Figure 1.8 (a), period Λ = 800 nm, shows the advantage of using a grating over a single ridge. The efficiency goes from 2-3 % to values close to 20 % for the correct wavelength. The unidirectional efficiency is the ratio of the SPP intensity propagating in one chosen direction and the incoming light intensity. The graph also shows the great importance of the wavelength, the efficiency goes up only when the plasmons excited from different ridges interfere constructively. Another important factor for the experiments is the influence of the position of the exciting beam on the grating, as shown in Figure 1.8 (b). The grating extends approximately from x = 3 μ m to x = 11 μ m, the efficiency exhibits a sharp peak when the beam is focussed at the end of the grating, it is thus highly sensitive to the position of the laser beam, creating another experimental difficulty. For the wavelengths out of resonance, such as λ_0 = 730 nm, the

spot even needs to be focused partly next to the grating to get the maximum efficiency. This can be understood by the negative influence of destructive interference from too many ridges, also visible in Figure 1.8 (a). The main aspects that thus need to be taken into consideration when using the grating for the excitation of surface plasmon polaritons are the size of the beam spot, its position and direction compared to the normal of the surface. The

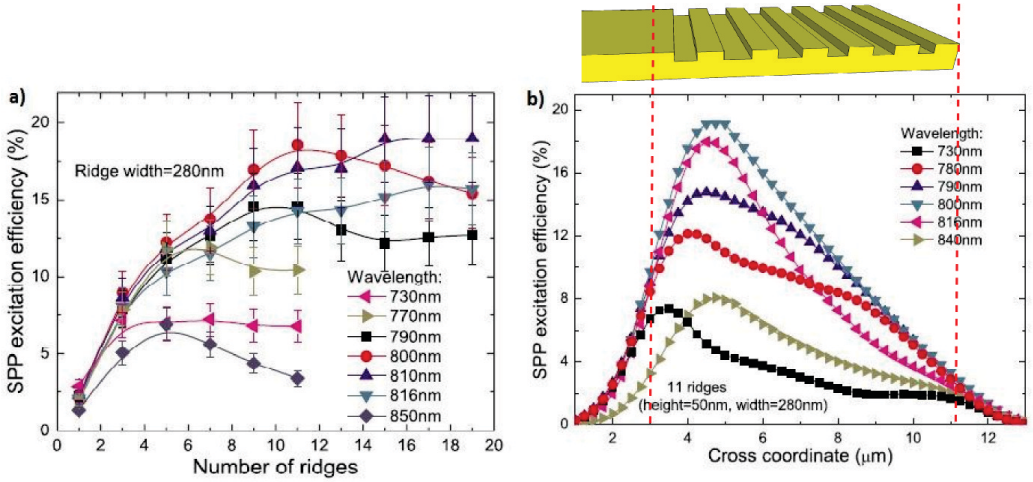


Figure 1.8: SPP coupling efficiency. (a) Experimental measurements of efficiency of SPP excitation versus the number of ridges in the grating (Λ = 800 nm), with height = 50 nm and width = 280 nm. (b) Experimental measurements for SPP excitation efficiency versus the position of a laser beam scanned over the grating, Λ = 800 nm. [38]

previous results by Radko et al. [38] considered λ_{SPP} to be the same as on a smooth surface. Due to this, the best free space wavelength had a value close to the grating period, λ_0 = 810 nm for Λ = 800 nm. While this is a good approximation for surfaces with small modulations, the dispersion relation shifts considerably for deep modulations, like high ridges. It turns out that for a fixed free space wavelength, the SPP wavelength becomes shorter for a deep modulation or a high roughness of the metal surface. In the same amount, the spectral width of the resonance becomes wider [30, 40, 41].

In light of those considerations, in our experiment, the coupling efficiency of our gratings has been maximized by always using 11-ridges gratings, and by focusing the incoming beam close to the edge of the grating.

1.3 Surface Plasmon Polariton Propagation Along Metal Stripes

In this section we will present a number of studies of coupled SPP modes guided along metallic stripes of finite width. We will restrict our discussions to waveguides of cross sections with $\omega/t >> 1$, where only the vertical dimension t is sub-wavelength (see sketch in Figure 1.9). The purely bound

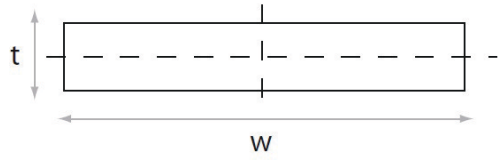


Figure 1.9: Cross section of a metal stripe waveguide of finite width.

electromagnetic modes of propagation supported by symmetric wave guide structures comprised of a thin lossy metal film of finite width embedded in an infinite homogeneous dielectric have been characterized at optical wavelengths in [42].

In [43] a photon scanning tunneling microscope is used to probe the field of surface plasmon polariton modes excited on finite-width thin metal films (metal stripes). It is shown that, if the width of the metal stripe is a few micrometers, a strong coupling with the stripe modes can be achieved at visible frequencies.

In [44] thin gold stripes, featuring various widths in the micrometer range, were fabricated to obtain surface plasmon guides on a glass substrate. For a fixed frequency of the incident light, the field distribution of the SPP modes are found to depend on the widths of the stripes. Here, similarity of the intensity distributions has been recorded over metal stripes having the same width but different thickness. This result supports the evidence that the field of the metal stripe modes is mostly localized at the upper interface (metal/air).

This result can also be seen from the field profile at the interface. In Figure 1.10 we calculated it for a 70nm thick gold stripe on glass substrate.

Electric field profile along the cross section of the waveguide calculated using the Finite Element Method (FEM) for an infinitely long waveguide. It is evident that the electric field is mostly localized at the upper interface, which in this particular case is air.

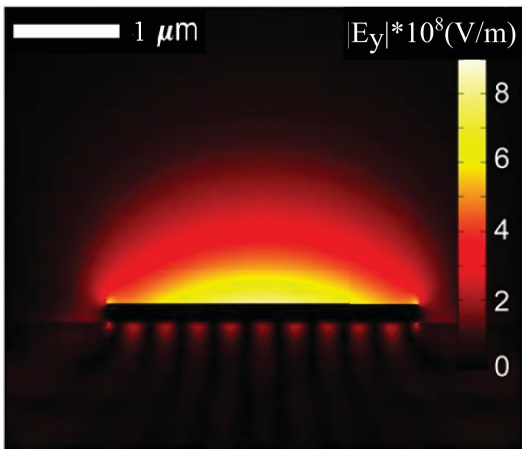


Figure 1.10: Fundamental SPP in a 70nm thick gold stripe on glass substrate. Electric field profile along the cross section of the waveguide calculated using the FEM for an infinitely long waveguide.

In [45] a series of near-field experiments on plasmon modes supported by Au stripes on glass substrates is presented. These studies demonstrate that the propagation of light along surface plasmon waveguides is mediated by a discrete number of guided polariton modes as well as a continuum of radiation modes. To distinguish the contribution of the guided modes from that of the radiation continuum, a parametric study of propagation length as a function of varying stripe width is performed. In [45] the authors have mapped the propagation of light along varying width Au stripes on glass substrates. It appears that the propagation length observed decreases as a function of decreasing stripe width. A metal stripe waveguide can support a finite number of guided modes. While wide stripes may support multiple guided modes, narrower stripes may support none [45].

In light of those considerations, in our experiment, we have designed the width of our gold waveguides so that only one mode, the fundamental one, is supported (see section 3.2 for more details).

1.4 SPPs in the quantum regime: State of the art

Surface plasmon polaritons have the potential to interface electronic and optical devices. They could prove extremely useful for integrated quantum information processing.

Recent work has shown that SPPs can maintain certain quantum properties of their exciting photon field, with the demonstration of assisted transmission of entangled photons [46, 47], sub-Poissonian statistics [26], energy-time entanglement [48], quantum superposition [49], quadrature squeezing [50], wave-particle duality [51], and single plasmon detection [52]. These results suggest that many principles of quantum optics can be transferred to the field of plasmonics, enabling novel devices, such as single photon switches, to be realized [27].

In [53] the authors described a new all-electrical SPP detection technique based on the near-field coupling between guided plasmons and a nanowire field-effect transistor. They used the technique to electrically detect the

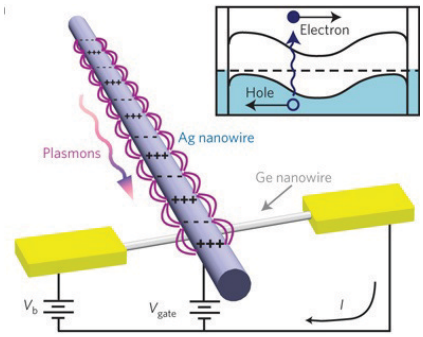


Figure 1.11: Schematic diagram of electrical plasmon detector operation. Inset: Electron-hole pair generation and separation in the Ge nanowire detector.[53]

plasmon emission from an individual colloidal quantum dot coupled to an SPP waveguide. Since surface plasmon polaritons are charge density waves that propagate along metal-dielectric interfaces, they can be concentrated and guided by current-carrying wires, suggesting an integrated approach to optical and electrical signal processing. The near-field plasmon detection

scheme proposed by [53] consists of a Ag nanowire crossing a Ge nanowire field-effect transistor (Figure 1.11). The Ag nanowire guides SPPs to the Ag-Ge junction, where they are converted to electron-hole pairs and detected as current through the Ge nanowire. Current through the Ge nanowire (I) is recorded when the laser is focused at either end of the Ag nanowire. This I signal is the key signature for electrical SPP detection. Propagating SPPs can be launched in the Ag nanowire only when the excitation laser is incident on the Ag nanowire ends. Further evidence for electrical SPP detection is provided by the dependence of I on the polarization of the excitation laser. I is largest when the excitation polarization is parallel to the Ag nanowire axis, and smallest when perpendicular. This preference reflects the conversion efficiency of the excitation light into SPP modes. The fundamental SPP mode consists of cylindrically symmetric charge oscillations along the Ag nanowire axis.

On-chip electrical detection has been demonstrated using organic photodiodes, gallium arsenide structures and germanium wires. However, none of these techniques has provided single plasmon sensitivity. By coupling a plasmon waveguide to a superconducting single-photon detector (SSPD), the authors in [52] demonstrate on-chip electrical detection of single plasmons. Their SSPDs consist of a NbN wire ($\sim 100\mu m$ long, 100 nm wide, $\sim$5 nm thin). The critical temperature T_c below which the wire becomes superconducting is approximately 9 K. When applying a bias current close to the critical current, absorption of a single photon is sufficient to create a local region in the normal, resistive state. This shortlived resistive state is detected as a voltage pulse at the terminals of the wire. The excess energy is dissipated within a fraction of a nanosecond, after which the superconducting state can be restored. They fabricate plasmon waveguides from polycrystalline gold strips, which are electrically insulated from the NbN by a thin dielectric (Figure 1.12). Gratings at both ends serve to couple incoming free-space photons to plasmons confined to the bottom gold/dielectric interface. Measurements are performed in a cryostat at $\sim$4 K. They also varied the shapes of the waveguides. They designed complex structures, one of which is

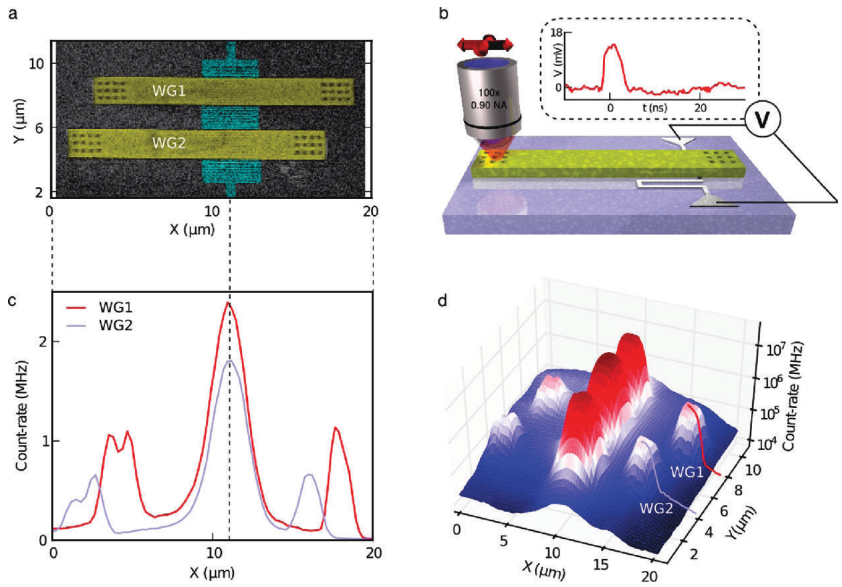


Figure 1.12: (a) A scanning electron microscopy image showing the superconducting detector (cyan) and two gold waveguides (yellow) with coupling gratings. (b) Representation of the low-temperature setup. The sample is XY-scanned through the laser focus. Illumination of the grating excites plasmons at the substrate/gold interface. After propagating along the waveguide, absorption in the SSPD gives a voltage pulse, V. (c) SSPD pulse counts versus laser-spot position. (d) 2D XY-scan. The blue and red lines (WG1 and WG2) indicate where the line-cuts in (c) are taken [52].

a Y-splitter (Figure 1.13). Here the experiment consists of scanning a laser

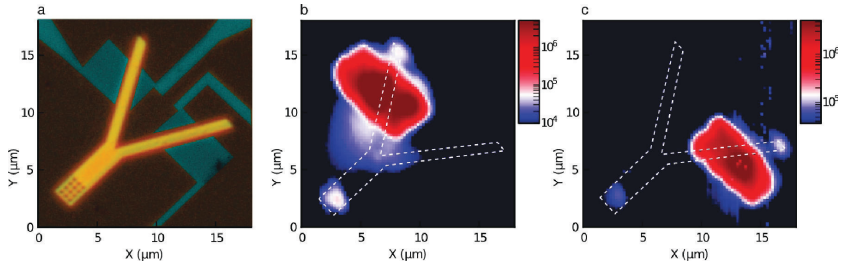


Figure 1.13: (a) Microscope image of a plasmon Y-splitter device. The SSPDs (cyan) are colorized. (b, c) Signal of the left (b) and right (c) detector when scanning a laser spot (980 nm) across the device in (a). Just one detector produces a signal when illuminating the left or right detector. Both detectors produce a signal when illuminating the grating on the bottom left, indicating that plasmons couple to both arms of the Y-plitter. The white contours of the waveguide are a guide to the eye. Note that the color scales are different due to different dark-count levels in the left and right detectors [52].

beam across the sample. Next to the individual detectors, which are visible in just one of the signals, the grating in the bottom left is visible in both images. This indicates that plasmons excited at the grating are propagating in both arms of the Y structure. This device could be used as an integrated plasmon Hanbury Brown and Twiss interferometer.

Plasmons preserve many key quantum mechanical properties of the photons used to excite them, including entanglement [46] and sub-Poissonian statistics [26]. The authors in [46] placed optically thick metal films perforated with a periodic array of subwavelength holes in the paths of the two entangled photons. Such arrays convert photons into surface-plasmon waves which tunnel through the holes before reradiating as photons at the far side. Their coincidence counting measurements show that the entanglement survives to this conversion process, so demonstrating that the surface plasmons have a true quantum nature. The authors in [26] considered the system depicted in Figure 1.14(a). The light emission at the nanowire end is a result of single, quantized surface plasmons scattering off the ends of the nanowire. This is demonstrated in Figure 1.14(b) by the dip at $\tau = 0$ in the photon coincidence measurements between the free-space fluorescence of the quantum dot and emission from the wire end. This near-zero coincidence is a

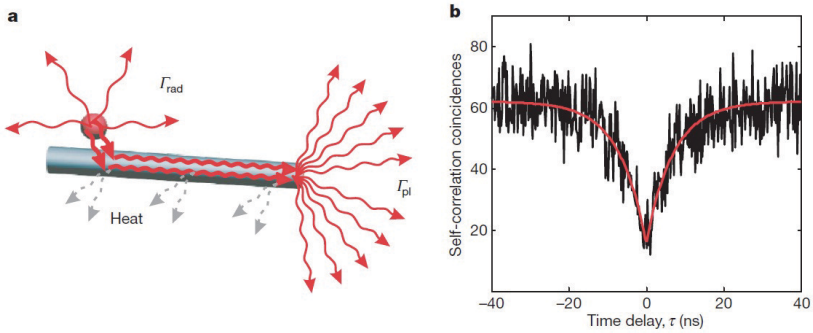


Figure 1.14: a, A coupled quantum dot can either spontaneously emit into free space or into the guided surface plasmons of the nanowire; b, Second-order cross-correlation function between fluorescence of the quantum dot and scattering from the nanowire end [26].

consequence of the fact that the single photon emitted from a quantum dot can either radiate into free space or the surface plasmon modes, but never both simultaneously.

Depending on the size of a metal nanostructure, microscopic quantum effects can be significant in the description of the electrodynamics. The continuous electronic conduction band, valid at macroscopic scales, breaks up into discrete states when the dimensions are small enough, making the Drude model for the dielectric function no longer valid. Scholl et al. have found that as the diameter of a nanoparticle approaches a critical size, the plasmon resonance undergoes a blue shift with linewidth broadening, which is drastically different to the predictions of classical electromagnetism [54].

When metallic nanostructures are placed close to each other quantum tunnelling can occur. Electron tunnelling effects can play an important role in the optical resonances between two nanoparticles with separation distances $d < 1$nm [55]. Moreover, for distances $d < 0.5$nm the dimer enters a conductive regime, where a charge transfer plasmon mode appears involving electrons flowing back and forth between the particles. Savage et al. have experimentally revealed the quantum regime of tunnelling plasmonics in sub-nanometre plasmonic cavities formed by two nanostructures [56]. They found that as the nanostructure separation decreases below a critical size, the plasmon interactions enter the quantum regime, manifested by a blue shift of

the resonances, attributed to the screening of localized surface charges by quantum tunnelling and a consequent reduction in the plasmonic coupling.

Despite recent progress in using quantum optical techniques to study plasmonic systems, adapting them to realistic structures will require a much more detailed understanding of the quantum properties of SPPs when loss is present. This is the central focus of the investigation in this thesis and represents an area so far lacking an in-depth experimental study. Our research in the field of quantum plasmonic is intended as a study of the quantum properties of light and its interaction with matter at the nanoscale. Our investigation of the quantum properties of surface plasmons has the goal to extend the knowledge already existing in the field of quantum optics, and with it all its applications, to the plasmonic field.

For instance, understanding how loss affects the quantum properties of SPPs may open up a route toward the realistic design and fabrication of nanophotonic plasmonic circuits for quantum information processing. With this goal in mind, in Chapter 4, we report our study on the quantum statistics of SPPs in metallic stripe waveguides, assessing the realistic potential of building plasmonic waveguides for nanophotonic circuitry that operates faithfully in the quantum regime.

Another key property yet to be fully investigated is the bosonic character of single surface plasmon polaritons. This knowledge may open up new opportunities for controlling quantum states of light in ultra-compact nanophotonic plasmonic circuitry. The quasi-particle nature of SPPs, consisting of a photon (boson) coupled to a charge density wave of electrons (fermions), makes them an unusual type of quantum excitation. The bosonic character of *photons* was explicitly verified in the seminal work of Hong, Ou and Mandel via the observation of *bunching* in the output field of a 50:50 beamsplitter with identical, indistinguishable photons incident on its two input ports [57]. Recent work using plasmonic waveguides has hinted that SPPs are bosons by observing the Hong-Ou-Mandel (HOM) effect, both indirectly using a photonic beamsplitter [58] and directly using a plasmonic beamsplitter (Figure 1.15) [59]. However, the question as to whether quantum interference is in-

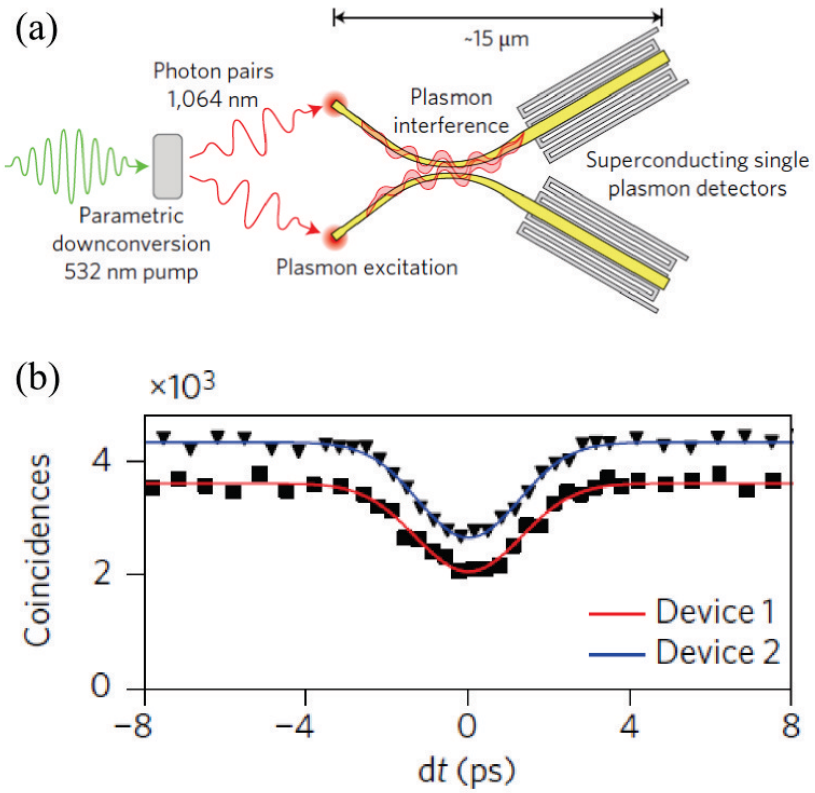


Figure 1.15: (a) On-chip plasmon interference. Photon pairs are generated from parametric down-conversion. A plasmonic directional coupler functions as beamsplitter. (b) HOM interference dip showing quantum interference of surface plasmons in two devices with a 50/50 directional coupling strength. Visibility V = 0.43±0.02 for device 1 and V = 0.39±0.01 for device 2. [59]

volved remains open due to the modest HOM interference observed in these previous reports and shown in Figure 1.15(b), which can also be obtained using classical light [60–63].

In Chapter 4, the direct observation of quantum interference in the HOM effect for single SPPs is reported. Our investigation confirms the bosonic nature of single SPPs in the quantum regime.

Chapter 2

Quantum optics and Quantum plasmonics

Photonic circuits can be much faster than their electronic counterparts, but they are difficult to miniaturize below the optical wavelength scale. Nanoscale photonic circuits based on surface plasmon polaritons (SPPs) are a promising solution to this problem because they can localize light below the diffraction limit.

Our project focuses on the study of the quantum properties of SPPs by using light field in specific, controlled quantum state. After a brief introduction, we will explain the meaning of coherence functions and we will present measurements of the second order coherence coefficient. Our aims are to investigate how the losses can interfere with the transfer of quantum information and then we will focus our attention on the demonstration of the bosonic nature of plasmons.

2.1 Coherence in the classical and quantum regime

In this section, we will discuss the classical and quantum theories of coherence. We review the notions of classical first-order coherence theory and the classical first-order coherence functions. We then proceed to introduce the quantum-mechanical first-order coherence functions. We next introduce the second-order coherence functions known also as the intensity-intensity correlation functions. For this theoretical introduction, we will follow the

description made by *Gerry and Knight* [64].

This theory background will provide the reader with the basic tools for a better understanding of the physics behind the Hanbury Brown and Twiss experiment, one of the pioneering developments of quantum optics, that we will use to experimentally measure the field quality after being passed through a plasmonic lossy channel.

2.1.1 Classical coherence functions

Coherence is a property of waves that enables stationary (i.e. temporally and spatially constant) interference. More generally, coherence describes all properties of the correlation between physical quantities of a wave. We begin with a brief review of classical coherence and we motivate this with Young's two-slit experiment (Figure 2.1). As we already know, under certain

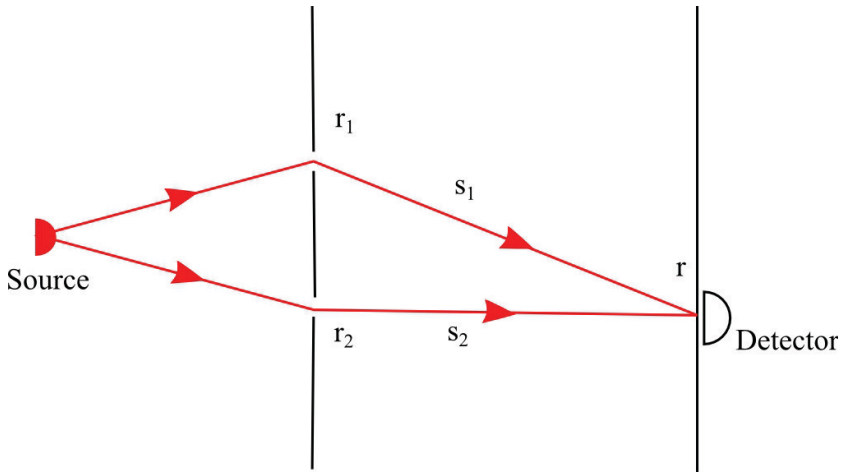


Figure 2.1: Sketch of the standard setup for Young's double-slit interference experiment.

conditions, interference fringes will appear on the screen. If the source has a bandwidth of $\Delta\omega$ and if $\Delta s = |s_1 - s_2|$ is the path difference, interference will occur if $\Delta s < c/\Delta\omega$. The quantity $\Delta s_{coh} = c/\Delta\omega$ is called the coherence length. The quantity $\Delta t_{coh} = \Delta s_{coh}/c = 1/\Delta\omega$ is called the coherence time. Interference fringes will be visible for $\Delta t_{coh}\Delta\omega \cong 1$. The field on the screen, or at the detector, at time t can be written as a linear superposition of the fields at the earlier times $t_1 = t - s_1/c$ and $t_2 = t - s_2/c$, i.e.

$$E(\mathbf{r},t) = K_1 E(\mathbf{r}_1,t_1) + K_2 E(\mathbf{r}_2,t_2) \tag{2.1}$$

where $E(\mathbf{r}_i,t_i)$ is the complex field on the screen arriving from the ith slit and the quantities K_1 and K_2 are complex geometric factors that depend on the distances s_1 and s_2 respectively. The intensity of light on the detector is given by

$$I(\mathbf{r}) = \left\langle |E(\mathbf{r},t)|^2 \right\rangle \tag{2.2}$$

where here the angular bracket means time average. By the ergodic hypothesis, the time average will then be equivalent to an ensemble average. Using Eq. 2.1 we then have

$$\begin{aligned} I(\mathbf{r}) &= |K_1|^2 \left\langle |E(\mathbf{r}_1,t_1)|^2 \right\rangle + |K_2|^2 \left\langle |E(\mathbf{r}_2,t_2)|^2 \right\rangle \\ &\quad + 2Re\left[K_1 \cdot K_2 (E^*(\mathbf{r}_1,t_1)E(\mathbf{r}_2,t_2))\right] \end{aligned} \tag{2.3}$$

The first two terms, that we can call I_1 and I_2, are just the intensities associated with the fields from each of the slits, while the third term gives rise to the interference.

We now introduce the first-order normalized mutual coherence function

$$\gamma^{(1)}(x_1,x_2) = \frac{\langle E^*(x_1)E(x_2)\rangle}{\sqrt{\left\langle |E(x_1)|^2 \right\rangle \left\langle |E(x_2)|^2 \right\rangle}} \tag{2.4}$$

where $x_i = \mathbf{r}_i, t_i$. We can write the intensity measured at the screen in terms of component intensities plus a coherence term:

$$I(\mathbf{r}) = I_1 + I_2 + 2\sqrt{I_1 I_2} Re[K_1 K_2 \gamma^{(1)}(x_1,x_2)]. \tag{2.5}$$

If we set $K_i = |K_i|\, exp(i\psi_i)$ [64] and then write

$$\gamma^{(1)}(x_1,x_2) = \left|\gamma^{(1)}(x_1,x_2)\right| exp(i\phi_{12}) \tag{2.6}$$

then we have

$$I(\mathbf{r}) = I_1 + I_2 + 2\sqrt{I_1 I_2}\left|\gamma^{(1)}(x_1,x_2)\right| cos(\phi_{12} - \psi) \tag{2.7}$$

where $\psi = \psi_1 - \psi_2$ is the phase difference arising from the difference in path length. Interference will occur for $\left|\gamma^{(1)}(x_1,x_2)\right| \neq 0$. We may discern three

types of coherence:

$$\begin{aligned} &\left|\gamma^{(1)}(x_1,x_2)\right| = 1, \qquad \textit{complete coherence} \\ &0 < \left|\gamma^{(1)}(x_1,x_2)\right| < 1, \quad \textit{partial coherence} \\ &\left|\gamma^{(1)}(x_1,x_2)\right| = 0, \quad \textit{complete incoherence.} \end{aligned} \tag{2.8}$$

2.1.2 Quantum coherence functions

A quantum theory of coherence can be constructed upon observables in a manner that closely parallels the classical theory. The actual determination of the intensity of a beam is determined by measuring in some way the response of the absorbing system. We shall consider an ideal detector consisting of a single atom of dimension small compared to the wavelength of the light. The absorption of light over a broad band of wavelengths results in the ionization of the atom and the subsequent detection of the photo-electron constitutes the detection of the photon. From the counting of the photo-electrons, the statistical properties of the light field may be determined. The single-atom detector couples to the quantized field through the dipole interaction

$$\hat{H}^{(I)} = -\hat{\mathbf{d}} \cdot \hat{\mathbf{E}}(\mathbf{r}, t) \tag{2.9}$$

where we have used the operator notation, $\hat{\mathbf{d}}$ is the dipole moment and $\hat{\mathbf{E}}(\mathbf{r}, t)$ the field. A single free-space field mode can be written as [64]

$$\hat{\mathbf{E}}(t) = i \left(\frac{\hbar \omega_k}{2\epsilon_0 V} \right)^{1/2} \mathbf{e}[\hat{a} e^{-i\omega t} - \hat{a}^\dagger e^{i\omega t}]. \tag{2.10}$$

with $\hat{a}$ and $\hat{a}^\dagger$ the annihilation and creation operators. Therefore we can write the field as

$$\hat{\mathbf{E}}(\mathbf{r}, t) = i \sum_{\mathbf{k},s} \left(\frac{\hbar \omega_k}{2\epsilon_0 V} \right)^{1/2} \mathbf{e}_{\mathbf{k}s}[\hat{a}_{\mathbf{k}s}(t) - \hat{a}^\dagger_{\mathbf{k}s}(t)]. \tag{2.11}$$

where the sum over $\mathbf{k}$ simply means the sum over a set of integers (m_x, m_y, m_z) since $k_x = \left(\frac{2\pi}{\lambda}\right) m_x$ with $m_x = 0, \pm 1, \pm 2, ...$, $k_y = \left(\frac{2\pi}{\lambda}\right) m_y$ with $m_y = 0, \pm 1, \pm 2, ...$ and $k_z = \left(\frac{2\pi}{\lambda}\right) m_z$ with $m_z = 0, \pm 1, \pm 2, ...$ or simply $\mathbf{k} = \left(\frac{2\pi}{\lambda}\right) (m_x, m_y, m_z)$. The set of integers (m_x, m_y, m_z) specifies a normal

mode of the field. The sum over s in eq. (2.11) is the sum over the two independent polarizations. $\mathbf{e}_{\mathbf{k}s}$ is a real polarization vector.

We can also write

$$\hat{\mathbf{E}}(\mathbf{r},t) = \hat{\mathbf{E}}(\mathbf{r},t)^{(+)} + \hat{\mathbf{E}}(\mathbf{r},t)^{(-)} \tag{2.12}$$

where $\hat{\mathbf{E}}(\mathbf{r},t)^{(-)} = [\hat{\mathbf{E}}(\mathbf{r},t)^{(+)}]^\dagger$ and $\hat{\mathbf{E}}^{(+)}$ is called the positive frequency part of the field as it contains all terms that oscillate as $e^{-i\omega t}$ for $\omega > 0$, while $\hat{\mathbf{E}}^{(-)}$ is the negative frequency part.

The component of the field describing absorption is the positive frequency part

$$\hat{\mathbf{E}}^{(+)}(\mathbf{r},t) = i\sum_{\mathbf{k},s}\left(\frac{\hbar\omega_k}{2\epsilon_0 V}\right)^{1/2}\mathbf{e}_{\mathbf{k}s}\hat{a}_{\mathbf{k}s}(t). \tag{2.13}$$

The probability that the field undergoes a transition from the initial state $|i\rangle$ to final state $|f\rangle$ is proportional to

$$\left|\left\langle f\left|\hat{\mathbf{E}}^{(+)}(\mathbf{r},t)\right|i\right\rangle\right|^2 \tag{2.14}$$

We are really only interested in the final state of the detector, not the field, so we must sum over all the possible final states. We have assumed the field to be initially in a pure state. More likely, it will be initially in a mixed state described by a density operator of the form $\hat{\rho} = \sum_i P_i |i\rangle\langle i|$, being P_i the probability of the system of be in the state $|i\rangle$. In this case, the expectation value of the sum over all the possible final states of eq. 2.14 is replaced by the ensemble average

$$Tr\left\{\hat{\rho}\hat{\mathbf{E}}(\mathbf{r},t)^{(-)}\cdot\hat{\mathbf{E}}(\mathbf{r},t)^{(+)}\right\} = \sum_i P_i \langle i|\,\hat{\mathbf{E}}(\mathbf{r},t)^{(-)}\cdot\hat{\mathbf{E}}(\mathbf{r},t)^{(+)}\,|i\rangle \tag{2.15}$$

We again use the notation $x = (\mathbf{r},t)$ and define the function:

$$G^{(1)}(x,x) = Tr\left\{\hat{\rho}\hat{E}^{(-)}\hat{E}^{(+)}\right\} \tag{2.16}$$

which is the intensity of light at the space-time point $x = \mathbf{r},t$.

For Young's interference experiment, the positive frequency part of the field at a photo-detector located at position r at time t is of the superposition of the fields from the two slits:

$$\hat{E}^{(+)}(\mathbf{r},t) = K_1\hat{E}^{(+)}(\mathbf{r}_1,t_1) + K_2\hat{E}^{(+)}(\mathbf{r}_2,t_2) \tag{2.17}$$

The intensity of the light on the screen (actually the photodetector) is

$$\begin{aligned} I(\mathbf{r},t) &= Tr\left\{\hat{\rho}\hat{E}^{(-)}(\mathbf{r},t)\hat{E}^{(+)}(\mathbf{r},t)\right\} = \\ &= |K_1|^2 G^{(1)}(x_1,x_1) + |K_2|^2 G^{(1)}(x_2,x_2) \\ &\quad +2Re[K_1^* K_2 G^{(1)}(x_1,x_2)] \end{aligned} \tag{2.18}$$

We may define [64], in analogy with the classical coherence function $\gamma^{(1)}(x_1,x_2)$ of eq. (2.4), the normalized first-order quantum coherence function

$$g^{(1)}(x_1,x_2) = \frac{G^{(1)}(x_1,x_2)}{[G^{(1)}(x_1,x_1)G^{(1)}(x_2,x_2)]^{1/2}} \tag{2.19}$$

As in the classical case, we may discern three types of coherence:

$$\begin{aligned} &\left|g^{(1)}(x_1,x_2)\right| = 1, \qquad \textit{complete coherence} \\ &0 < \left|g^{(1)}(x_1,x_2)\right| < 1, \quad \textit{partial coherence} \\ &\left|g^{(1)}(x_1,x_2)\right| = 0, \quad \textit{complete incoherence.} \end{aligned} \tag{2.20}$$

2.1.3 Second-order coherence function $g^{(2)}(\tau)$

For quantized electromagnetic fields propagating in the x-direction with an arbitrary lateral beam profile, and represented by the electric field operator $\hat{E}^+(x,t)$, we have at a fixed position, $x = 0$, the following definition

$$g^{(2)}(\tau) = \frac{\left\langle \hat{E}^-(0)\hat{E}^-(\tau)\hat{E}^+(\tau)\hat{E}^+(0)\right\rangle}{\left\langle \hat{E}^-(0)\hat{E}^+(0)\right\rangle^2} \tag{2.21}$$

Here $\left\langle \hat{X}\right\rangle$ represents the expectation value of the operator $\hat{X}$ with respect to the initial state of the field, i.e. an averaging over ensembles. The average of the intensity of the field is assumed to be constant over time, $\hat{E}^-(\tau)\hat{E}^+(\tau) = \hat{E}^-(0)\hat{E}^+(0)$. Throughout we will suppress the position dependence of $\hat{E}^+(x,t)$, as x is fixed at zero. At zero time delay, $\tau = 0$, for n-excitation states $|n\rangle$, we have that $\langle n|\,\hat{E}^-(0)\hat{E}^-(0)\hat{E}^+(0)\hat{E}^+(0)\,|n\rangle = n(n-1)$ and$\langle n|\,\hat{E}^-(0)\hat{E}^+(0)\,|n\rangle = n$, leading to the relation $g^{(2)}(0) = 1 - 1/n$. In particular, for n = 1 (single excitations), we have $g^{(2)}(0) = 0$. Similarly, for n = 2, $g^{(2)}(0) = 0.5$: a measured value of $g^{(2)}(0)$ between 0 and 0.5 is an unambiguous proof that we are dealing with single excitations. On the

other hand, for attenuated laser light described by a weak coherent state $|\alpha\rangle = \sum_{n=0}^{\infty} e^{-|\alpha|^2} \frac{|\alpha|^{2n}}{n!} |n\rangle$, where $|\alpha|^2 = \langle n \rangle$ is the mean excitation number, we have $g^{(2)}(0) = 1$. Moreover, it can be shown using the Cauchy-Schwartz inequality that for any classical electromagnetic field, due to the absence of operators and their commutation relations for the classical electric field $E^+(x,t)$, the numerator in Eq. 2.21 factorizes to give the inequality $g^{(2)}(0) > 1$. Thus by measuring $g^{(2)}(0)$ for a given field, we can determine whether or not it is in the nonclassical regime ($g^{(2)}(0) < 1$). A detailed explanation of the actual measurement of $g^{(2)}$ will be found in section 4.1.2.

2.2 Single photon sources

In order to better grasp the original features of a single-photon source with respect to standard light sources, it is interesting to compare first the statistical properties of light emitted by a black body or a lamp (thermal light) and by a stable laser (coherent light).

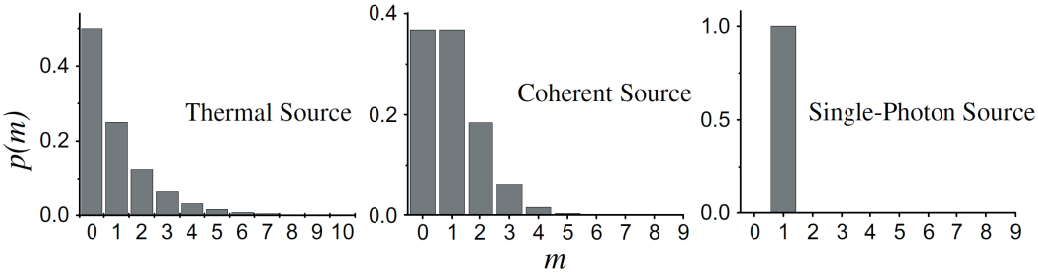


Figure 2.2: Probability distribution of the number of photons for three sources with an average photon number $\langle n \rangle = 1$. The thermal source presents large number fluctuations due to the Bose-Einstein statistics of black-body radiation. The coherent light source presents a Poisson distribution, narrower than that of thermal light, but with still strong number fluctuations, called photon noise. A single-photon source delivers a number-state with $m = 1$.

Figure 2.2 shows the probability distribution of the number of photons for the three sources. In conventional macroscopic sources such as lamps, representing the thermal source case, many independent emitters contribute to the signal. Therefore, the field is a superposition of many incoherent waves.

The classical picture of laser light, representing the coherent source case, is a wave with constant amplitude and phase. The first- and second-order correlation functions of such a wave are obviously both equal to unity. In other words, there are no fluctuations in this classical description. These quantum statistics are very different from those of thermal light. The maximum probability is to find $\langle n \rangle$ photons in the mode. In coherent states, the number of photons obeys the central limit theorem for large numbers. The associated physical picture is that of independent particles, corresponding to a classical limit.

A a single-photon source is an ideal source able to deliver a regular stream of single photons. The fluctuations of the number of photons emitted by this source are weaker than those of a coherent state.

The concept of the photon, central to Einstein's explanation of the photoelectric effect, is exactly 100 years old. Yet, while photons have been detected individually for more than 50 years, devices producing individual photons on demand have only appeared in the last few years. New concepts for single-photon sources, or 'photon guns', have originated from recent progress in the optical detection, characterization and manipulation of single quantum objects. Single emitters usually deliver photons one at a time. This so-called antibunching of emitted photons can arise from various mechanisms, but ensures that the probability of obtaining two or more photons at the same time remains negligible.

The first successful generation of single photons [65] was based on a cascade transition of calcium atoms. Each excited atom delivers a couple of two photons with different colours. A photon at one of the wavelengths is detected after spectral filtering, and is used for the conditional detection of its companion at the other wavelength. Each single photon is thus a 'herald' for the presence of its companion. Although the cascading calcium atoms and the faint sodium beam were the first sources of single photons, their brightness was very low, and a further drawback was that the operation of the source was limited by the density and transit times of the atoms and could not be controlled.

From the mid-1980s, single ions in traps provided long observation times with one and the same ion [66]. These long series of antibunched photons came closer to a 'photon gun', i.e. an ideal device delivering photons one by one. At about the same time, pairs of correlated photons (twin photons) were obtained at high rates by parametric down- conversion [67, 68]. When a short laser pulse is sent into a nonlinear crystal, it generates pairs of signal and idler photons, which are highly correlated in space and time. Provided the probability of generating two pairs at the same time remains negligible, such correlated pairs can be used as sources of heralded single photons. To this day, the parametric sources are the workhorses of quantum-optics experiments. This is the source we use in our experiments, therefore we will discuss it in more detail in the following section.

2.2.1 Spontaneous parametric down-conversion and heralded single photons

As we briefly introduced before, our project is centered around the study of the quantum properties of plasmons. In order to to so, we need single photons able to excite plasmons and, therefore, study their characteristic at the single plasmon level. For our experiments, we used spontaneous parametric down-conversion process able to create heralded single photons.

As a source of single photons, downconversion has the inherent advantages that the apparatus required is simple - only a pump laser and a nonlinear crystal are needed to generate photon pairs, and the entire apparatus is at room temperature and pressure. The variety of lasers and crystals available give a considerable amount of flexibility in determining the parameters of the photons generated, allowing the use of efficient, room-temperature detectors in many cases. This makes parametric down-conversion one of the most promising candidates for single photon sources in quantum information applications. Moreover, the possibility to build a source of degenerate photons, makes any interference experiment doable. The main disadvantage is that this photon-pair creation process is very inefficient (efficiency $\sim 10^{-7} - 10^{-11}$). The number of photon pairs per mode is thermally dis-

tributed within the coherence time of the photons and follows a Poissonian distribution for larger time windows.

Spontaneous parametric down-conversion is a process wherein a pump photon can decay into a pair of daughter photons, known (for historical reasons) as the signal and idler. A nonlinear crystal is used to split photons into pairs of photons that, in accordance with the law of conservation of energy, have combined energies and momenta equal to the energy and momentum of the original photon, are phase-matched in the frequency domain. The equations describing these conditions are known as the phase matching equations:

$$\omega_p = \omega_s + \omega_i \tag{2.22}$$

$$\vec{k}_p = \vec{k}_s + \vec{k}_i \tag{2.23}$$

where ω_μ is photon angular momentum, $\vec{k}_\mu$ is wavevector, and $\mu = p, s, i$ denote pump, signal, and idler respectively.

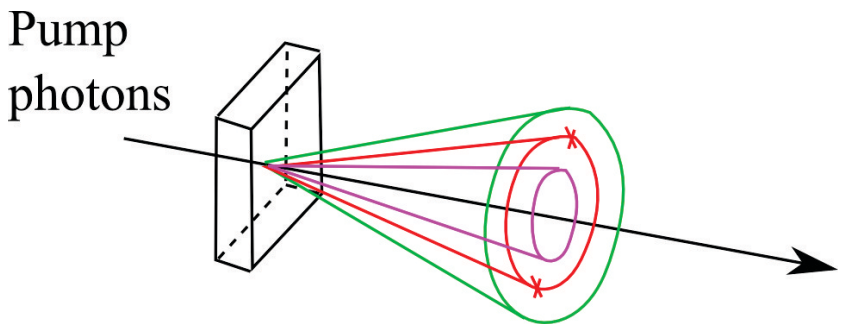


Figure 2.3: Type I down-conversion in BBO, with the crosses representing degenerately down-converted photons.

For type-I parametric down-conversion, the photon pairs are generated in a series of concentric cones, rotationally symmetric about the pump propagation direction, and the angle of each cone is proportional to the frequency of the pairs, see Figure 2.3. As both photons from the same pair are identical, their directions of emission are symmetric about the pump direction. For the nondegenerate case one typically gets a bandwith of 5-10 nm, whereas in the

degenerate case (where the central frequencies of both photons are equal), the bandwidth can be as large as 70 nm.

The interaction Hamiltonian for type-I spontaneous parametric down-conversion is given by [68][67]:

$$\hat{H}_I = \hbar\xi\hat{\alpha}_A^\dagger\hat{\alpha}_B^\dagger + H.c. \tag{2.24}$$

Here, $\xi \propto \chi^{(2)}\epsilon_p$, where $\chi^{(2)}$ is the second-order nonlinear susceptibility of the BBO crystal in our setup and ϵ_p is the amplitude of the classical coherent laser pump field. In addition, $\hat{\alpha}_A^\dagger$(resp. $\hat{\alpha}_B^\dagger$) is a creation operator for a photon in mode A (resp. B) and $H.c.$ represents the Hermitian conjugate. Taking the initial state of modes A and B to be the vacuum $|\psi(0)\rangle = |0\rangle_{AB} = |0\rangle_A |0\rangle_B$ and evolving it according to the Schroedinger equation as

$$|\psi(t)\rangle = e^{-it\hat{H}_I/\hbar}|\psi(0)\rangle \tag{2.25}$$

we obtain, up to first order in time, the state

$$|\psi(t)\rangle = (1-\mu^2/2)|0\rangle_A |0\rangle_B - i\mu|1\rangle_A |1\rangle_B \tag{2.26}$$

where $\mu = \xi t$. By detecting a photon in mode A we remove the first (vacuum) term and 'herald' the presence of a single-photon state $|1\rangle_B$ in mode B, up to first order. By tuning the pump laser intensity appropriately, higher order terms can be made negligible in mode B, even if the detection in mode A is not photon number resolving. Thus, we can use type-I SPDC to produce high-quality single photon states, $|1\rangle$, with larger generation rates than currently achieved with emitter-type sources, such as quantum dots.

2.3 Quantization of surface plasma waves

In the previous sections, we analyzed the quantum theory of coherence and the original features of a single-photon source. Our target is now to use these concepts focusing our attention on the quantum properties of SPP.

Much of the work laying the foundations for quantization was carried out in the 1950s by Bohm and Pines, with work by Pines providing the very first model for quantizing plasma waves in metals [69]. Here, electrons in the

conduction band were considered to be free electrons in an electron gas and the long-range correlations in their positions treated in terms of collective oscillations of the system as a whole.

One of the most fundamental aspects in quantum plasmonics is the description of surface plasmons using quantum mechanics. This is what sets it apart from all other areas of modern plasmonics.

A basic approach to the quantization of surface plasma waves (SPWs) involves quantizing the electromagnetic field by accounting for the dispersive properties of the metal via the collective response of the electrons. There are 3 steps to quantization: (i) Classical mode description, (ii) Discretization of classical modes, and (iii) Quantization via the correspondence principle. We briefly present these steps for SPPs and LSPs. For this theoretical introduction, we will follow the description made by *M. Tame* [25].

2.3.1 Classical mode description

We can start considering a SPW at a plane interface between a metal and vacuum (or air). The metal has a dielectric constant $\epsilon(\omega)$ and initially loss is neglected. One can describe the total electromagnetic field in terms of a vector potential $\mathbf{A}(\mathbf{r}, t)$, where the electric and magnetic fields are recovered in the usual way using Coulomb's gauge ($\nabla \cdot \mathbf{A} = 0$), i.e. $\mathbf{E} = -\frac{\partial \mathbf{A}}{\partial t}$ and $\mathbf{B} = \nabla \times \mathbf{A}$. By solving Maxwell's equations a general form of the vector potential for the SPW is found to be

$$\mathbf{A}(\mathbf{r}, t) = \frac{1}{(2\pi)^2} \int d^2\mathbf{k} \alpha_{\mathbf{k}} \mathbf{u}_{\mathbf{k}}(\mathbf{r}) e^{-i\omega t} + c.c. \tag{2.27}$$

Here, *c.c.* denotes the complex conjugate, $\mathbf{K}$ is a real wave vector parallel to the interface and the frequency ω is linked to the wavenumber, $K = |\mathbf{K}|$, by the dispersion relation $K = \frac{\omega}{c}\sqrt{\frac{\epsilon(\omega)}{\epsilon(\omega)+1}}$. In addition, the term $\alpha_{\mathbf{k}}$ is an amplitude and the mode function $\mathbf{u}_{\mathbf{k}}(\mathbf{r})$ is given by

$$\mathbf{u}_{\mathbf{k}}(\mathbf{r}) = \frac{1}{\sqrt{L(\omega)}} e^{-k_j z} \left(\hat{\mathbf{K}} - i\frac{K}{k_j}\hat{\mathbf{z}} \right) e^{i\mathbf{K}\cdot\mathbf{r}} \tag{2.28}$$

where L(ω) is a length normalization and $k_j^2 = K^2 - \epsilon_j \omega^2/c^2$ characterizes the decay of the field in the z direction with $\epsilon_1 = 1$ and $\epsilon_2 = \epsilon(\omega)$.

2.3.2 Discretization of classical modes

To discretize the SPW mode functions, a virtual square of area $S = L_x \times L_y$ is introduced on the surface. This gives discretized values for the wavenumbers $K_x = n_x 2\pi/L_x$ and $K_y = n_y 2\pi/L_y$, where n_x and n_y are integers. By substituting $\frac{1}{(2\pi)^2}\int d^2\mathbf{k} \rightarrow \frac{1}{S}\sum_{\mathbf{k}}$ and $\alpha_{\mathbf{k}} \rightarrow SA_{\mathbf{k}}$ one obtains the discretized form for $\mathbf{A}(\mathbf{r},t)$. Using the formula for the total energy of the electromagnetic field in the virtual square $U = \int dt \int d\mathbf{r}(\mathbf{E}\frac{\partial \mathbf{D}}{\partial t} + \mathbf{H}\frac{\partial \mathbf{B}}{\partial t})$, where $\mathbf{D} = \epsilon_0\mathbf{E} + \mathbf{P} = \epsilon_j\mathbf{E}$ and $\mathbf{H} = \mu_0\mathbf{B}$ are used, one finds

$$U = \sum_{\mathbf{k}} \epsilon_0 \omega^2 S[A_{\mathbf{k}}A^*_{\mathbf{k}} + A^*_{\mathbf{k}}A_{\mathbf{k}}] \tag{2.29}$$

which has exactly the structure of the energy of a harmonic oscillator for each mode $\mathbf{K}$

2.3.3 Quantization via the correspondence principle

Now we can use the quantized Hamiltonian of a harmonic oscillator $\hat{H} = \sum_{\mathbf{k}} \frac{\hbar\omega_{\mathbf{k}}}{2}[\hat{a}_{\mathbf{k}}\hat{a}^\dagger_{\mathbf{k}} + \hat{a}^\dagger_{\mathbf{k}}\hat{a}_{\mathbf{k}}]$ with the correspondence $A_{\mathbf{k}} \rightarrow \sqrt{\frac{\hbar}{2\epsilon_0\omega S}}\hat{a}_{\mathbf{k}}$ and $A^*_{\mathbf{k}} \rightarrow \sqrt{\frac{\hbar}{2\epsilon_0\omega S}}\hat{a}^\dagger_{\mathbf{k}}$, the field of the SPW is quantized by the association of a quantum mechanical oscillator with each mode $\mathbf{K}$. The operators a $\hat{a}_{\mathbf{k}}$ and $\hat{a}^\dagger_{\mathbf{k}}$ are annihilation and creation operators which destroy and create a quantum of energy, $\hbar\omega_{\mathbf{k}}$, and obey bosonic commutation relations $[\hat{a}_{\mathbf{k}}, \hat{a}^\dagger_{\mathbf{k}}] = \delta_{\mathbf{k},\mathbf{k}'}$. A single quantized SPW excitation, or SPP (now both a wave and a particle), is then written as $\left|1_{\mathbf{k}}\right\rangle = \hat{a}^\dagger_{\mathbf{k}}\left|vac\right\rangle$, where $\left|vac\right\rangle$ represents the vacuum state of the system. The commutation relations are responsible for the different behaviour of physical observables compared to the classical regime. For example, the widely used second-order coherence function at a fixed position, $g^{(2)}(\tau)$, quantifies the probability of measuring an excitation at time $t = 0$ and another at $t = \tau$.

The above quantization procedure can be carried out for more complex waveguides, such as channel and nanowires, with the only change being the mode function $\mathbf{u}(\mathbf{r})$ which represents the classical wavelike properties of the excitation. In most cases a continuum limit is used for the wavevector $\mathbf{K}$. In

order to include loss in the quantization, one couples the SPP to a reservoir of bath modes whose coupling strength is determined in a phenomenological approach from the imaginary part of $\epsilon(\omega)$ for the metal, which is a result of the damping experienced by the electrons. This is mathematically equivalent to the more rigorous reservoir method. A similar procedure is used to quantize the near field of localized plasma oscillations at nanoparticles. The vector potential for the field can be written as $\mathbf{A}(\mathbf{r},t) = \sum_i \alpha_i \mathbf{u}_i(\mathbf{r}) sin(\omega_0 t)$, where the mode function is given by $\mathbf{u}_i(\mathbf{r}) = \hat{\mathbf{i}}$ for $r < R$ and $\mathbf{u}_i(\mathbf{r}) = -\frac{R^3}{r^3}[3(\hat{\mathbf{i}}\cdot\hat{\mathbf{r}})\hat{\mathbf{r}} - \hat{\mathbf{i}}]$ for $r > R$. Here, the subscript i represents the three-dimensional coordinates (i=x,y,z), R is the radius of the nanoparticle and r is the radial coordinate of the position vector $\mathbf{r}$, taken with respect to the centre of the nanoparticle.

Following similar steps as for SPWs, one obtains bosonic annihilation and creation operators $\hat{a}$ and $\hat{a}^\dagger$, where $|1\rangle = \hat{a}^\dagger |vac\rangle$ represents a single quantized localized surface plasma oscillation, or localized surface plasmon (LSP), corresponding to the creation of a quantum of energy $\hbar\omega$ in the near field of the nanoparticle. Internal damping is then modeled as a reservoir of bath modes, as in the SPP case.

2.4 Hong-Ou-Mandel interferometer

The bosonic character of *photons* was explicitly verified in the seminal work of Hong, Ou and Mandel via the observation of *bunching* in the output field of a 50:50 beamsplitter with identical, indistinguishable photons incident on its two input ports [57]. Recent work using plasmonic waveguides has hinted that SPPs are bosons by observing the Hong-Ou-Mandel (HOM) effect, both indirectly using a photonic beamsplitter [58] and directly using a plasmonic beamsplitter [59]. However, the question as to whether quantum interference is involved remains open due to the modest HOM interference observed in previous reports, which can also be obtained using classical light [60–63, 70].

In the following section, we will provide the reader with some tools for understanding the findings of the work of Hong, Ou and Mandel. We will

present the concept of photon bunching and its plasmonic counterpart. These knowledge will be later used in the understanding of our experimental results on the quantum interference in the plasmonic Hong-Ou-Mandel effect, presented in section 4.2.

2.4.1 Photonic bunching

A beamsplitter is simply a partially reflecting mirror with two input and two output ports. In the case of a 50:50 beamsplitter, the two input modes are mixed at the interface and whatever is in each input mode has a probability of one half of ending up in each output mode (Figure 2.4). This illustrates the reason why beamsplitters are such useful components in quantum optics: the indivisible nature of quantized fields results in the output modes being in a quantum superposition that is a combination of whatever was incident on the beamsplitter. Thus, as beamsplitters allow us to observe interference between weak fields, they can be used to demonstrate the bosonic behaviour of single photons.

In 1987, Hong, Ou and Mandel showed the destructive interference between two single photons without a phase relationship at a beam splitter. This benchmark study directly proved the bosonic nature of the photons and allowed to probe the length of their photon wave packets with unprecedented precision [57]. With the current rising interest in the quantum behavior of SPPs, our goal is to reproduce this result with SPPs instead of free space photons.

In the HOM experiment, a single photon in path i is described by the quantum state $|1\rangle_i = \int d\omega_i \phi_i(\omega_i) \hat{a}_i^\dagger(\omega_i) |0\rangle$, where $\phi_i(\omega_i)$ is a normalized spectral amplitude of the photon, $|0\rangle$ is the vacuum state and $\hat{a}_i^\dagger(\omega_i)$ is a creation operator, which together with the operator $\hat{a}_i(\omega_i)$ satisfies the bosonic commutation relation $[\hat{a}_i(\omega_i), \hat{a}_i^\dagger(\omega_i')] = \delta(\omega_i - \omega_i')$ [71]. Taking the two-photon input state at the beamsplitter as $|1\rangle_A |1\rangle_B$ and applying the unitary transformations $\hat{a}_A^\dagger(\omega) = iR^{1/2}\hat{a}_{B_1}^\dagger(\omega) + T^{1/2}\hat{a}_{B_2}^\dagger(\omega)$ and $\hat{a}_B^\dagger(\omega) =$

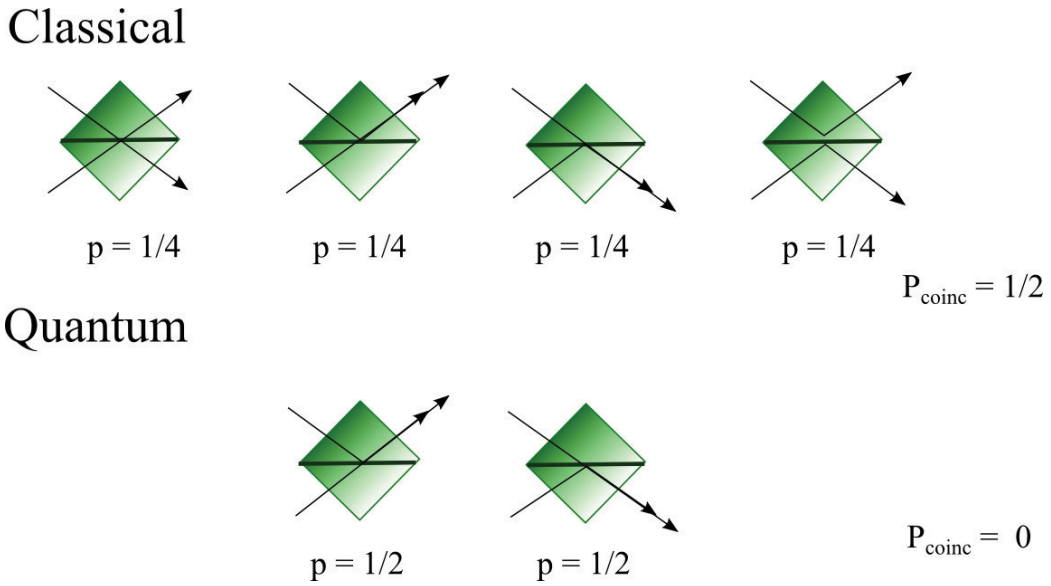


Figure 2.4: Sketch of the different output configurations for a classical and a quantum interference. Each configuration has a probability p=1/4 (classical case) and p=1/2 (quantum case) to happen. The coincidence probability is, therefore, p_{coinc}=1/2 for the classical interference and p_{coinc}=0 for the quantum one.

$T^{1/2}\hat{a}^{\dagger}_{B_1}(\omega) + iR^{1/2}\hat{a}^{\dagger}_{B_2}(\omega)$ leads to the output state:

$$\eta_{in}\eta_{out}[iR^{1/2}T^{1/2}\left|2\right\rangle_{B_1}\left|0\right\rangle_{B_2}+iR^{1/2}T^{1/2}\left|0\right\rangle_{B_1}\left|2\right\rangle_{B_2}-R\left|1\right\rangle_{B_1}\left|1\right\rangle_{B_2}+T\left|1\right\rangle_{B_1}\left|1\right\rangle_{B_2}] \tag{2.30}$$

where the factor η_{in} (η_{out}) accounts for loss in the input (output) arms of the beamsplitter [71]. In the ideal case, $R = T$ =0.5 and the terms with one excitation in each output interfere in a destructive manner. This interference can only be seen in the quantum regime, when the photons are indistinguishable, and leads to the normalized output state

$$\left|1\right\rangle_A\left|1\right\rangle_B \rightarrow \frac{1}{\sqrt{2}}(\left|2\right\rangle_{B_1}\left|0\right\rangle_{B_2} + \left|0\right\rangle_{B_1}\left|2\right\rangle_{B_2}). \tag{2.31}$$

Thus, the photons display bosonic behaviour by bunching together. On the other hand, fermionic excitations will anti-bunch and always exit a beamsplitter through different output ports [1, 72]. Note that bunching occurs regardless of the loss at the input and output stages, which only reduces the overall rate at which the process occurs. From Eq. (2.31), it can be seen that if one photon enters the beamsplitter at each input port, the probability of

detecting a coincidence event where a photon is present at each output port will drop to zero when the photons interfere. On the other hand, when they are unable to interfere, *e.g.* due to their arrival time, each of the output states in Eq. (2.30) occurs with equal probability. In this case, the probability of detecting a coincidence is 1/2 (scaled by the factor $(\eta_{in}\eta_{out})^2$).

If we were to perform a HOM between two independent single photons and place two photon detectors on the two outputs of the beamsplitter, we would never observe simultaneous detection events at both detectors if our two photons were pure and indistinguishable.

This interference is an intrinsically quantum effect. If one of the photons incident on the beamsplitter is subjected to a variable time delay relative to the other, some distinguishability will be introduced between them as a result of the additional timing information available to an observer. As the time delay is scanned, the level of distinguishability changes; when the photons are not temporally overlapped at all upon arrival at the beamplitter, they are perfectly distinguishable and no interference can occur, whereas when they are perfectly overlapped, as was assumed in the calculation above, they are indistinguishable and perfect photon bunching should be seen. Therefore, if one were to record the rate of coincidence detection events at the two detectors as a function of the time delay (which is assumed to be small compared to the coincidence window), one would observe that it drops from a constant value where the photons are not overlapped, to zero at zero time delay.

This interference pattern is called a HOM dip and its visibility is defined as

$$V = \frac{P_C(\infty) - P_C(0)}{P_C(\infty)} \tag{2.32}$$

where $P_C(\tau)$ is the probability of obtaining a coincidence event as a function of the time delay τ. The maximum value that the visibility can attain, when the light arriving at the beamsplitter is classical, has been shown to be 0.5 [62], but for the interference of pure, indistinguishable single photons, the visibility will be 1. In fact, classical electromagnetic waves superposition theory provides a HOM dip with only $V \leq 0.5$ [70]. Let us consider the

classical case of two beams of intensity I_a and I_b with randomly varying relative phase ϕ present at the inputs of the beamsplitter. As we can see in [70], the interference visibility using constant intensity sources and a 50/50 beamsplitter is thus $V_c = 2R_{ab}/(R_{ab}+1)^2$, where $R_{ab} = \langle I_a \rangle / \langle I_b \rangle$. Assuming constant classical intensity, *Rarity et al.* clearly show that the visibility reaches a maximum of $V = 0.5$ when $I_a = I_b$ [70]. Thus, the visibility of $V = 0.5$ in HOM interference is usually considered as the border between classical and quantum physics. However, with a visibility larger than 0.5 we can confirm that the drop is due to *quantum* interference [62, 63]. We want to stress the fact that in the HOM interference between plasmons, the question as to whether quantum interference is involved remains open due to the modest HOM interference observed in previous reports [59], with a visibility always less that 0.5.

The visibility can be reduced if $R \neq T$. In Figure 2.5 (c) is shown the visibility of the HOM dip varying the ratio between T and R. It is clear that, for having the best dip visibility, we need to work in the condition $T = R = 0.5$. This result will be used in the experimental part of our work.

In the time domain, when $R = T$ =0.5, Eq. (2.30) leads to a coincidence probability:

$$P(\Delta t) = (\eta_{in}\eta_{out})^2 \frac{\big(1 - sinc^2(\Delta t \cdot \Delta\omega/2)\big)}{2} \tag{2.33}$$

Here, Δt is the delay between the photons and top-hat spectral amplitudes $\phi_i(\omega_i)$ are used with a FWHM of $\Delta\omega$, leading to the $sinc^2$ term in $P(\Delta t)$. The top-hat function has been used in order to better reproduce the spectral shape of our filtered beams, as we will show in the following chapter, in section 3.1. Thus, we have $P(0) = 0$ and $P(\Delta t \gg \tau_c) = (\eta_{in}\eta_{out})^2/2$, where $\tau_c \sim 2\pi/\Delta\omega$ is the single-photon coherence time and $\tau_c \ll t_c$, with t_c the coincidence window used to correlate the detection events. Using eq. 2.33 we can therefore plot the HOM dip for different time delays δt and different spectral widths $\delta\lambda$, as shown in Figure 2.5 (a).

From Figure 2.5(a) we can select few cross sections for a better understanding of the dip shape dependence with different input spectra. In Figure 2.5 (b) we plot eq. 2.33 for two top-hat shaped spectra with $\Delta\lambda = 3nm$

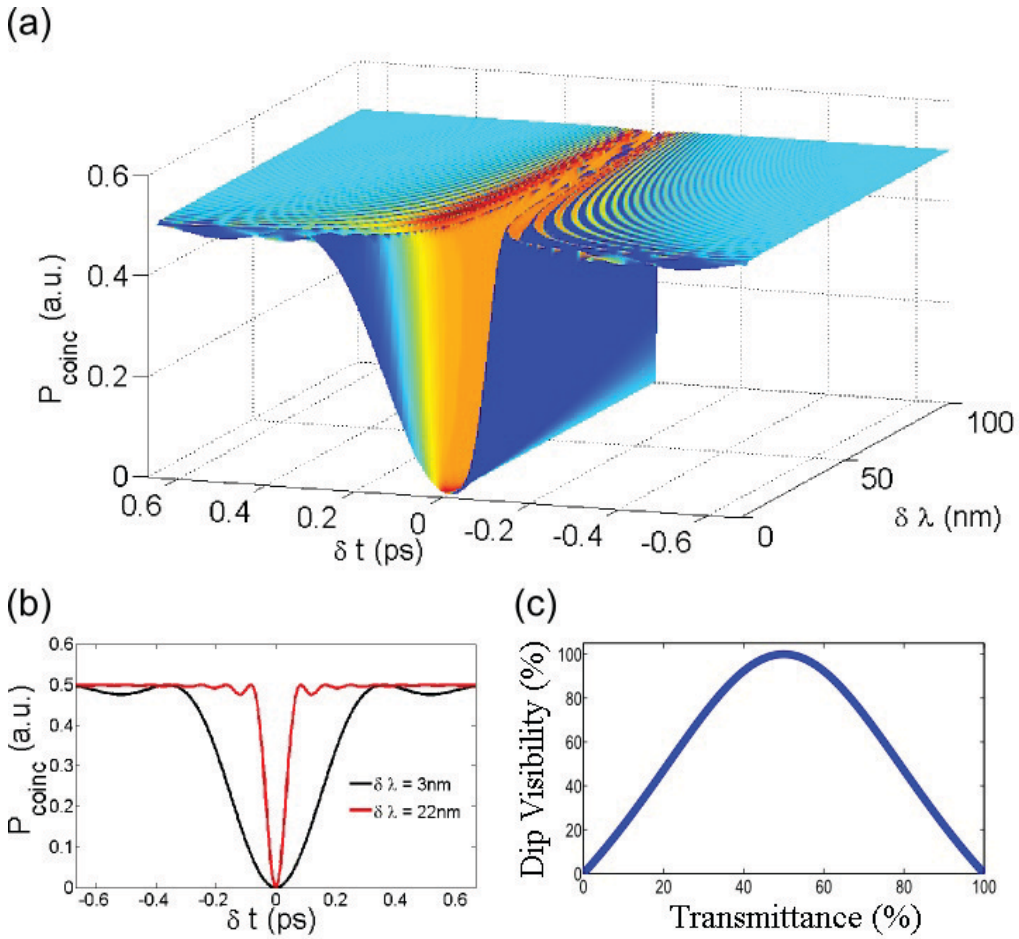


Figure 2.5: (a) HOM dip for different time delays δt and different spectral widths $\delta\lambda$ using eq. 2.33.(b) HOM dip with two different input spectra. In black, a top-hat shaped spectrum with $\Delta\lambda = 3nm$, in red, a top-hat shaped spectrum with $\Delta\lambda = 22nm$. (c) Visibility for different values of splitting ratio on the BS. $R = 1 - T$ is assumed.

and $\Delta\lambda = 22nm$. We can notice that the narrower is the input spectrum, represented by the value of $\Delta\lambda$, the wider is the shape of the HOM dip. In the following chapter, we will show how we experimentally reproduce this behavior.

Chapter 3

Experimental details

In the previous chapters, we gave an overview on SPPs and quantum optics, going through the main key concepts of the theory that stays at the base of our experiments. In this chapter, we want to turn our attention on the experimental details, focusing on the source we used and on the different samples we tested for our experiments.

3.1 Single photon source

As we have seen in the previous chapters, the central tool for performing all our experiments is a single photon source. Here, we present a description of the source we used and, in addition, a detailed alignment procedure is provided.

3.1.1 Description of the source

Figure 3.1 shows a schematic of the experimental setup used for the creation of single photons from down conversion process. The pump laser used in this work is a CW ultraviolet diode (404 nm)[1]; the pump is linearly polarized, output power 100 mW. The beam passes through a telescopic body of lenses (L_1 and L_2) to allow us to control the beam size.

Downconversion is accomplished in a 5x5 mm aperture, 3-mm-long beta-barium borate (BBO) crystal. It is cut for Type-I downconversion of 404-nm pump light, with a 808-nm signal and idler waves making angles of $\Theta = 3\,^{\circ}$ with respect to the pump. Because the crystal is hydroscopic, the crystal

[1]Coherent CUBE 405-100C, 100mW, Circular Beam, Part No.1142279

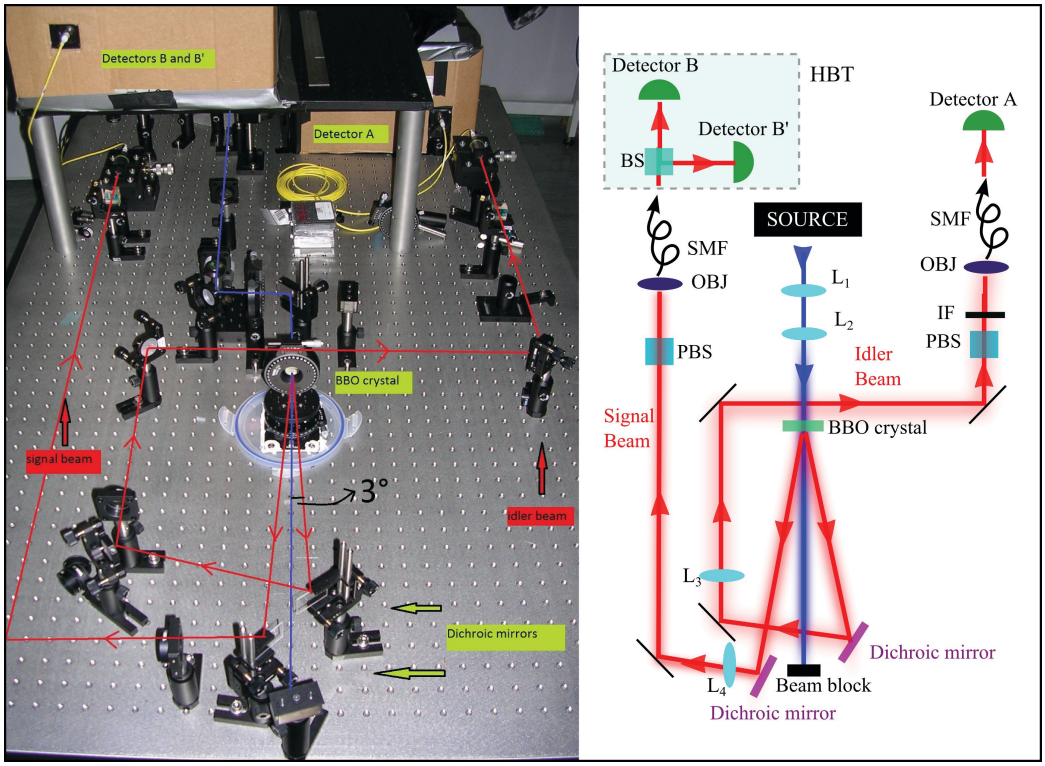


Figure 3.1: Experimental setup of the single-photon source. In the parametric down-conversion process a 405nm laser is sent to a BBO crystal. Two 808nm photons are created and redirected to the detectrors thanks to the dicroic mirrors. The idler beam passes trough a polarizing beam splitter (PBS) and interference filters (IF) before reaching Detector A. The signal beam passes trough the PBS and then enters into the Hanbury Brown and Twiss (HBT) interferometer.

faces have humidity barrier, antireflective coatings. The crystal is mounted in a hermetic box so that when not in use, it is stored in a sealed container with desiccant silica crystals.

The two 808nm photons created are redirected to the dichroic mirrors and, then, through the lenses L_3 and L_4, respectively. In order to be able to characterize our single photon source, the light from one of the IR beams is used as a gating beam. We will call this beam *idler*. The detection of a photon on the idler arm signals the presence of a photon into the other arm. We will tag the detector receiving this signal with the letter A. We name the beam on the other arm as *signal* beam.

Polarizing beam splitters (PBSs) are placed in the paths of the down-converted beams to remove any parasitic light with the incorrect polarization. A $\lambda = 800nm$ bandpass filter, with bandwidth $\Delta\lambda = 22nm$ is placed in arm A to spectrally select only a fraction of the down-converted photons. This effectively selects out an equivalent bandwidth in other arm when the detections are conditioned on A.

The two beams are then collected by 10X microscope objectives (OBJs) for injection into single mode fibers (SMFs).

The *signal* beam is, then, directed into a 50/50 BS and subsequently observed by photodetectors placed in both the transmission and reflection ports of the beamsplitter. We will tag the detectors receiving this splitted signal with the letters B and B'. This ensemble of BS and detectors B and B' is known as Hanbury Brown and Twiss (HBT) interferometer. The *idler* beam is directed into detector A.

All of the photon detection events are time-tagged (Hydraharp 400, PicoQuant GmbH). This allows measurements involving detectors B and B' to be conditioned on the detection of a photon at detector A.

3.1.2 Alignment procedure

The height of all the optical elements used is initially adjusted so that their center is at the same height as the pump beam. The alignment procedure starts from the optics dedicated to the injection of the downconverted

beams into the microscope objectives. The fibers in front of the collection microscope objective launches are mounted in kinematic mounts that allow horizontal, vertical, and focus adjustments. Light from a fiber-coupled 785 nm laser diode is coupled backward through the SMFs so that a red beam exits from the microscope objectives. This alignment needs to be done for left and right arm at the same moment. The two dichroic mirrors are placed so that the angle of these red beams is set to be 3° off from the pump beam, as shown in Figure 3.1, and their position is adjusted so that the 785nm alignment laser is sent onto the center of the downconversion crystal. The dichroic mirrors were adjusted in order to have the alignment beams parallel to the optical table. Thanks to the help of a semitransparent white sheet positioned between the BBO and the dichroic mirrors, the pump beam and the two alignment red beams are projected and made visible. By this way, the dichroic mirrors are adjusted in order to reach a symmetric situation with the two red beams at the opposite sides of the central pump beam. This procedure is needed because the 808nm wavelength of the downconverted beams is invisible. The alignment laser is now removed and the single mode fibers collecting the downconverted beams can be connected to the detectors. The mounts controlling the fine movements of all the optical components - dichroic mirrors and fiber launches - are adjusted to maximize the count rate read from the APDs. Once the single count rate is maximized, the coincidences count rate between the two arms can be maximized as well.

In Figure 3.2, we report the spectra of the single photon source and the coincidence rates between the different detectors.

For the down conversion process, the phase matching conditions are not perfect in the experiment. For this reason, the down-converted light is not monochromatic, but presents a spectrum with finite width [73]: this effect is observed with our source as shown in Figure 3.2(a), where we present its spectral properties. In Figure 3.2(b) the unconditioned coincidence rates $R_{BB'} = N_{BB'}/T$ (where T is the integration time) are shown. No correlation between those two arms arises. On the other hand, when we plot the conditioned rates $R_{AB} = N_{AB}/T$ (Figure 3.2(c)) it is apparent that there is

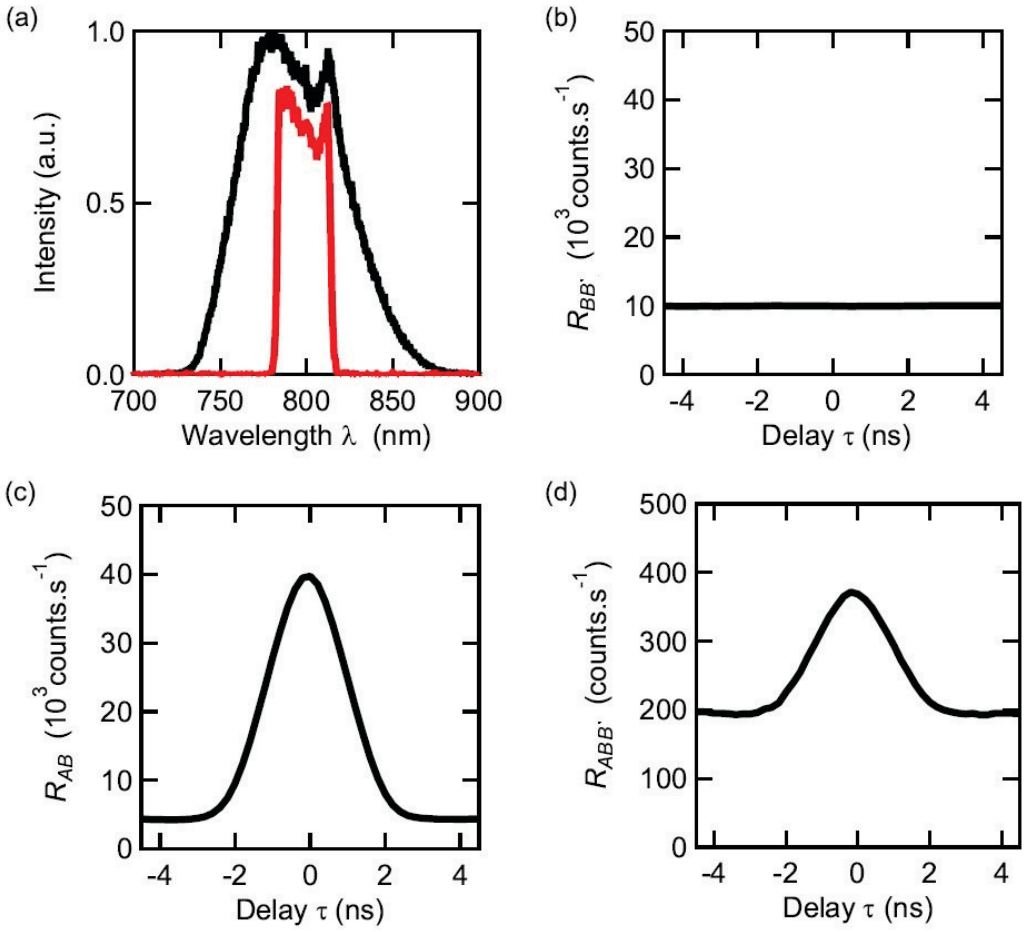


Figure 3.2: Characterization of the heralded single-photon source. (a) Unconditioned spectral intensity function for photons in arms A (red) and B (black). Note that a $\lambda = 800nm$ bandpass filter, with bandwidth $\Delta\lambda = 22nm$ was placed in arm A to spectrally select only a fraction of the down-converted photons. This effectively selects out an equivalent bandwidth in arm B when the detections are conditioned on A. (b) (resp (c)) Coincidence rate between B and B' (resp A and B). (d) Triple coincidence rate $R_{ABB'}$.

a very strong correlation between arm B and the reference arm A at zero delay. The same occurs for B'. This figure shows as well that the configuration used allows for a single photon generation rate of about $4 \cdot 10^5 s^{-1}$. In addition, the triple coincidence rate $R_{ABB'} = N_{ABB'}/T$ is shown in Figure 3.2(d). On first thought, one would expect to see a value of zero at zero delay, as a coincidence between A and B should indicate the presence of a single photon in the system, and thus forbidding any simultaneous detection on B'. However, there is a peak in $R_{ABB'}$ at zero delay: this is due to the fact that we count coincidences within a finite time window Δt. In our case, $\Delta t = 2ns$: two 'clicks' detected within a 2 ns-wide time window are considered as a coincidence, even if they are not exactly simultaneous. For this reason, accidental coincidences are measured, at a rate determined solely by the count rates on each detector, the integration time T and the time window Δt. One can show that [74], if R_B and $R_{B'}$ are the single count rates at B and B' respectively, the accidental coincidence rate at zero delay for three detectors $R_{acc}(0)$ is:

$$R_{acc}(0) = \Delta t R_{AB} R_{B'} + \Delta t R_{AB'} R_B \tag{3.1}$$

3.2 The samples

In our project we used two different samples. The first sample we will describe, *Sample A*, has been used for the characterization of the effects of loss on the quantum statistics of waveguided SPPs. The second one, *Sample B*, has been used for the study on the quantum interference in the plasmonic Hong-Ou-Mandel effect.

Sample A consists of 3 μm wide, 150 nm thick gold stripes fabricated by electron beam lithography on glass coated with 23 nm of indium tin oxide. Input and output gratings with a periodicity of 680 nm were then etched into the waveguides using focused ion-beam milling. To investigate the effects of loss on SPP excitations, the separation between gratings was varied between 5 μm and 30 μm in steps of 2.5 μm. A scanning electron microscope image

of a selection of our waveguides is shown in Figure 3.3(a). These asymmetric

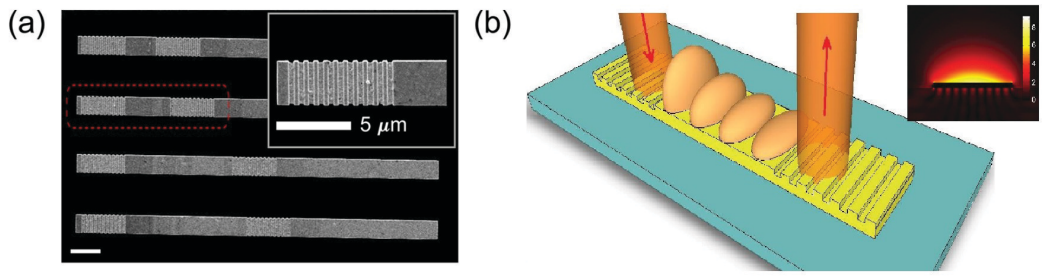


Figure 3.3: *Sample A*. (a) Scanning electron microscope image of a selection of waveguide lengths from 5 to 20 μm. All waveguides have been explored in the quantum regime, however a further time-domain analysis of the quantum statistics has been performed for the 7.5 μm waveguide highlighted by the dashed red box. Inset: detail of one of the in/out-coupling gratings. The scale bars denote 5 μm. (b) Sketch of the SPP excitation and propagation through the waveguide. Inset: fundamental SPP mode in our stripe waveguide - electric field profile along the cross section of the waveguide, calculated using the Finite Element Method (FEM) for an infinitely long waveguide.

waveguides support a number of leaky and bound quasi-TM guided modes. Here, the grating periodicity (see inset of Figure 3.3(a)) was chosen to couple effectively to the leaky-modes supported by the structure (those with highest field intensity at the gold-air interface). Two such leaky modes exist in the waveguides and the lowest order mode, shown in the inset in Figure 3.3(b), possesses by far the lowest losses of the complete set of supported modes. Indeed, the leaky modes of asymmetric waveguides are most often used as plasmonic circuitry components due to their low losses as compared to the bound modes.

Sample B contains gold stripes and plasmonic beamsplitters consisting of two 2 μm wide, 70 nm thick gold stripe waveguides that cross at a right angle at their middle point, as shown in Figure 3.4 (a). These asymmetric waveguides support a single low-loss, albeit leaky, SPP mode [75] and a number of short-range bound modes [76]. The waveguide X-shaped structure was defined on a glass substrate by electron beam lithography (EBL). A second EBL step is used to overlay 90 nm thick input/output gratings and the central scattering elements. We simulated and experimentally studied different beam splitter configurations of coupled waveguides, which gave rather

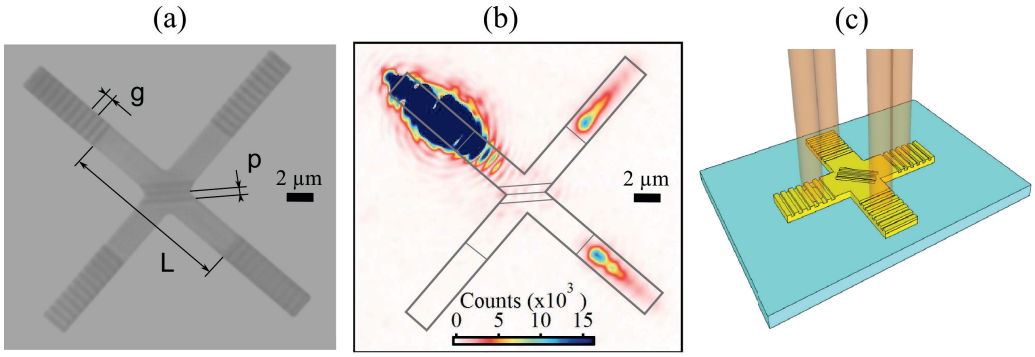


Figure 3.4: *Sample B.* (a) Optical image of the plasmonic beamsplitter structure, obtained in transmission. Here, two 2 μm-wide, 70 nm-thick gold stripe waveguides cross at a right-angle in their middle. The 90 nm thick in/out coupling gratings and central Bragg reflector are defined on top of the stripes. The in/out gratings consist of eleven ridges, each ridge being repeated at an increment of $g = 620$ nm from the end of the waveguide. The distance between gratings is $L = 12.5$ μm. The semi-transparent Bragg reflector is made out of three ridges with a center-to-center distance of $p = 500$ nm. (b) Optical image of the splitter when the SPPs are excited by light from a laser operating at 808 nm focused on the top-left grating. Light is out-coupled from the beamsplitter at the top-right and bottom-right gratings with an almost identical intensity. The integration time has been adjusted to give a reasonable contrast for the output light, leading to a saturation of the signal at the input grating caused by the scattered field. (c) 3D sketch of the X-splitter used as our plasmonics beam splitter.

poor results in terms of splitting; the Bragg mirrors give the correct 50/50 splitting ratio and, in addition, the whole device is more compact.

3.2.1 Fabrication

The waveguides were fabricated on Corning No. 1 cover glass via e-beam lithography (Raith eLiNE) by exposing 300 nm thick poly(methylmethacrylate) (PMMA) resist, coated with a conductive polymer (ESPACER 300Z) to the electron beam. The conductive polymer was then removed in DI water and the PMMA developed in a mixture of methyl isobutyl ketone and isopropanol (1:3). To obtain good propagation at the Au-glass interface and 100% yield during lift-off, the use of a low-loss sticking layer is crucial. For this, the sample was ashed for 4 min in a O2 plasma and immediately transferred to a vessel saturated with (3-mercaptopropyl)trimethoxysilane vapor to form a self- assembled monolayer at the glass surface. A 150nm gold layer for *Sample A* and a 70 nm gold layer for *Sample B* was then deposited by vacuum thermal evaporation, followed by lift-off in acetone. The self-assembled monolayer ensured good adhesion and contact between the glass-Au interface.

In *Sample A*, input and output gratings were then etched into the waveguides using focused ion-beam milling, resulting in gold ridges ∼50nm high.

In *Sample B*, a 90 nm thick Au in and out-coupling gratings were defined using a second-step of e-beam lithography aligned onto the prefabricated waveguides.

3.2.2 Propagation length

An important information about our samples is the SPP propagation length, defined as the length at which the intensity decreases to 1/e of its original value. In order to gather this information, we illuminate the input grating with a single mode pigtailed diode laser with $\lambda_0 = 785nm$ [2]. The light coming from the outcoupling grating is directed to a camera. A picture capturing the intensity of the outcoupled light is taken. This process is

[2]Thorlabs, LM9LP

repeated for waveguides with different lengths, as shown in Figure 3.5(a). For each waveguide two picture have been taken, one with the input beam in TM polarization and another one in TE polarization. The TE picture, which brings the information about the light scattered from the sample, was subtracted from the TM one, which gives us the information about the coupling of the plasmon into the waveguide. At this point, the pixel-values at the output grating were summed in order to give us the information about the overall intensity coming out from the outcoupling grating. Since the intensity of the incoupled light is constant in all our measurements, we can find the propagation length of the SPP mode by plotting the measured intensities versus the stripe lengths, as shown in Figure 3.5(b). By fitting the data-points by a exponential function, we can extrapolate the propagation length value.

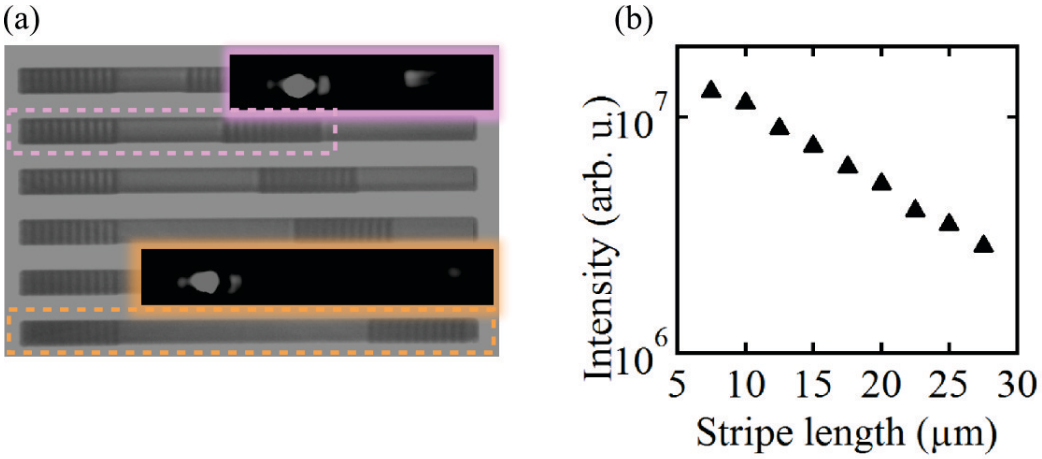


Figure 3.5: (a) Example pictures taken for waveguides with lengths from $5\mu m$ to 17.5 μm deposited on *Sample B*. Insets: input laser beam and output light from the exited plasmon for $7.5\mu m$ and 17.5 μm stripes. (b) Intensity out-coupled from a single waveguide as a function of length when excited by a laser operating at 785 nm. The intensity is averaged over three measurements. Here, we find a propagation length of $l = 12.4 \pm 0.3$ μm.

With this technique we manage to measure the propagation length for both our samples. In *Sample A* we found a propagation length of $l = 8.9 \pm 1.7$ μm, in *Sample B* we found a value of $l = 12.4 \pm 0.3$ μm.

3.2.3 Grating characterization

In light of the considerations shown in section 1.2.4, in our experiment, the coupling efficiency of our gratings has been maximized by always using 11-ridges gratings, and by focusing the incoming beam close to the edge of the grating.

The coupling efficiency of the gratings depends on the wavelength of the illuminating light. The samples contain waveguides (*Sample A*) and beam splitters (*Sample B*) with gratings with different periodicities. By illuminating these with a broadband light source at one grating and collecting the output at the other sides of the stripes, we can measure the spectral response of the structures. For the spectrum measurements, the 10 μm stripe is always used in order to obtain comparable results.

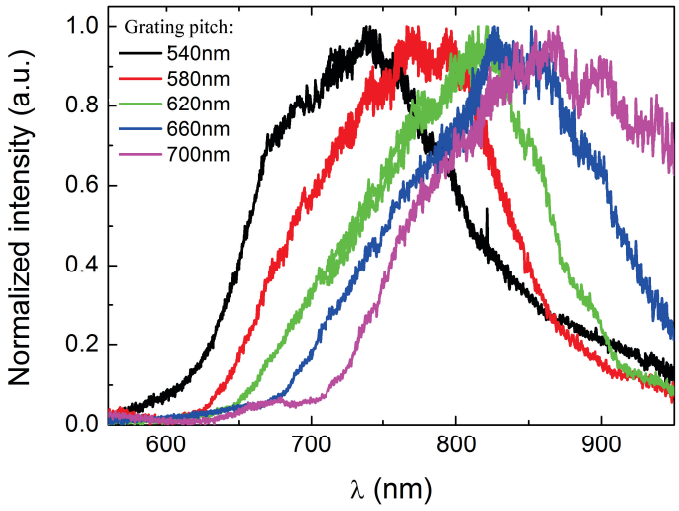


Figure 3.6: Spectra collected from *Sample B* at the output grating of 10 μm stripes when excited with white light at the input grating. The TM-TE intensity is normalized by the reflectance of the source taken on a glass surface. Here we show spectra for five different grating pitches, from 540nm to 700nm at steps of 40nm.

To obtain the spectrum of the surface plasmon excitation, we collect the TM and the TE light, respectively. The TE spectrum, containing mainly the scattered light, is subtracted from the TM spectrum, which carries the plasmonic signal. To have a meaningful spectral response of the structure, it

is important to eliminate the influence of the spectrum of the light source itself. This was done by normalizing the TM-TE spectrum by the spectrum of the source simply reflected on a glass surface. Thanks to the flat reflectance spectrum of the glass, we can consider this spectrum as a good approximation of the spectrum of the input source. In addition, the collection of this spectrum directly from the sample allows us to have a normalization procedure that take into account the response of the whole system (such as optics, wavelength dependent CCD sensitivity, white light spectrum). The results obtained for *Sample B* are shown in Figure 3.6.

As we can see, there is a redshift of the light that couples into the waveguide as SPPs when the grating pitch is increased. The longer the pitch of the grating, the longer the exciting wavelengths, as predicted from the theory. In the *Sample B*, the 620 nm pitch turns out to be the best choice for our experiment, since its spectrum has a broad maximum around $\lambda_0 = 820$ nm, close to the 808 nm of the single photon source used in our measurements. The grating periodicity g of 620 nm is chosen to couple effectively to the low-loss mode supported by the structure - that with the highest field intensity at the gold-air interface and, therefore, this the grating that will be used in the further experiments.

A similar trend has been measured for *Sample A*. Here, the different fabrication process led to a different grating layout and ridge thicknesses. After characterization, the grating periodicity chosen for *Sample A* is g of 680 nm.

3.2.4 Splitting characterization

In *Sample B*, a fundamental feature to be studied in more detail is the characterization of its splitting efficiency, with the main goal finding the best 50:50 beam splitter among the variety of plasmonic beam splitted we have fabricated. As we have seen in Figure 2.5(c), a 50:50 splitting ratio is a fundamental requirement in order to reach the condition of maximum HOM dip visibility.

In the plasmonic beam splitter the splitting operation is obtained via

a scattering process, in direct contrast to previous studies using coupled waveguides [59]. The scattering element is a semi-transparent Bragg reflector, consisting of an arrangement of ridges spaced by p=500, 550 and 600nm, deposited on the top of the central part of the X-shaped splitter, as shown in Figure 3.4 (a). Plasmonic Bragg mirrors, such as the one we use have been studied extensively in the literature, mostly as effective mirrors in the one-dimensional case of normal incidence, both on an infinite interface and on plasmonic waveguides [77]. Some reflectors have also been studied in the two-dimensional case, although with different structures, such as a grating made of individual nanoparticles [78, 79], or Bragg mirrors made of ridges on an infinite interface [80]. We have chosen this approach over coupled waveguides due to its compactness and the ease with which multiple elements can be integrated. Indeed, with this approach the zone over which the two single SPPs interact represents less than two wavelengths.

A Bragg reflector has a resonance wavelength, at which the structure reflects maximally, given by the following equation[80]:

$$\lambda = 2d\cos(\alpha_{inc}) \tag{3.2}$$

with d being the period of the grating and α_{inc} the incidence angle of the beam. In our case of $\alpha_{inc} = 45^o$ and d = 500nm, 550nm and 600 nm.

Different from common Bragg structures, like fiber Bragg gratings, we can not ignore loss our plasmonic beam splitter. A transmission of 0.5 does not guarantee us a 50:50 beam splitter, as the other half of the beam can both be reflected and lost into scattering -similarly to the in/output coupler, they can scatter light out out the structure- and propagation loss [81]. The relationship for reflectivity, transmittance and loss is $R + T + E = 1$, with E being the loss component. The only ratios which are relevant to maximize the visibility of the HOM dip, and that we therefore have measured, are $R/(R + T)$ and $T/(R + T)$: as shown earlier, the losses in the system do not affect the visibility of the dip. We do not measure the local reflection and transmission of the beam splitter, but the ratio of the output intensities of the gratings at the end of the waveguide. If we consider the losses of both

beam splitter output arms identical, this ratio is the same as the local ratio $R/(R+T)$ at the Bragg reflector. We here consider that the reflected and transmitted beam travel the same distance as SPPs, neutralizing the effect of the propagation losses. This is the case as the output gratings are placed equidistant from the Bragg grating.

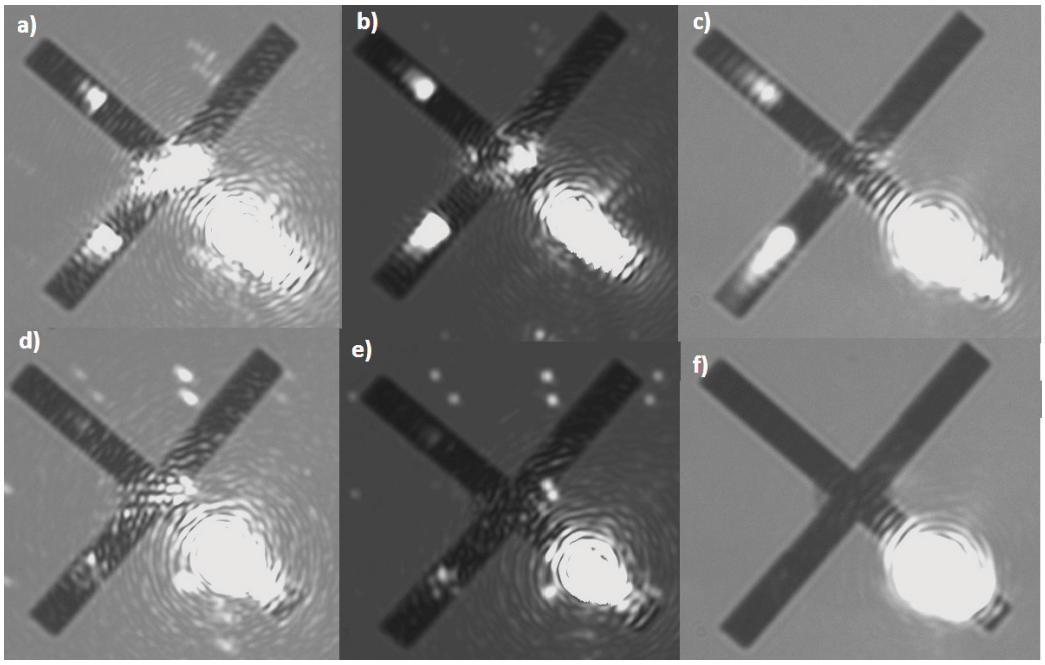


Figure 3.7: Beam splitter with 4 ridges (d = 500 nm) excited at respectively λ= 650, 675 and 775 nm, at TM mode (a), (b) and (c) and TE mode (d), (e) and (f).

The influence of the scattering is a problem more difficult to address. According to the publications mentioned before, specifically [81] and [80], scattering into free space should create a considerable loss at the center of the beam splitters. We will show that our measurements do not capture this kind of scattering in the far-field for the wavelength of our interest, around 800 nm.

To obtain the wavelength dependence of the transmission and reflection coefficients, T and R, of the Bragg element in our beamsplitter, we use light from a supercontinuum filtered to the appropriate wavelength and focused on one input grating of the structure, *e.g.* the top-left grating, as shown in Figure 3.4 (c). For each wavelength the intensity is integrated over the

complete area of each of the output gratings (top-right and bottom-right gratings in Figure 3.4 (c)). The value of T is then the ratio between the intensity at the output grating directly opposite the input grating and the total intensity at both output gratings. This method does not account for any loss due to radiative scattering at the Bragg reflector or during SPP propagation, but gives the relative transmission T of the beamsplitter. The reflection coefficient is then $R = 1 - T$.

As mentioned before, we expect scattering of surface plasmons into the far-field by the ridges composing the Bragg reflector. From Figure 3.7 we can see that this loss is only introduced at lower wavelengths. At 775 nm, close to the 808 nm at which we are interested, we do see only a small amount of light (measured to be less than 10%) coming out of the center of the beam splitter. At 650 nm and less at 675 nm, some scattered light starts to be visible in the central part of the cross. The strong TM dependency gives a indication that this could indeed be the scattering of SPPs.

We are mainly interested in the wavelength dependency of the transmission and reflection of the structures. In Figure 3.8 we plot reflection and transmission intensities varying the incident wavelengths for Bragg reflectors with center-to-center distance of $p = 600$nm, Figure 3.8 (a), (c) and (e), and $p = 500$nm, Figure 3.8 (b), (d) and (f). We also tested Bragg reflectors containing different number of ridges.

As shown in fig. 3.8 (d), a Bragg reflector with three ridges spaced $p = 500$nm gives an average transmission of $T = 0.49 \pm 0.05$ for incident SPPs at $\lambda_0 = 808$ nm, which is the wavelength of the photons used to probe the beamsplitter in our experiment. This value of T remains the same with every input of the beamsplitter.

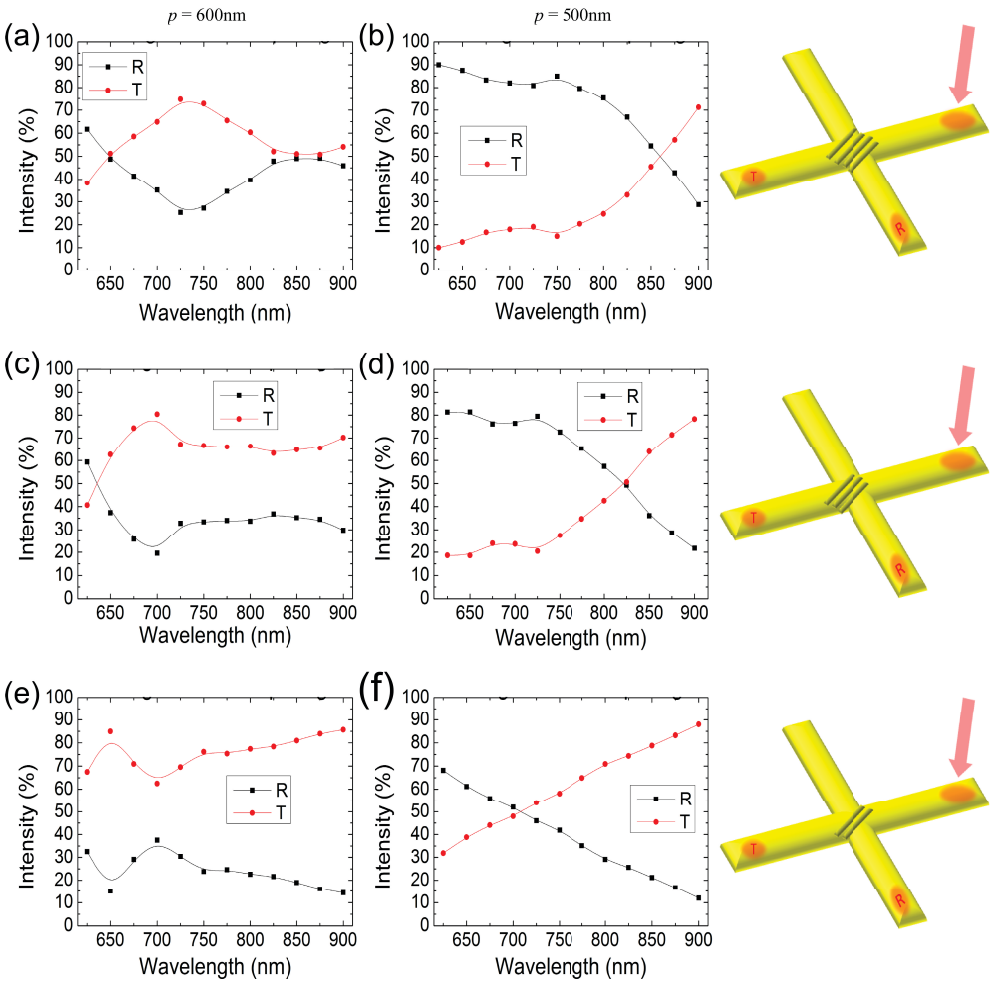


Figure 3.8: Reflection and Transmission intensities varying the incident wavelengths for Bragg reflectors with center-to-center distance of $p = 600nm$ - plots a, c and e - and $p = 500nm$ - plots b, d and f - and for four - plots a and b -, three - plots c and d -, and two - plots e and f - ridges.

Chapter 4

Results and Discussions

4.1 Quantum Statistics of Surface Plasmon Polaritons in Metallic Stripe Waveguides

In section 3.1 we presented the single photon source we used for our experiments. We described the alignment process and the way how we managed to create two beams of heralded photons. Here we will discuss how we used these beams for our study on the quantum statistics of surface plasmon polaritons in metallic stripe waveguides. The goal of our experiment is to show that single SPPs excited in a metallic stripe waveguide by single photons from parametric down conversion preserve their photon-number statistics. We will better understand the role that losses play on the quantum properties of SPPs, assessing the realistic potential of building plasmonic waveguides for nanophotonic circuitry that operates faithfully in the quantum regime.

4.1.1 Experimental setup

After having created the two heralded photon beams, light from one of the IR beams (the idler) is used as a gating beam. The detection of a photon on the idler arm signals the presence of a photon into the other arm.

The other beam (the signal) is focused onto the in-coupling grating of the waveguide probed (Figure 4.1). At the grating, the generated photons are converted into SPPs due to phase-matching conditions. These propagate along the waveguide until they reach the outcoupling grating, at which point they are converted back into light, as previously depicted in Figure

3.3(b). The output is selected by an iris and injected into a multimode fiber (MMF) for analysis. Finally, the multimode fiber directs the output to a Hanbury Brown and Twiss interferometer (BS and detectors B and B') used to measure the second-order quantum coherence function, $g^{(2)}(\tau)$.

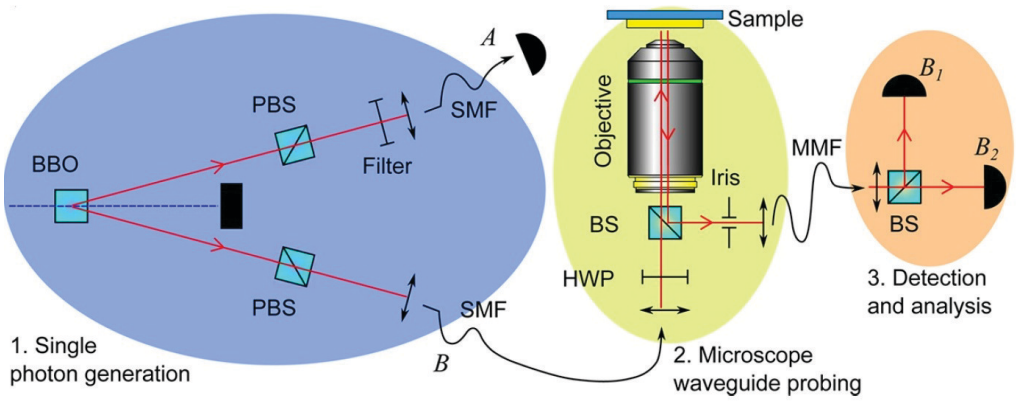


Figure 4.1: Schematic of the experimental setup including a single-photon source stage, waveguide probing stage, and final analysis stage.

All of the photon detection events are time-tagged (Hydraharp 400, PicoQuant GmbH). This allows measurements involving detectors B and B' to be conditioned on the detection of a photon at detector A, with appropriate delays, ensuring that only correlations arising from the injection of single photons into the waveguide are measured.

This setup allowed us to generate, detect and characterize single photons, and the results will be presented in the next section.

4.1.2 Experimental measurement of $g^{(2)}(\tau)$

As we have seen in section 2.1.3, the coherence function $g^{(2)}$is a measure of the correlation of the intensity of a field at a time $t = 0$ and at a later time $t = \tau$ for a fixed position. By measuring $g^{(2)}(0)$ for a given field, we can determine whether or not it is in the nonclassical regime ($g^{(2)}(0) < 1$). In particular, for number states $|n\rangle$, if $g^{(2)}(0) < 0.5$ is measured in an experiment, we can be confident that the field is within the single excitation regime. Experimentally, a beamsplitter is used to symmetrically split the field into modes B and B'. In this case one can show that the definition of

$g^{(2)}(\tau)$ (cf. Eq 2.21) is equivalent to [71][74]

$$g^{(2)}(\tau) = \frac{\left\langle \hat{E}_B^-(0)\hat{E}_{B'}^-(\tau)\hat{E}_{B'}^+(\tau)\hat{E}_B^+(0)\right\rangle}{\left\langle \hat{E}_B^-(0)\hat{E}_B^+(0)\hat{E}_{B'}^-(\tau)\hat{E}_{B'}^+(\tau)\right\rangle} \equiv \frac{N_{BB'}}{N_B N_{B'}}\left(\frac{T}{\Delta t}\right) \tag{4.1}$$

where $\hat{E}^+(t)$ is the electric field operator, T the averaging (integration) time of the measurement, $N_{BB'}$ is the number of coincidence detections at detectors B and B' within a coincidence time window Δt, and N_B and $N_{B'}$ are the number of independent detections at detectors B and B' respectively. All detections at B' are delayed by time t. In our experiment, we use both an attenuated laser source (λ =785 nm) with Eq. 4.1 used to calculate the second-order quantum coherence function and the single-photon source, where all measurements are conditioned on the detection of a photon in mode A. Therefore in this second case we use the conditional form of Eq. 4.1, given by

$$g_c^{(2)}(\tau) = \frac{N_A N_{ABB'}}{N_{AB} N_{AB'}} \tag{4.2}$$

where $N_{ABB'}$ is the number of coincidence detections at detectors A, B, and B', with detections at B and B' occurring within a coincidence time window Δt centered on the detection at A. N_{AB} is the number of coincidence detections at detectors A and B within the coincidence time window Δt and similarly for $N_{AB'}$. N_A is the number of independent detections at detector A. All measurements are taken over an integration time T, which does not appear explicitly in Eq 4.2. The value of $g_c^{(2)}(\tau)$ at zero time delay provides us with a measure of conditioned single-arm statistics in mode B. Additional information about the quality of the field intensity correlations can then be obtained by measuring $g_c^{(2)}(\tau)$ over a range of different time delays τ. An example of $g_c^{(2)}(\tau)$ is shown in Figure 4.2.

The rate of triples observed at zero delay agrees very well with the value expected for solely accidental coincidences. Additionally, these accidental coincidences lead to a value of $g^{(2)}(0)$ higher than zero. One can show [74] that the offset on $g^{(2)}(0)$ due to accidental coincidences is:

$$g_{acc}^{(2)}(0) = \Delta t R_A \left(\frac{R_B}{R_{AB}} + \frac{R_{B'}}{R_{AB'}}\right) \tag{4.3}$$

We first characterize the single photon source described in section 3.1. The measured $g_c^{(2)}(\tau)$ for the single photon source is presented in Figure 4.2. From eq.4.3 and using the count rates values observed at each detector and reported in section 3.1, we calculate the value of $g_{acc}^{(2)}(0) = 0.23$ for $\Delta t = 2ns$, which is the value experimentally observed and shown in Figure 4.2: the non-zero value of $g^{(2)}(0)$ is solely due to accidental coincidences. Moreover, here the width and shape of the dip in $g_c^{(2)}(\tau)$ is only linked to the coincidence window used.

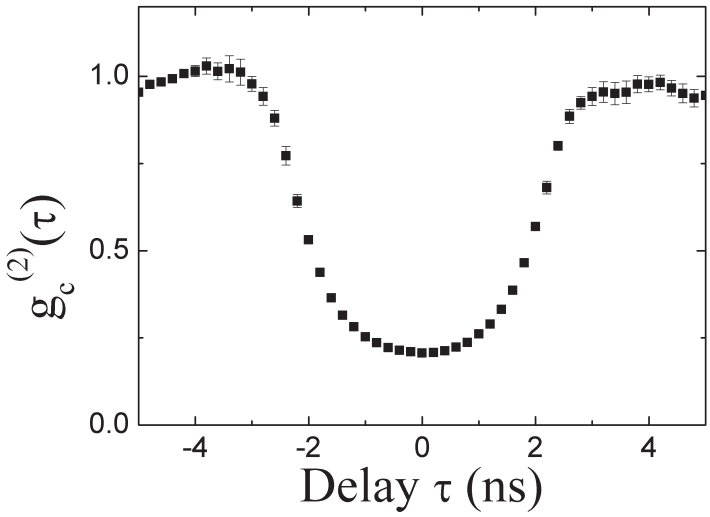


Figure 4.2: Conditional second-order quantum coherence function, $g_c^{(2)}(\tau)$, for the down-converted light. The time window Δt used for the measurement is 2 ns, and the integration times are adjusted to obtain reasonable error bars.

4.1.3 Characterization of the effects of loss on the quantum statistics of waveguided SPPs

In this section, we show how we characterized the effects of loss on the quantum statistics of waveguided SPPs.

The dependence of the output light on the input polarization (TM-only, as shown in Figure 4.3(a)) confirms that the collected light originates exclusively from out-coupled SPPs.

We first measure the second-order quantum coherence function, $g^{(2)}(\tau)$, as a function of time delay τ between detectors B and B'.

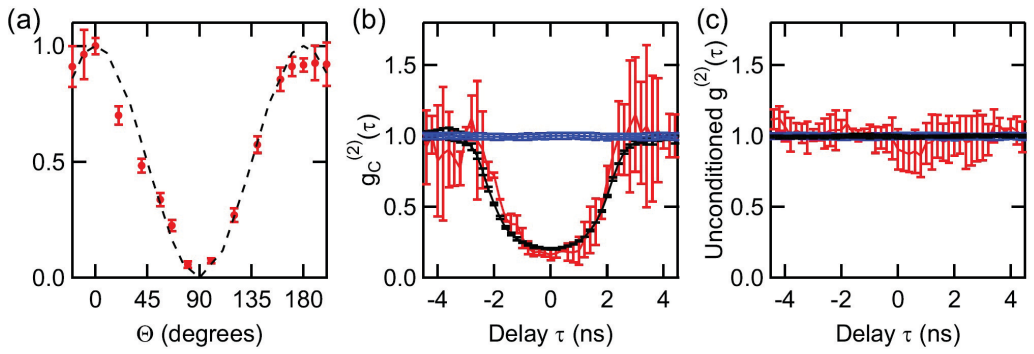


Figure 4.3: Intensity dependence and second-order quantum coherence. (a) Normalized coincidence rate coupled out from a 7.5 μm waveguide, dependent on the polarization angle Θ of the beam incident on the in-coupling grating (red) and the theoretically expected $\cos^2\Theta$ dependence (black dashed line). (b) Conditional second-order quantum coherence function, $g_c^{(2)}(\tau)$, for the down-converted light in mode B before the waveguide (black), along with the out-coupled light when single photons are injected into a waveguide of length 7.5 μm (red). The classical limit is illustrated by the blue data points, corresponding to the unconditioned second-order quantum coherence, $g^{(2)}(\tau)$, for an attenuated laser injected in the waveguide. (c) $g^{(2)}(\tau)$ for the down-converted light in mode B (black) and injected into the waveguide (red). Blue: $g^{(2)}(\tau)$ for the attenuated laser injected in the waveguide.

The results from the single-photon source before and after the waveguides are shown in Figure 4.3b (respectively, black and red curves). The time window Δt used for the measurement is 2 ns, and the integration times are adjusted to obtain reasonable error bars. The statistics obtained after the waveguide are identical to that of the source itself. One can see that the value of $g_c^{(2)}(0)$ <0.5 in both cases which unambiguously demonstrates that we are in the single plasmon excitation regime. Note that $g_c^{(2)}(0)$ is not identically zero in either case. The finite value, however, originates solely from accidental coincidences (see section 3.1).

In Figure 4.3(c) we show the unconditioned $g^{(2)}(\tau)$ as a function of time-delay for the single photon source only and after a 7.5 μm length waveguide (resp. black and red). This plot shows the vital role of the detection of photons in mode A for the conditional measurements of the statistics of the out-coupled light from the waveguides. Without this 'heralding' of the photons, the statistics of the light arriving at the detectors are those of a

thermal field [74]. It should be noted that the theoretically expected peak of $g_c^{(2)}(0)$=2 for a thermal field is challenging to observe in quantum optics experiments [82], as instead of reaching the value of 2, its height above unity is effectively proportional to the ratio of the coherence time of the single-photon source to the response time of the detection, which in our experiment is $\approx 10^{-5}$.

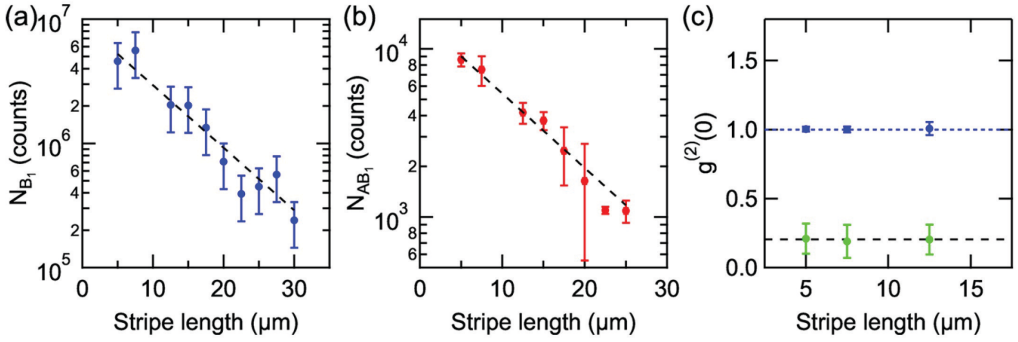


Figure 4.4: Count rate statistics of the light out-coupled from the surface plasmon waveguides. (a) N_B for injected attenuated laser as the length of the waveguide is increased. Dashed black line is a exponential fit, yielding a propagation length $l = 8.9 \pm 1.7\mu$m. (b) Same for N_AB at zero delay for injected single photons. Here, $l = 9.8 \pm 0.6\mu$m. (c) $g_c^{(2)}(0)$ for single photons injected in waveguides of varying lengths (green) and unconditioned $g^{(2)}(0)$ for a laser injected in the waveguides (blue). The black dashed line indicates the value found for the single-photon source and the blue dotted line the classical limit.

We now turn our attention to the effect of losses in the single excitation regime. As the SPPs propagate along the waveguide, the finite conductivity of the metal results in ohmic losses, while radiation into the substrate and surface roughness results in radiative losses. For a reasonably smooth waveguide surface and a thick gold layer, ohmic losses are the main source of damping. At the single excitation level there may be correlations between and within the different damping channels, such as excited phonons, background ion-cores, electron gas collisions and interband transition processes (involving electron-hole pairs), that cause the damping to depart significantly from the classical model. In this case we may be able to see such effects manifest themselves through a change in the behavior of the second-order quantum coherence. Indeed, such a change is well known when light-matter scattering

and absorption processes are involved [71]. Taking a simple linear loss model with uncorrelated Markovian noise [1], we expect that for number states $|n\rangle$, the quantum observables that make up $g^{(2)}$ transform the numerator of eq 4.1 as $n(n-1) \rightarrow \eta^2 n(n-1)$ and the denominator as $n \rightarrow \eta n$, where η is the total loss over the length of the waveguide[83]. Thus, for this particular loss model, the second-order quantum coherence should remain unchanged. Indeed, closer to the plasmon wavelength, the SPP character becomes more electron-like and such effects may become important. This regime remains to be investigated. To explore the quantum statistics in the presence of loss, we first measured the mean excitation rate over a range of waveguide lengths. To do this we measured the counts N_B at detector B for an attenuated laser at a fixed intensity and then the conditional counts N_{AB} at detectors A and B for the single photon source. In both cases, the effect of loss from the beam-splitter in the analysis stage was included in the overall detection efficiency, enabling us to disregard the data from detector B'. In Figure 4.4(a) we show N_B against waveguide length for the injected attenuated laser. Figure 4.4(b) presents N_{AB} at zero delay for injected single photons and as the length of the waveguide is increased. The N_{AB} trend matches N_B, providing evidence that the effect of loss on the field of the single SPPs is consistent with the classical exponential behavior. The SPP propagation length l, defined as the length at which the intensity (mean photon number $\langle n \rangle$) decreases to $1/e$ of its original value, extracted from Figure 4.4a is $l = 8.9 \pm 1.7 \mu m$, a value similar to $l = 9.8 \pm 0.6 \mu m$ obtained from Figure 4.4(b). Both values are in good agreement with each other but smaller than the propagation length expected from finite element method (FEM) calculations of 16.7 μm, due to imperfections introduced by the fabrication of the waveguides.

In Figure 4.4(c), we show $g_c^{(2)}(0)$ for the out-coupled light for injected single photons as the length of the waveguide is increased. The value of $g_c^{(2)}(0)$ for the down-converted photons only is plotted as a dashed black line for reference. One can clearly see that indeed the values remain unchanged

[1] A Markov process can be thought of as 'memoryless': loosely speaking, a process satisfies the Markov property if one can make predictions for the future of the process based solely on its present state just as well as one could knowing the process's full history.

for the lengths investigated. These results therefore provide evidence for the validity of a linear uncorrelated Markovian loss model for SPP damping at the single quanta level. This complements well and goes beyond previous studies looking into the preservation of entanglement via localized plasmons [46] and nonclassicality via long-range surface plasmons[84], where elements of plasmon loss were considered.

4.1.4 Fock state population tomography

We now turn our attention to another representation of the quantum property we are studying, by probing the population structure of the conditioned SPP fields propagating along the waveguides. Note that this is the first time, to the best of our knowledge, that such a technique has been applied to a plasmonic quantum system.

The reconstruction of diagonal elements of density matrix of a quantum optical state, i.e. of its photon statistics, is fundamental for various applications ranging from quantum information to quantum optics. The quantum tomography do provide an alternative method to measure photon number distributions. The method used here is based on the measurement of on/off detection frequencies for a certain optical field when varying the quantum efficiency of the system, i.e. in practice by interposing calibrated neutral filters on the optical path. The beauty of this scheme with respect to alternative ones resides indeed in the extreme simplicity that can allow an extensive application of it to test optical fields in various applications.

We used the technique of Zambra et al. [85] to measure the photon statistics based on on/off detection. The statistics of the 'no-click' and 'click' events from an on/off detector, is given by

$$p(\eta) = \sum_n (1-\eta)^n \rho_n \tag{4.4}$$

where $\rho_n = \langle n \left| \rho \right| n \rangle$ is the photon distribution of the quantum state with density matrix ρ, and η is the quantum efficiency of the detector, i.e. the probability of a single photon to be revealed. The expression (4.4) can be

more compactly written as

$$p_\nu = \sum_n A_{\nu n} \rho_n. \tag{4.5}$$

Here, p_ν can be obtained experimentally and $A_{\nu n}$ can be set by artificially changing the efficiency of the detector, leaving the photon distribution of the quantum state ρ_n as the unknown parameter.

At first sight the statistics of an on/off detector appears to provide quite a scarce piece of information about the state under investigation. However, if the statistics about $p(\eta)$ is collected for a suitably large set of efficiency values then the information is sufficient to reconstruct the whole photon distribution ρ_n of the signal.

The procedure consists in measuring a given signal by on/off detection using different values η_ν of the quantum efficiency. This has been achieved by interposing a series of different calibrated neutral filters on the optical path. The information provided by experimental data is contained in the collection of frequencies $f_\nu = f_0(\eta_\nu) = n_{0\nu}/n_\nu$, where $n_{0\nu}$ is the number of 'no click' events and n_ν the total number of runs with quantum efficiency η_ν.

By imposing the physical constraint $\sum_n \rho_n = 1$ we have the iterative solution that allows us to identify ρ_n^{i+1} knowing ρ_n^i. Our reconstruction of the photon statistics is based on an algorithm, which by an iterative method reaches the ρ_n best reproducing the experimental data, i.e. the statistics of 'no-clicks' f_ν. The algorithm is then carried out until the changes in the population numbers ρ_n between iterations reduce below a given threshold, ϵ. The total error measures the distance of the probabilities p_ν, as calculated at the i-th iteration, from the actual experimental frequencies. In [86], additional details on the mathematical derivation of the tomographic method used to reconstruct the populations are provided.

We perform two different measurements for reconstructing the population of the field out-coupled from the waveguides. In one first measurement, we excite plasmons using our single photon source and, in a second set of data, we excite plasmons with an attenuated laser.

For the field out-coupled from the waveguides for the single photon source,

we have $n_\nu = N_A$ and $n_{0,\nu} = N_A - N_{AB_\nu}\eta_x$. Here, η_x is a loss scaling factor given by $\eta_x = \eta_d/\eta_0$, which allows us to consider the tomography being performed on the state that enters the detection and analysis stage in our setup (rather than a tomography of the initial state generated, as carried out by Zambra *et al.* [85]). The loss $\eta_d = 0.55/2$ corresponds to detector B's intrinsic efficiency around the operating wavelength of the field used (λ =808nm), combined with that of the beamsplitter in front of it. The loss $\eta_0 = N_{AB_0}/N_A$ is the total loss from initial state generation to detection at B. To measure the coincidences N_{AB_ν} we have set the coincidence window to $\Delta t = 2$ns. A set of efficiencies are then introduced using an ND filter wheel. Here, the efficiencies $\eta_\nu = \eta_d N_{B_\nu}/N_{B_0}$. For the attenuated laser source, as it is not based on conditional measurements at detector A, we set a window of 500ns every 10μs and carry out 10,000 runs. Thus $n_\nu = 10,000$ and $n_{0,\nu} = 10,000 - N_{AB_\nu}$, where N_{AB_ν} is the total number of clicks from the 10,000 runs. The efficiencies $\eta_\nu = \eta_d N_{B,\nu}/N_{B_0}$, where $\eta_d = 0.55/2$ is used as before.

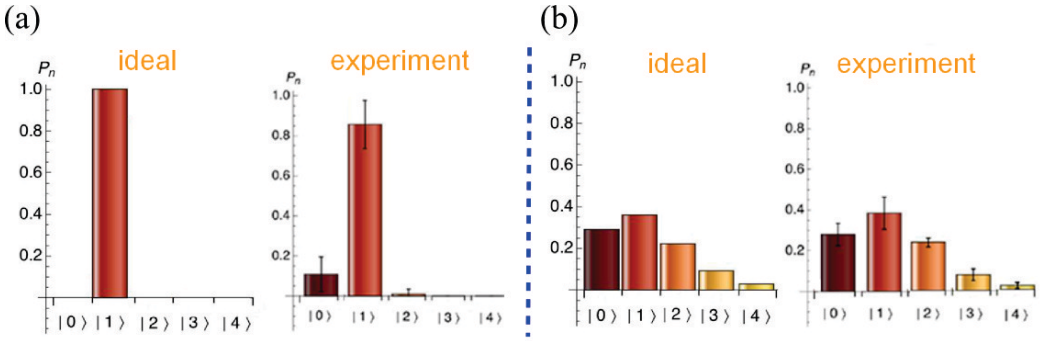


Figure 4.5: Fock state populations of light out-coupled from the waveguides, (a) for conditioned single photons injected into the waveguides, (b) for a laser attenuated, to give on average one photon at the detection stage, $|\alpha|^2 \sim 1$. In both, the ideal populations are and the experimentally reconstructed populations. For the attenuated laser, the ideal populations have been set to correspond to a weak coherent state with $|\alpha|^2 = 1.2$. In both plots the errors are calculated from a Monte Carlo approach, propagating the errors from the measured data through the reconstruction algorithm.

Thanks to this procedure, we are able to obtain the number state, or Fock state populations P_n for a given state, which represents the probability

of the state to have n excitations. For a single-photon state $|1\rangle$, we have $P_1 = 1$ and $P_n = 0$, $\forall n \neq 1$. On the other hand, for an attenuated laser described by the weak coherent state $|\alpha\rangle$, we have the Poissonian distribution $P_n = e^{-|\alpha|^2}(|\alpha|^{2n}/n!)$, where $|\alpha|^2 = \langle n \rangle$ is the mean excitation number. For a mean excitation number of $|\alpha|^2 = 1$, we have the first six populations, $P_0 = 0.368$, $P_1 = 0.368$, $P_2 = 0.184$, $P_3 = 0.061$, $P_4 = 0.015$, and $P_5 = 0.003$, corresponding to the vacuum state $|0\rangle$ and the number states $|1\rangle$, $|2\rangle$, $|3\rangle$, $|4\rangle$ and $|5\rangle$ respectively.

In Figure 4.5(a), we show a tomographic reconstruction of the Fock state populations of the field out-coupled from a 7.5 μm long waveguide, for single-photon excitation. In Figure 4.5(blue), we show the reconstructed populations for a laser attenuated to give on average one photon at the detection stage, $|\alpha|^2 \sim 1$. In Figure 4.5(b), one can clearly see the populations for the out-coupled light from the attenuated laser are consistent with a weak coherent state with mean excitation number of ~ 1. On the other hand, the out-coupled light from the single-photon source, shown in Figure 4.5(a), displays the strong presence of a single population, P_1, representative of a single excitation. This analysis complements the investigation performed in the previous sections and confirms that we are exciting single SPPs on the waveguides when single photons are injected.

4.1.5 Conclusions

Using single photons produced by parametric down conversion, we excited quanta of leaky SPPs in thin metallic stripe waveguides, one of the fundamental building blocks for plasmonic circuits. By measuring the second-order quantum coherence function $g^{(2)}$, we demonstrated the ability to excite single SPPs. Moreover,the effect of losses incurred during propagation of the single SPPs is consistent with the classical exponential behavior and does not change the value of $g^{(2)}$, providing evidence that a linear uncorrelated Markovian loss model is valid for SPP damping at the single quanta level. Our results [86] imply that building longer and more complex SPP waveguide structures operating in the quantum regime is realistic and opens up

the possibility for future studies of new types of functioning devices based on quantum plasmonics, assessing the realistic potential of building plasmonic waveguides for nanophotonic circuitry that operates faithfully in the quantum regime.

4.2 Quantum interference in the plasmonic Hong-Ou-Mandel effect

As we have seen in 2.4, the bosonic character of *photons* was explicitly verified in the seminal work of Hong, Ou and Mandel via the observation of *bunching* in the output field of a 50:50 beamsplitter with identical, indistinguishable photons incident on its two input ports [57].

However, the question as to whether quantum interference is involved in plasmonic systems remains open. We will show how we used plasmonic waveguides to prove that SPPs are bosons by observing the Hong-Ou-Mandel (HOM) effect.

In the following sections, we first confirmed that the single photons generated by our source exhibit the described HOM effect when using a conventional beamsplitter cube. After that, we will show the results obtained from the plasmonic HOM experiment.

4.2.1 HOM dip experiment in free space

Figure 4.6 (a) shows the experimental setup used to conduct our investigation. Here, photon pairs are generated at a wavelength of 808 nm, as described in secion 3.1. Interference filters (IFs) with a central wavelength of 800 nm and 22 nm bandwidth are placed in both paths to spectrally select out the down-converted photons. The photons are then injected into single mode fibers (SMFs). After collimation of the output from the fibers, the photons pass trough polarizers (Pol) in order to remove from the beams any random polarization introduced by the travel into the fibers. Their polarization is then adjusted using half-wave plates (HWPs). In order to vary the amount by which the photons from a given pair are able to interfere with

each other we introduce a time delay in one path by extending it over a distance d with respect to the other using a motorized delay line. This provides a variable delay of $\Delta t = d/c$ between the single-photon wavepackets in each path. The two photons are sent to a conventional beamsplitter to make

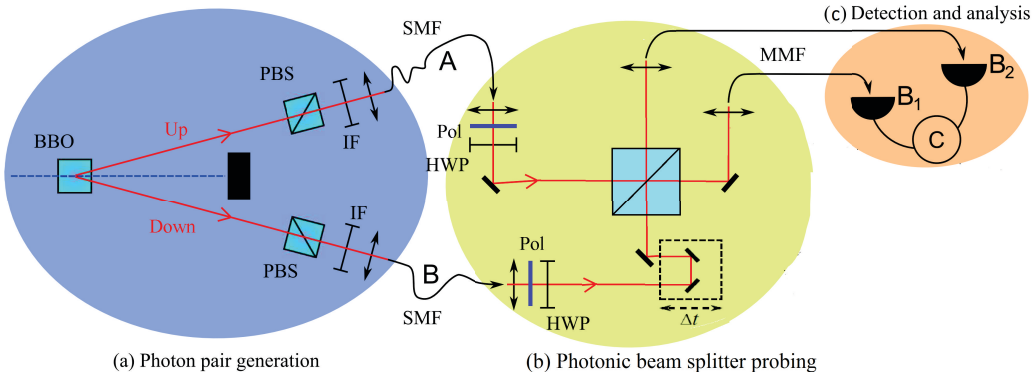


Figure 4.6: Experimental setup. (a) Photon pair generation. Photon pairs are generated via spontaneous parametric down-conversion using a 404 nm pump laser beam focused onto a Beta Barium Borate (BBO) crystal and are filtered using interference filters (IF) to narrow the bandwidth to 800 nm ± 11 nm. Each photon from a pair is coupled into a single-mode fiber (SMF). (b) Photonic beamsplitter. The photons pass trough polarizers (Pol) in order to remove from the beams any random polarization. The half wave plates (HWPs) turn the polarization so that both the photons have the same polarization when they reach the beam splitter. The photons interfere at the beam splitter level and at the output they are then collected by two 10x microscope objectives and coupled into multi-mode fibers (MMFs). A delay line introduces a time delay Δt in one of the photon paths. (c) Detection and analysis stage. The outputs of the MMFs are collected by avalanche photodiodes, B_1 and B_2, where coincident detection events within a time window t_c are collected.

them interfere. It is crucial to tune their polarization in order to ensure their indistinguishability at the beam splitter level. To do so, the two beams are sent through a polarizer and a HWP in order to have both the beams horizontally polarized. Multi-mode fibers (MMFs) collect the light coming out from the beam splitter and direct it to silicon avalanche photodiode detectors B_1 and B_2, which monitor the arrival of the photons from a given output of the splitter. All detection events are time-tagged (PicoQuant Hydraharp 400) and coincidences are evaluated within a $t_c = 2$ ns time window.

In order to first confirm that the single photons generated by our source exhibit the above-described HOM effect when using a conventional beam-splitter cube, we measured the output port coincidences, as a function of the time delay between the arrival of the input port photons. The total travel of the translation stage depicted in Figure 4.6 is only $\sim$ 2.5cm, therefore a coarse estimation of the delay between the two paths needs to be done. The two paths are called path Up and path $Down$, as shown in Figure 4.6. A pulsed laser at 808nm is sent onto the BBO crystal. For this particular measurement, we use the scattered light from the BBO collected by the dichroic mirrors and coupled to the single mode fibers. At this point, pulsed light is going along the two paths and through the beam splitter. Therefore, we are able to measure the time delay between a trigger signal coming from the pulsed laser and the signals reaching the APDs after having traveled along the two different paths. Our goal is to compare the time delay of the Up arm with the time delay of the $Down$ arm in the two different position of the translation stage that are giving the longest delay, $Down_L$, and the shortest one, $Down_S$. Then, we align the optical components so that the delay found in path Up falls between the positions $Down_L$ and $Down_S$, as shown in Figure 4.7. By this way, the central position of the translation stage $Down_0$ gives the same time delay of the arm Up within a precision of 1cm. By this way we can be sure that there will be a position in the range of travel of the translation stage where $\Delta t = 0$.

Once concluded this first coarse delay estimation, it is possible to go back using our single photon source in order to measure the coincidence rate between the two outputs. At zero delay the coincidence rate drops to a minimum value, N_{min}, as expected (Figure 4.8). This drop is quantified using the visibility, V_P, defined as the percentage drop of the coincidences from their maximum value far from the dip center, N_{max}, where the photons do not interfere, *i.e.* $V_P = (N_{max} - N_{min})/N_{max}$ [63, 72].

The expected coincidence rate is given by $N(\Delta t) = N_t P(\Delta t)$, where N_t is the rate of correlated pairs. $N_t(\eta_{in}\eta_{out})^2/2$ is obtained by measuring $N^{exp}(\Delta t \gg \tau_c)$. Here, there is a contribution from uncorrelated (accidental)

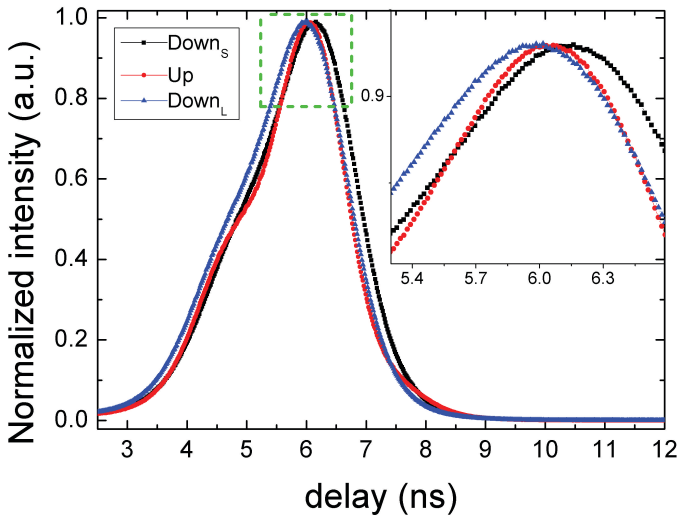


Figure 4.7: Delay estimation with a pulsed laser. The delays from a trigger signal are shown. The different path delays are shown for the arm *Down* in the two position of the translation stage that are giving the longest delay, $Down_L$, and the shortest one, $Down_S$. The delay of arm *Up* falls between $Down_L$ and $Down_S$. Inset: zoom of the peak region.

pairs, N_{acc}, which arrive at the APDs within t_c. Thus, $N^{exp}(\Delta t \gg \tau_c) = N_t(\eta_{in}\eta_{out})^2/2 + N_{acc}$. A large proportion of N_{acc} is given by [86] $N^m_{acc} = t_c N_{B_1} N_{B_2}$, with the rest as $N^r_{acc} = N_{acc} - N^m_{acc}$, leading to $N(\Delta t) = N^r_{acc} + (N^{exp}(\Delta t \gg t_c) - N_{acc})(1 - \mathtt{sinc}^2(\Delta t \cdot \Delta\omega/2))$, where $N^r_{acc} = N^{exp}(0) - N^m_{acc}$.

The photonic HOM dip obtained is shown in Figure 4.8. We find a visibility $V_P = 0.67 \pm 0.05$. The value is limited mainly by the deviation of the beamsplitter from the ideal case of R = T = 0.5. We emphasize here that for a classical input field, a drop in coincidences corresponding to a visibility of up to $V = 0.5$ can be observed [60, 62]. In fact, classical electromagnetic waves superposition theory provides a HOM dip with a visibility that reaches a maximum of 0.5 [70]. Thus, the visibility of $V = 0.5$ in HOM interference is usually considered as the border between classical and quantum physics. However, with a visibility larger than 0.5 we can confirm that the drop is due to *quantum* interference [62, 63].

The comparison between the experimental photonic HOM dip, in black, and the expected theoretical curve (using eq. 2.33), in red, for a top-hat

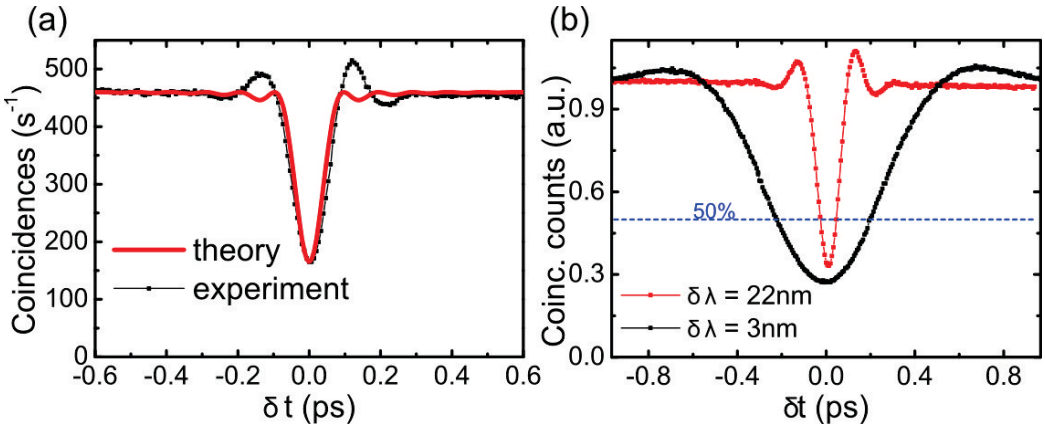


Figure 4.8: (a) Comparison between the experimental photonic HOM dip, in black, and the expected theoretical curve, in red, for a top-hat shaped spectrum of $\Delta\lambda = 22$nm. (b) Experimental photonic HOM dip with different input spectra, in black $\Delta\lambda = 3$nm, in red $\Delta\lambda = 22$nm.

shaped spectrum of $\Delta\lambda = 22nm$ is shown in Figure 4.8(a). We can see a very good agreement between theory and experiment. The reason the theory does not match on the 'wings' at the top left and right of the curve is due to the shape of the spectrum not being exactly a top-hat shape (see Figure 3.2 (a) in section 3.1).

In addition we performed different HOM experiments varying the bandwidth of the IFs used, therefore varying the value of $\Delta\lambda$. As we can see in Figure 4.8 (b), for smaller $\Delta\lambda$ we have a wider HOM dip, as predicted in eq. 2.33 and observed in the theoretical curves plotted in Figure 2.5(b).

4.2.2 Plasmonic HOM dip experiment

This section is devoted to present our results, showing that SPP have a distinct bunching behaviour as expected for bosons, clearly showing quantum interference is involved in the process. Our investigation confirms the bosonic nature of single SPPs in the quantum regime.

We will go through the experimental details that have characterized this project. We start by showing the experimental setup used and then we will focus our attention on the different techniques used for a coarse timing of the delay between the two beam paths. This included also a timing technique based on the Mach-Zehnder interferometry.

Finally, we will then present and discuss our experimental results.

Experimental setup

For the conduction of the plasmonic HOM experiment, we use the same photon pairs generation as described in section 3.1. The sample is attached to a triaxis piezo stage to allow a fine positioning. In the experiment, the photons need to reach the sample be focused onto separate gratings (spot size 2 μm) at the inputs of an X-shaped plasmonic beamsplitter, shown in Figure 4.9(c), by a microscope objective (100×, NA 0.8). The same microscope objective is also devoted to the collection of the light coming from the output gratings.

In order to achieve this configuration, we could have used a pair of beam splitters at the entrance of the microscope objective. Since passing through each beam splitter implies a loss of 50% of the signal and each beam encounters a beamsplitter three times, using this technique allows to work with only a total of ∼12.5% of the original signal, giving a loss of ∼87.5%. We must remember that we are working with an already weak signal, coming from a downconversion process, and a system characterized by plasmonic losses and low coupling efficiency. Therefore, we need to find another solution for sending the beams to the microscope objective and collecting them from it.

This problem has been overcome by producing a glass pyramid, which has then been coated with a mirror-grade reflective layer (Figure 4.9(a)). The metal used for the deposition is Aluminium and it has been protected with a thin layer of silica. The surfaces obtained are used as reflective mirror. Two of them are used to send the two input beams into the microscope objective, the remaining two are used to collect the two output beams and send them into multimode fibers (MMFs) and then to the APDs. In this challenging alignment process, the pyramid has been positioned on a flat surface and on the top of it, at a distance of ∼ 10cm, we placed a 2 inches mirror, as shown in Figure 4.9(a). The role of this top mirror is twofold: initially, it redirects the two input beams coming from the pyramid to the microscope objective and, after that, it projects the two outcoupled beams onto the remaining two

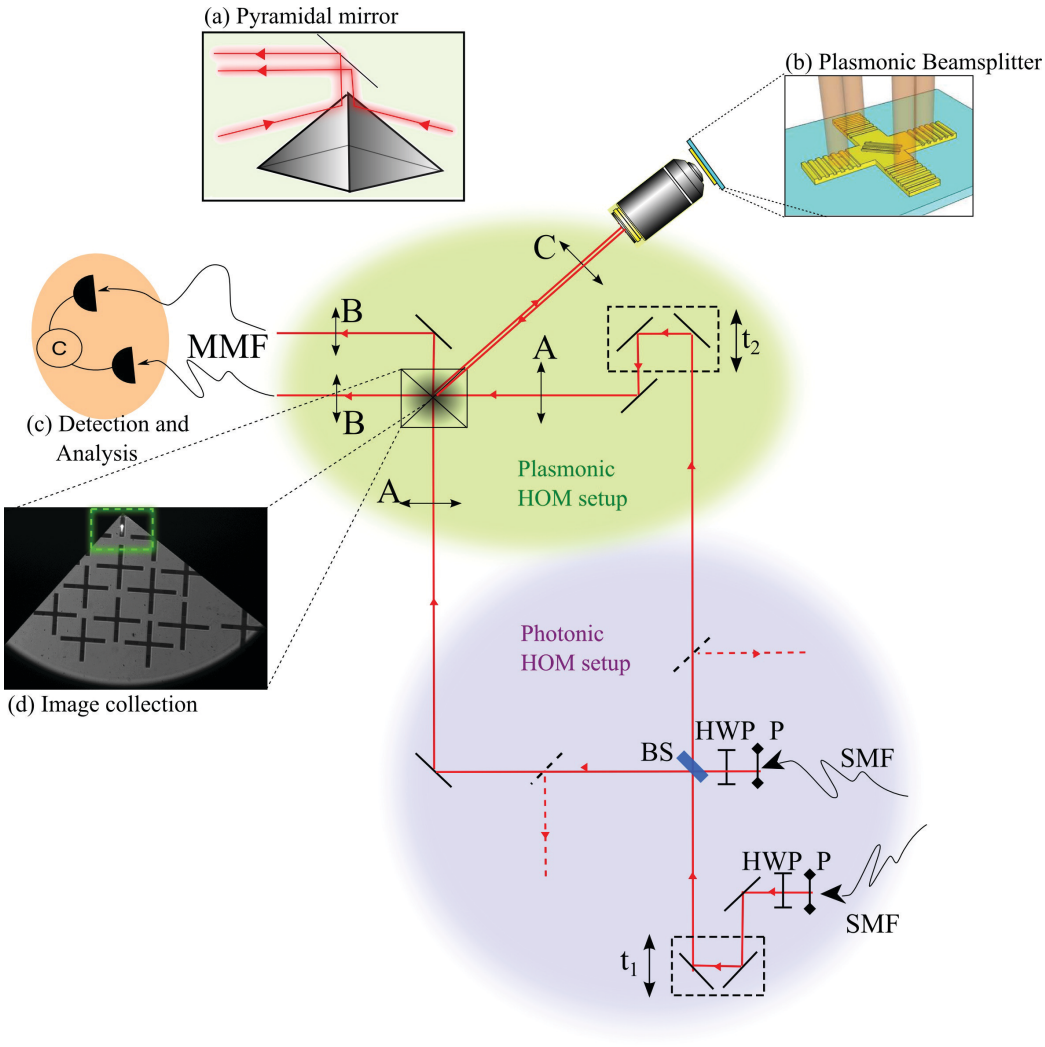


Figure 4.9: Experimental setup. Single photons injected using single mode fibers (SMFs). In the first part of the optical setup, used for the photonic HOM dip detection, the beam splitter (BS) is on a flip mount - flipped up: beams to the detectors following the dashed paths; flipped down: the beams enter in the section for the plasmonic HOM dip experiment. Lens A: f = 300 mm plano-convex, Lens B: f = 75mm plano-convex, Lens C: f = 300 mm bi-convex. (a) Pyramidal mirror. Injection of the single photons into the microscope objective and collection of the two outcoupled photons. (b) Plasmonic beamsplitter. The photons are focused onto separate spots on the input gratings using a microscope objective. The beams at the output gratings are then collected by the same microscope objective. (c) Detection and analysis stage. The outputs of the multimode fibers (MMFs) are collected by avalanche photodiodes for detection of coincident events. (d) Image formed on one face of the pyramid.

faces of the pyramid and, therefore, to the multimode fibers and APDs, as shown in Figure 4.9. An easier way to understand the role of this complex series of optical elements is to see the 2 inches top mirror as a way to project the image of the X-shaped plasmonic structure on the top of the pyramid. Each face of the pyramid hosts one arm of the X shape. This can be easily seen by placing a camera in the output position as shown in Figure 4.9(d). Here, the many different X-shaped splitters present in the sample are visible in the picture, and at the corner of the V-shaped image it is possible to see one arm of the selected splitter. The remaining three arms of the X-shaped splitter are projected on the other faces of the pyramid and, therefore, not present in this picture. Moreover, on the arm of the splitter we can see the light coming out from the outcoupling grating. This image shows that we are actually able to collect the light coming from the grating we are interested in, without being influenced by other sources of light coming, for instance, from the second output grating and the two input beams.

Lenses A (with f = 300mm) are necessary to focus the incoming collimated beams on the pyramid. Then, we focus the beams on the sample thanks to the lens C (with f = 300mm) and the objective. Lenses B (with f = 75 mm) are positioned 300 mm away from the pyramid. This configuration gives a total magnification of the system from the sample to the fiber collectors of M=50, which means that we can approximately collect light with spot size diameter of 4μm coming from the grating into the multimode fibers (with core 200 μm). This way we capture the majority of our output, without capturing other signals. In addition, thanks to this body of lenses, we are able to have the beams on the input grating with a spot size of 2μm.

Multi-mode fibers (MMFs) collect this out-coupled light and direct it to silicon avalanche photodiode (APD) detectors, which monitor the arrival of the photons from a given output of the splitter. All detection events are time-tagged (PicoQuant Hydraharp 400) and coincidences are evaluated within a t_c = 2 ns time window.

Mach-Zehnder interferometer

In the previous sections, we showed how we managed to measure the photonic HOM dip and, therefore, to find the position of the translation stage that gives $\Delta t = 0$ for the two path beams from the BBO crystal till the photonic beam splitter, with a precision of $\sim 1\mu$m. Now, we need to build two paths able to send the two photons from the BBO crystal to the plasmonic beam splitter again with $\Delta t = 0$. Therefore, also the two paths from the photonic beam splitter to the sample, need to have the same length.

To do so we use the technique of the Mach-Zehnder interferometer. In Figure 4.10 we show the sketch of a general Mach-Zehnder interferometer. In our experiment, the photonic beam splitter corresponds to the first beam splitter of a Mach-Zehnder interferometer, the plasmonic beam splitter has the role of the second beam splitter of a Mach-Zehnder interferometer. In this second section of the optical setup, we use again an additional translation stage for the adjustment of the path length t_2. By this way we can elongate one of the two paths in order to reach a configuration of $\Delta t = 0$, as shown on Figure 4.9.

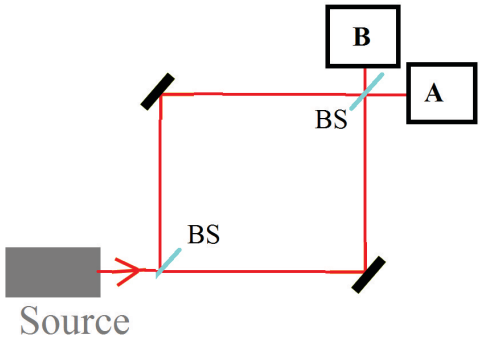


Figure 4.10: Diagram of a simple Mach-Zehnder interferometer.

The Mach-Zehnder interferometer is a particularly simple device for demonstrating interference by division of amplitude. A light beam is first split into two parts by a beam splitter and then recombined by a second beam splitter. Depending on the relative phase acquired by the beam along the two paths the two beams interfere constructively or destructively, leading to an

intensity measured after the beamsplitter being between 0 and 100%. The operation of a Mach-Zehnder interferometer is often used as an example in quantum mechanics because it shows a clear path choice problem.

We can look at Figure 4.10, here we shall use the following definitions: l_1 and l_2 are the total path lengths for the light traveling from the source to the detector for the upper and lower paths respectively. When the light passes through the glass of the beamsplitters it picks up an extra phase shift which we shall call $2\pi t/\lambda$. Note that t is not the thickness of the beamsplitters by this definition. In fact t is the optical path length through the beamsplitter, which takes account of the actual distance travelled (the beam passes through at an angle) and the refractive indices of the glass and the coatings.

The upper path picks up the following phase shifts on the way to detector A: π at the first reflection, π at the second (100%) reflection, nothing at the transmission, $2\pi l_1/\lambda$ for the distance travelled, and $2\pi t/\lambda$ for the extra phase picked up in traversing the glass substrates where the wavelength is reduced. This gives a total of

$$2\pi + 2\pi\left(\frac{l_1 + t}{\lambda}\right) \tag{4.6}$$

The lower path, also on its way to A, picks up a phase shift of π off the 100% reflector, π at the second beam splitter, a phase shift of $2\pi l_2/\lambda$ for the distance travelled, and an extra phase shift of $2\pi t/\lambda$ from passing through the glass substrate at the first beam splitter. The phase difference between the two paths is

$$2\pi + 2\pi\left(\frac{l_1 + t}{\lambda}\right) - 2\pi - 2\pi\left(\frac{l_2 + t}{\lambda}\right) = 2\pi\left(\frac{l_1 - l_2}{\lambda}\right) = \delta \tag{4.7}$$

where δ is the phase shift due to the difference in the path lengths.

Similarly, we can calculate the phase difference between the two paths on their way to detector B. We obtain

$$2\pi + 2\pi\left(\frac{l_1 + 2t}{\lambda}\right) - \pi - 2\pi\left(\frac{l_2 + 2t}{\lambda}\right) = \pi\left(\frac{l_1 - l_2}{\lambda}\right) = \pi + \delta \tag{4.8}$$

Now it is clear that when $\delta = 0$ there is constructive interference on the path to A and destructive on the path B. By varying δ, this condition can

be changed so as to vary the probability of arrival at either detector from 0 to 1.

It is important to say that interference occurs only when the optical path difference is smaller than the coherence length of the beam. As a consequence of this, the magnitude of the temporal coherence of a beam may be used by monitoring the visibility of the interference pattern as a function of path delay, therefore using the Mach-Zehnder interferometer.

The visibility can be written as:

$$V = \frac{I_{max} - I_{min}}{I_{max} + I_{min}} \tag{4.9}$$

The source of single photon is too weak to perform this experiment in a reasonable time. Therefore, we preferred to switch to other sources of light. We firstly performed the Mach-Zehnder interferometer experiment with a 806nm pulsed laser with pulse width of 38.7ps. After having found interferences over a range of $\sim$ 0.7ps, we performed the same experiment with white light. This allows us to reduce the range of interferences to $\sim$ 0.02ps, corresponding to $\sim 5\mu$m, which is the coherence length of white light source used. This method allows to control the arrival time of the single photons of the source onto the sample with a $\sim$ 0.02ps precision.

Mach-Zehnder interferometer with 806nm pulsed laser

Here, we use a 806nm pulsed laser. In order to place the second delay line, a coarse timing is done as previously described for the photonic HOM experiment, using the pulsed laser with the trigger. Then a finer timing is done using the MZ interferences with the same laser. This fine adjustment procedure is described in this section.

The pulsed laser is first directed onto the photonic beamsplitter. The two output beams are then focused onto the two input gratings of the plasmonic beam splitter. A delay line placed into one of the paths provides a variable delay of $\delta t = \delta d/c$ between the laser beams in each path. The intensity at one of the outputs of the plasmonic beamsplitter is monitored by an APD. We see interference patterns when the two split pulses meet at the plasmonic

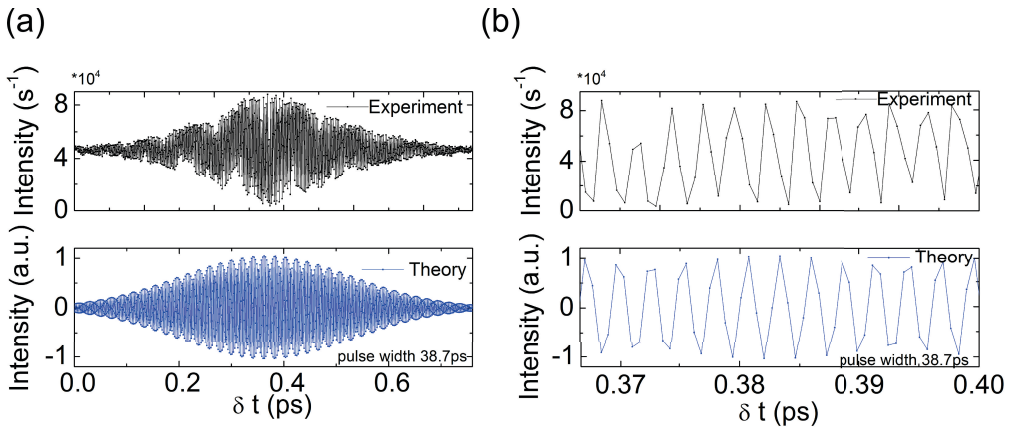


Figure 4.11: Mach-Zehnder interferogram with 806nm pulsed laser. (a) Top. Experimental signal detected from the APD varying the path length of one arm. Bottom. Theoretical curve convolution of the two pulses modeled as the product of a gaussian and a cosine function. (b) Detail of the cosine modulation of the main curve envelope, experimental (top) and theoretical (bottom).

beam splitter stage after having traveled for the same path length. The shape of the interference curve shown in Figure 4.11 is the result of the overlap of the two split pulses, each of them representable by a function $h = f \cdot g$, where f is a gaussian with width equal to the pulse width of the laser, and g is a cosine function where the argument contains the information about the path difference. Therefore, the shape of the interference curve shown in Figure 4.11 is the result of the convolution operation, $h_1 * h_2$, representing the two overlapping pulses. As we can see there is a very good agreement between the experimental curve and the theoretical one. In Figure 4.11(a) we see the envelope of the whole curve and inside it we can clearly see the sinusoidal modulation, shown in 4.11(b). The whole curve envelope covers $\sim$ 0.7ps. Here, we observe a visibility of 92%.

Mach-Zehnder interferometer with white light

Now we can perform the same experiment using white light. This allows us to reduce the range of interferences, and therefore the position for zero path difference, to $\sim$ 0.02ps. We observe a visibility of 67% (see Figure 4.12). Here, the visibility is limited by the higher amount of ligth scattered from the sample compared to the previous case of a laser beam. Therefore, the

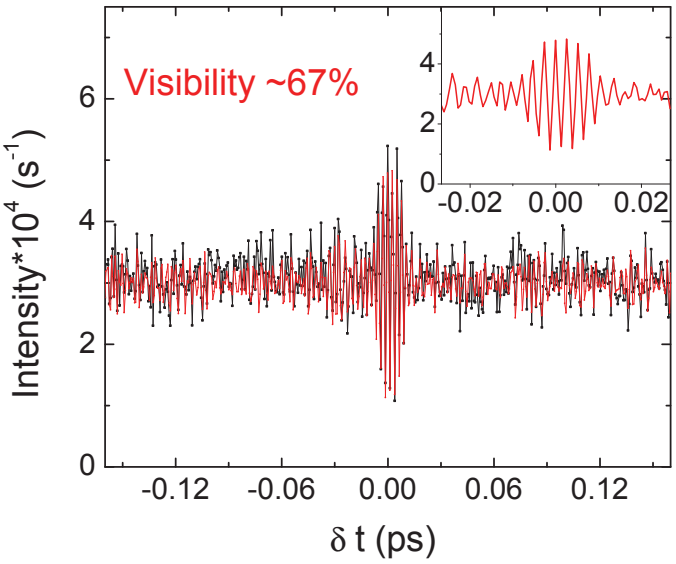


Figure 4.12: Mach-Zehnder interferogram with white light. In black, experimental signal detected from the APD varying the path length of one arm. In red, experimental signal with a band pass FFT filter applied. Inset: zoom of the interferences section.

higher amount of spurious counts brings to a higher baseline.

Thanks to this method, we know with very high precision the position for which we have $\Delta t = 0$, where the plasmonic HOM dip will be found.

Quantum interferences

The plasmonic beamsplitter was then probed as depicted in Figure 4.9. Experimentally, the BS we used for the photonic HOM dip experiment is removed and, therefore, the beams enter in a second section of our optical setup, as described in Figure 4.9. The target is to see whether the HOM effect could be observed and whether or not single SPPs interfere with each other like bosons by bunching together.

When the coupling of single photons into the SPP waveguides is optimized, the count rate due to SPPs scattered by the output grating and detected by APD $B_{1,2}$ is $N_{B_{1,2}} \sim 3.6 \times 10^6$ counts per hour (cph), as shown in the inset of Figure 4.13.

A big challenge of this measurement is the acquisition procedure. We

need to measure the coincidence rate for a range of Δt, by moving the motorized translation stage. Since we have low intensities, each position of the translation stage needs to be integrated for a few hours. One major issue is, therefore, the defocussing and the mechanical drift of the sample during the measurement. In order to avoid this, we implemented a feedback loop to automatically correct for drift of the sample. Every 15 minutes the acquisition program was automatically starting the focusing procedure: the sample was translated in the x, y and z directions in order to find the maximum output intensity and, then, the piezo stage holding the sample was bringing it back to the optimal position that was found.

In order to have reasonable error bars in our data, we run many full scans with rather short integration time, 1h per point, and then we sum the resulting curves to obtain the full HOM dip curve with its error bars.

The time-resolved correlation data give an average number of coincidences of 54.8 ± 1.4 cph far from zero time delay and 30.2 ± 2.4 cph at zero delay. However, a proportion of these counts are due to accidental coincidences from uncorrelated pairs of photons. These uncorrelated pairs are part of the field coupled into the plasmonic beamsplitter but they do not correspond to true correlated photon pairs generated by our source and therefore we subtract them from the overall counts. In principle, these photons could be actively removed by better spectral filtering and reducing the coincidence time window t_c. However, this reduces the overall count rates and leads to extended data integration times which cause stability issues in our setup due to fluctuations in the coupling efficiency. We measure the contribution of coincidences due to accidentals by introducing an electronic time delay between the events at both detectors larger than the coincidence window, thus capturing the coincidence counts from uncorrelated pairs. After subtracting these measured accidentals the average coincidence rate far from zero delay is then 39.4 ± 0.9 cph, as shown in Figure 4.13. The average number of coincidences far from the region of zero time delay is a weighted mean over the twelve data points present in the off dip region (six on the left and six on the right of the HOM dip), where the weights are the standard deviation

of each data point shown in Figure 4.13. On the other hand, at zero delay the detected coincidences drop to 10.7 ± 5.1 cph, where the reported error bar corresponds to its standard deviation. This leads to an overall visibility for the plasmonic HOM dip of $V_{SPP} = 0.72 \pm 0.13$. The observed dip confirms that single SPPs bunch together as bosons and as the visibility is larger than 0.5 in our experiment this also confirms that quantum interference is involved in the bunching process [62, 63]. The plasmonic visibility is again limited mainly by the large bandwidth of the IF's in our experiment and the resolution of the time delay used. Any loss due to radiative scattering at the beamsplitter (measured to be less than 10%) can be included within the coefficient η_{out} and therefore does not play a role in reducing the visibility [61]. Finally, note that when the coincidence rate drops as the single SPPs are interfering, the count rate at each APD remains unchanged, as shown in the inset of Figure 4.13. This is due to the small proportion of *pairs* of single excitations (as compared to the total count rate) that survive the entire process of propagation, splitting and out-coupling: in most cases at least one of the excitations from a pair will be lost in the process. Therefore the count rate at each APD allows the efficiency of the system to be monitored to ensure the HOM dip is not caused by loss fluctuations.

4.2.3 Conclusions

In this work we used single photons generated via parametric down conversion to excite single SPPs on a metallic stripe beamsplitter. The SPPs interacted via a scattering process and we directly observed the HOM effect. The SPPs showed a distinct bunching behaviour as expected for bosons, with the results clearly showing quantum interference is involved in the process. Our investigation confirms the bosonic nature of single SPPs in the quantum regime and opens up new opportunities for controlling quantum states of light in ultra-compact nanophotonic plasmonic circuitry.

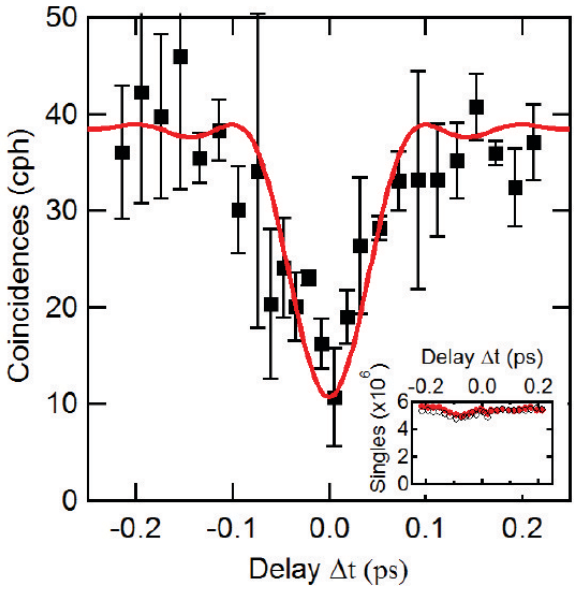


Figure 4.13: Plasmonic Hong-Ou-Mandel dip. Black squares: coincidence rate as a function of time delay Δt. The red curve is a theoretical fit, $N(\Delta t)$, based on the coincidence probability $P(\Delta t)$ corrected for accidentals. From the theory fit we extract a coherence time for the single SPPs of $\sim 0.1ps$, which is consistent with the coherence time obtained from our measured photonic dip. This confirms that during the photon-SPP conversion process thecoherence properties of the single-photon wavepackets and the single SPPs are similar, and that the wavepacket has not been significantly altered by either the conversion process or propagation in the plasmonic media. The bottom-right inset shows the singles rates (in cph) as a function of Δt: red disks for detector B_1 and black circles for B_2. The visibility obtained from the plasmonic dip is $V_{SPP} = 0.72 \pm 0.13$.

Chapter 5

Conclusions and Future work

In this thesis we gave a brief overview of the physics of surface plasmon polaritons (SPPs) at metal/insulator interface focusing our attention on the excitation of SPPs and their propagation along metal stripes. We used this knowledge in order to introduce the work that we have done on quantum statistics of surface plasmon polaritons in metallic stripe waveguides and on quantum interference in the plasmonic Hong-Ou-Mandel effect.

We study the quantum properties of SPPs by using single photon generators as sources of light. After an introduction on the meaning of coherence functions, we explained how we couple photons into a gold waveguides with gratings on both sides, where the coupled plasmon is confined at the interface between gold and air.

By measuring the second-order quantum coherence function $g^{(2)}$, we demonstrated the ability to excite single SPPs. Moreover, the effect of losses incurred during propagation of the single SPPs is consistent with the classical exponential behaviour and does not change the value of $g^{(2)}$, providing evidence that a linear uncorrelated Markovian loss model is valid for SPP damping at the single quanta level. Our results imply that building longer and more complex SPP waveguide structures operating in the quantum regime is realistic and opens up the possibility for future studies of new types of functioning devices based on quantum plasmonics.

Therefore, we moved onto more complicated stripe designs, such as X-shaped stripes, in order to observe nonclassical effects in the interference of two plasmons. Over the past few years there have been many works on con-

structing different types of scattering/interaction scenario for surface plasmons. These include Y- and X-shape waveguides, periodically structured media, interfaces made from basic dielectric media and more exotic anisotropic metamaterials. Performing an experiment probing the interaction of two single surface plasmons with each other is an important step along the way to understanding better the behaviour of single surface plasmons at the quantum level and how one can build more complicated quantum interference networks, such as plasmonic-based quantum logic gates. A natural thing to probe in the most basic type of scatterer (a 50/50 beamsplitter) operating quantum mechanically, is how it acts on two separate single surface plasmons. In this thesis we showed how we focused single photons onto separate gratings at the inputs of an X-shaped plasmonic beamsplitter, and converted into SPPs due to phase-matching conditions. We made them interact via a scattering process and we directly observed the plasmonic HOM effect. The SPPs showed a distinct bunching behaviour as expected for bosons, with the results clearly showing quantum interference is involved in the process. Our investigation confirms the bosonic nature of single SPPs in the quantum regime and opens up new opportunities for controlling quantum states of light in ultra-compact nanophotonic plasmonic circuitry.

This important result will allow us to proceed to the next stage of building stable quantum logic gates, as the interference of two surface plasmons would be a core component. It would also open up the possibility of testing more complex interference effects involving three or more single surface plasmon.

In the future, we are also planning to work on nanophotonic quantum transfer of single plasmons. The aim is to demonstrate the transfer of single plasmon excitations across a nanoparticle array. The transfer of plasmonic fields via an array of coupled metallic nanoparticles has received much attention over the past few years [78][87]. Recent experimental evidence has now confirmed that this is indeed possible [88]. Such arrays can perform interesting operations such as entanglement generation [89] and nonlinear absorption [90]. However, it is not yet known if one can achieve this type of transfer right down at the single plasmon level using quantum plasmonic

states. This would be an important advancement as it would open up the possibility of developing techniques for controlling and maintaining the quantum coherence of light in truly nanophotonic devices. Applications include building scalable networks for quantum information processing with much smaller footprints than currently achievable, investigating many-body quantum phenomena of interacting nanoparticles, for instance quantum phase transitions and probing fundamental aspects of quantum mechanics such as fermionic and bosonic behaviour. The major question which this experiment would seek to answer is if we transfer single plasmon excitations across a nanoparticle array and, if so, how well. The experiment could use a single photon to couple to a single plasmon on the nanoparticle waveguide, with the other photon from the PDC as the trigger, as in the previous experiments. Possible things to investigate include intensity and quantum statistical measures such as $g^{(2)}(\tau)$. This work will provide the first evidence for the transfer of single plasmon quantum excitations across a nanoparticle array. It would open up the possibility of developing techniques for controlling and maintaining the quantum coherence of light in truly nanophotonic applications, such as nanoscale optical quantum information processing and many-body plasmonic quantum phenomena. Future work would be to also use frequency or energy-time entangled states in order to probe deeper into the symmetric and antisymmetric features of surface plasmon wavefunctions. Moreover, the study of confined and more 'electronic' SPPs in the quantum regime, would be interesting in order to see whether we depart from the Markovian description of the loss processes.

Bibliography

[1] R. Loudon, Phis. Rev. A **58**, 4904 (1998).

[2] A.L.Schawlow & H. Townes, Phys. Rev. **112**, 1940 (1958).

[3] L.S. Brown & G. Gabrielse, Rev. Mod. Phys. **58**, 233 (1986).

[4] S. Chu, Rev. Mod. Phys. **70**, 685 (1998).

[5] W.D. Phillips, Rev. Mod. Phys. **70**, 707 (1998).

[6] C.N. Cohen-Tannoudji, Rev. Mod. Phys. **70**, 707 (1998).

[7] C.E. Wieman , D.E. Pritchard & D.J. Wineland, Rev. Mod. Phys. **71**, 253 (1999).

[8] H.J. Metcalf & P. van der Straten, *Laser Cooling and Trapping* (Springer, Berlin, 2001).

[9] W. Ketterle, Rev. Mod. Phys. **74**, 1131 (2002).

[10] M.A. Kastner, Rev. Mod. Phys. **64**, 849 (1992).

[11] Y. Makhlin, G. Schon & A. Shnirman, Rev. Mod. Phys. **73**, 357 (2001).

[12] A. Zeilinger, G. Weihs, T. Jennewien & M. Aspelmeyer, Nature **433**, 230 (2005).

[13] G.E. Moore, Electronics **19**, April (1965).

[14] P.A. Benioff, J. Stat. Phys. **22**, 563 (1980).

[15] P.A. Benioff, Int. J. Theor. Phys. **21**, 177 (1982).

[16] P.A. Benioff, Phys. Rev. Lett. **48**, 1581 (1982).

[17] R.P. Feynman, Int. J. Theor. Phys. **21**, 467 (1982).

[18] D. Deutsch, Proc. Roy. Soc. Lond. **A 400**, 97 (1985).

[19] D.P. Di Vincenzo, *Topics in Quantum Computers* (Kluwer Ac. Publ., Dordrecht, 1997).

[20] D. K. Gramotnev & S. I. Bozhevolnyi, Nature Photonics **4**, 83 (2010).

[21] V. Giannini *et al.*, Small **6**, 2498 (2010).

[22] S. Kawata, Y. Inouye & P. Verma, Nature Photonics **3**, 388 (2009).

[23] J. N. Anker *et al.*, Nature Materials **7**, 442 (2008).

[24] H. A. Atwater & A. Polman, Nat. Mat. **9**, 205 (2010).

[25] M. S. Tame *et al.*, Nature Physics **9**, 329 (2013).

[26] A.V. Akimov, A. Mukherjee, C.L. Yu, D.E. Chang, A.S. Zibrov, P.R. Hemmer, H. Park & M.D. Lukin, Nature **450**, 402 (2007).

[27] A. S.; Demler E. A.; Lukin M. D. Chang, D. E.; Sorensen, Nature Phys. **3**, 807 (2007).

[28] N. P. de Leon, M. D. Lukin & H. Park, IEEE Sel. Top. Quant. Elec. **18**, 1781 (2012).

[29] M. L. Brongersma & V. M. Shalaev, Science **328**, 440 (2010).

[30] H. Raether, *Surface Plasmons on Smooth and Rough Surfaces and on Gratings* (Springer-Verlag, Berlin Heidelberg, 1986).

[31] S. Maier, *Plasmonics: Fundamentals and Applications* (Springer, United Kingdom, 2007).

[32] E. Kretschmann & H. Raether, Z. Naturf. **23A**, 2135 (1968).

[33] A. Otto, Z. Phys. **216**, 398 (1968).

[34] A. Bouhelier & S.R. Wiederrecht, Opt. Lett. **30**, 884 (2005).

[35] Hecht B., Bielefeld H., Novotny L., Inouye Y. & Pohl D. W., Phys. Rev. Lett. **77**, 1889 (1996).

[36] H. Ditlbacher, J. R. Krenn, A. Hohenau, A. Leitner & F. R. Aussenegg, Appl. Phys. Lett. **83**, 3665 (2003).

[37] E. Devaux, T. W. Ebbesen, J-C. Weeber & A. Dereux, Appl. Phys. Lett. **83**, 24 (2003).

[38] I. P. Radko, S. I. Bozhevolnyi, G. Brucoli, L. Martín-Moreno, F. J. García-Vidal & A. Boltasseva, Phys. Rev. B **78**, 115115 (2008).

[39] J.D. Jackson, *Classical Electrodynamics* (Wiley, New York, 1962).

[40] G. Lévêque & O. J. F. Martin, J. Appl. Phys. **100**, (1996).

[41] H. Kapitza, Opt. Comm. **16**, 1 (1976).

[42] P. Berini, Phys. Rev. B **61**, 10484 (2000).

[43] J.C.Weeber, J.R.Krenn, A.Dereux, B.Lamprecht, Y.Lacroute & P.Goudonnet, Phys. Rev. B **64**, 045411 (2001).

[44] J.C.Weeber, Y.Lacroute & A.Dereux, Phys. Rev. B **68**, 115401 (2003).

[45] R. Zia, J. A. Shuller & M. L. Brongersma, Phys. Rev. B **74**, 165415 (2006).

[46] E. Altewischer, M.P. van Exter & J.P. Woerdman, Nature **418**, 304 (2002).

[47] F. J.; Erni D.; Cirac J. I.; Martín-Moreno L. Moreno, E.; García-Vidal, Phys. Rev. Lett. **92**, 236801 (2004).

[48] F.; Moreno E.; Erni D.; Gisin N.; Zbinden H. Fasel, S.; Robin, Phys. Rev. Lett. **94**, 110501 (2005).

[49] M.; Gisin N.; Zbinden H. Fasel, S.; Halder, New J. Phys. **8**, 13 (2006).

[50] S.; Lodahl P.; Sørensen A. S.; Boltasseva A.; Janousek-J.; Andersen-U. L. Huck, A.; Smolka, Phys. Rev. Lett. **102**, 246802 (2009).

[51] R. Kolesov, B. Grotz, G. Balasubramanian, R.J. Stï¿½hr, A.A.L. Nicolet, P.R. Hemmer, F. Jelezko & J. Wrachtrup, Nature **5**, 470 (2009).

[52] R.W. Heeres, S.N. Dorenbos, B. Koene, G.S. Glenn, L.P. Kouwenhoven & V. Zwiller, Nano Letters **10**, 661 (2010).

[53] Abram L. Falk, Frank H. L. Koppens, Chun L. Yu, Kibum Kang, Nathalie de Leon Snapp, Alexey V. Akimov, Moon-Ho Jo, Mikhail D. Lukin& Hongkun Park, Nature Physics **5**, 475 (2009).

[54] J.A. Scholl , A.L. Koh & J.A. Dionne, Nature **483**, 421 (2012).

[55] J. Zuloaga , E. Prodan & P. Nordlander, Nano Latt. **12**, 429 (2012).

[56] K.J. Savage, M.M. Hawkeye, R. Esteban, A.G. Borisov, J. Aizpurua & J.J. Baumberg, Nature **491**, 574 (2012).

[57] Hong C.K., Ou Z.Y. , Mandel L., Phys. Rev. Lett. **59**, 18 (1987).

[58] G. Fujii *et al.*, Opt. Lett. **37**, 1535 (2012).

[59] R. W. Heeres, L. P. Kouwenhoven & V. Zwiller, Nature Nanotechnology AOP (2013).

[60] Y.S. Fim *et al.*, arXiv:1309.3017 (2013).

[61] D. Ballester, M. S. Tame & M. S. Kim, Phys. Rev. A **82**, 012325 (2010).

[62] Mandel L., Reviews of Modern Physics **71**, 274 (1999).

[63] R. Ghosh & L. Mandel, Phys. Rev. Lett. **59**, 1903 (1987).

[64] C.C.Gerry & P.L.Knight, *Introductory quantum optics* (Cambridge University press, Cambridge, 2004).

[65] J. F. Clauser, Phys. Rev. D **9**, 853 (1974).

[66] F. Diedrich & H. Walther, Phys. Rev. Lett. **58**, 203 (1987).

[67] Burnham D.C., Weinberg D.L., Phys. Rev. Lett. **25**, 84 (1970).

[68] Hong C.K., Mandel L., Phys. Rev. Lett. **56**, 58 (1986).

[69] D.A. Pines, Phys. Rev. **92**, 626 (1953).

[70] J.G. Rarity, P.R. Tapster & R. Loudon, J. Opt. B: Quantum Semiclass. Opt. **7**, S171 (2005).

[71] R. Loudon, *The Quantum Theory of Light* (Oxford University Press, Oxford, 2000).

[72] E. Bocquillon *et al.*, Science **339**, 1054 (2013).

[73] S. Baek & Y. Kim, Phys. Rev. A **77**, 043807 (2008).

[74] Thorn J. J., Neel M. S., Donato V. W., Bergreen G. S., Davies R. E., Beck M., Am. J.Phys. **72**, 1210 (2004).

[75] R.Zia, M.D.Selker & M.L.Brongersma, Phys. Rev. B **71**, 165431 (2005).

[76] B. Lamprecht *et al.*, Appl. Phys. Lett. **79**, 51 (2001).

[77] J.C. Weeber, M. U. González, A.L. Baudrion & A. Dereux, Appl. Phys. Lett. **87**, (2005).

[78] M. Quinten, A. Leitner, J.R. Krenn, F.R. Aussenegg, Opt. Lett. **23**, 1331 (1998).

[79] H. Ditlbacher, J. R. Krenn, G. Schider, A. Leitner & F. R. Aussenegg, Appl. Phys. Lett. **81**, (2002).

[80] M. U. González, J.C. Weeber, A.L. Baudrion, A. Dereux, A. L. Stepanov, J. R. Krenn, E. Devaux & T. Ebbesen, Phys. Rev. B **73**, (2006).

[81] J. A. Sánchez-Gil & A. A. Maradudin, Appl. Phys. Lett. **86**, (2005).

[82] Hockel D., Koch L. & Benson, O. Phys. Rev. A **83**, 013802 (2011).

[83] Tame M. S., Lee C., Lee J., Ballester D., Paternostro M., Zayats A. V., Kim M. S., Phys. Rev. Lett. **101**, 190504 (2008).

[84] M.L. Brongersma, J.W. Hartman & H.H. Atwater, Molecular Electronics Symposium Boston, MA, USA (29 Nov. - 2Dic).

[85] Zambra, Andreoni, Bondani, Gramegna, Genovese, Brida, Rossi & Paris, Phys. Rev. Lett. **95**, 063602 (2005).

[86] G. Di Martino, Y. Sonnefraud, S. KenaCohen, M. Tame, S.K. Ozdemir, M.S. Kim & S.A. Maier, Nanoletters **12**, 2504 (2012).

[87] M. L. Brongersma, J. W. Hartman, H. A. Atwater, Phys. Rev. B **62**, R16356 (2000).

[88] S.A. Maier, P.G. Kik, H.A. Atwater, S. Meltzer, E. Harel, B.E. Koel & A.A.G. Requicha, Nature Materials **2**, 229 (2003).

[89] C. Lee, M. Tame, C. Noh, J. Lim, S.A. Maier, J. Lee & D.G. Angelakis, New J. Phys. **15**, 083017 (2013).

[90] K. Wang, H. Long, M. Fu, G. Yang & P. Lu, Opt. Lett. **35**, 10 (2010).

[91] A. Drezet, A. Hohenau, A.L. Stepanov, H. Ditlbacher, B. Steinberger, N. Galler, F.R. Aussenegg, A. Leitner & J.R. Krenn, App. Phys. Lett. **89**, 091117 (2006).

[92] V. Ferry et al., Appl. Phys. Lett. **95**, 183503 (2009).

[93] J.C. Weeber, Y. Lacroute, A. Dereux, E. Devaux, T. Ebbesen, C. Girard, M. U. González & A.L.Baudrion, Phys. Rev. B **70**, (2004).

[94] A. Politi et al., Science **320**, 646 (2008).

[95] B. Lamprecht, J.R. Krenn, A. Leitner & F.R. Aussenegg, Appl. Phys. B **69**, 223 (1999).

[96] I. Avrutsky, Phys. Rev. B **70**, 155416 (2004).

[97] H. Berger, Solid State Electronics **15**, 145 (1975).

[98] C. Chen & P. Berini, IEEE Photonics Technology Letters **21**, 1831 (2009).

[99] Israel De Leon & Pierre Berini, Nature Photonics **4**, 382 (2010).

[100] P. Berini, Phys. Rev. B **63**, 125417 (2001).

[101] A. Brenier, J. of Luminescence **92**, 199 (2001).

[102] R. Zia, J.A. Schuller & M.L. Brongersma, Materials Today **9**, 20 (2006).

[103] A. Hamel , B. Hadjoudja , B. Chouial & A. Chibani, J. Mater. Sci. **1**, 8 (2009).

[104] A. Hamel & A. Chibani, J. Appl. Sci. **10**, 231 (2010).

[105] P.B. Johnson & R.W. Christy, Phys. Rev. B **6**, 4370 (1972).

[106] L. Birotheau, A. Izrael, J. Y. Marzin, R. Azoulay, V. Thierry-Mieg & F. R. Ladan, Appl. Phys. Lett. **61**, 3023 (1992).

[107] Brunner K, Bockelmann U, Abstreiter G, Walther M, Bohm G, Trankle G & Weimann G, Phys. Rev. Lett. **69**, 3216 (1992).

[108] M. Orrit & J. Bernard, Phys. Rev. Lett. **65**, 2716 (1990).

[109] M. Kirkengena, J. Bergli & Y.M. Direct, J. Appl. Phys. **102**, 093713 (2007).

[110] W.L. Barnes, A. Dereux & T.W. Ebbesen, Nature **424**, 824 (2003).

[111] J. Seidel, S. Grafström & L. Eng, Phys. Rev. Lett. **94**, 177401 (2005).

[112] M.P. Nezhad, K. Tetz & Y. Fainman, Opt. Express **12**, 4072 (2004).

[113] U. Fano, Phys. Rev. **103**, 1202 (1956).

[114] J. Grandidier, G.C. des Francs, S. Massenot, A. Bouhelier, L. Markey, J. Weeber, C. Finot & A. Dereux, Nano Letters **9**, 2935 (2009).

[115] J.C. Maxwell Garnett, Philos. Trans. R. Soc. London **203**, 385 (1904).

[116] S. Pillai, K. R. Catchpole, T. Trupke & M. A. Green, J. Appl. Phys. **101**, 093105 (2007).

[117] R.H. Rithchie, E.T. Arakawa, J.J. Cowan & R.N. Hamm, Phys. Rev. Lett. **21**, 1530 (1968).

[118] Z. Wang, Y. Tang, L. Wosinski & S. He, IEEE Photonics Technology Letters **22**, 1568 (2010).

[119] N.C. Lindquist, W.A. Luhman, S.H. Oh & R.J. Holmes, Appl. Phys. Lett. **93**, 123308 (2008).

[120] C.F. Bohren & D.R. Huffman, *Absorption and scattering by small particles* (Wiley, New York, 1983).

[121] C.Hagglund, M. Zach, G. Petersson & B. Kasemo, Appl. Phys. Lett. **92**, 053110 (2008).

[122] Mark L. Brongersma & Pieter G. Kik, *Surface Plasmon Nanophotonics* (Springer, Dordrecht, The Netherlands, 2007).

[123] M. Hamasaki, T. Adachi, S. Wakayama & M. Kikuchi, J. Appl. Phys. **49**, 3987 (1978).

[124] M. Hamasaki, T. Adachi, S. Wakayama & M. Kikuchi, Solid State Commun. **21**, 591 (1977).

[125] J. Takahara, S. Yamagishi, H. Taki, A. Morimoto & T. Kobayashi, Opt. Lett. **22**, 475 (1997).

[126] H. Kretschmann, E. & Raether, Z. Naturforschung **23A**, 2135 (1968).

[127] Paul G. Kwiat, Klaus Mattle, Harald Weinfurter, Anton Zeilinger, Alexander V. Sergienko, and Yanhua Shih, Phys. Rev. Lett. **75**, 4337 (1995).

[128] A.J. Morfa, K.L. Rowlen, M.J. Romero & J. Van de Lagemaat, Appl. Phys. Lett. **92**, 013504 (2008).

[129] H.J. Simon , D.E. Mitchell & J.G. Watson, Phys. Rev. Lett. **33**, 1531 (1974).

[130] T.H. Cormen, C.E. Leiserson & R.L. Rivest, *Introduction to Algorithms* (MIT Press, Cambridge, MA, 1990).

[131] P. Shor, SIAM J. Comput. **26**, 1484 (1997).

[132] L.K. Grover, Phys. Rev. Lett. **79**, 325 (1997).

[133] S. Wiesner, SIGNAT News **15**, 178 (1983).

[134] C.H. Bennett & G. Brassard, Proceedings of IEEE International Confer- ence on Computers, System and Signal Processing **175**, (1984).

[135] N. Gisin, G. Ribody, W. Tittel & H. Zbinden, Rev. Mod. Phys. **74**, 145 (2002).

[136] A. Ekert, Phys. Rev. Lett. **67**, 661 (1991).

[137] M. Hillery, V. Buzek & A. Berthiaume, Phys. Rev. A **59**, 1829 (1999).

[138] H. Buhrman, R. Cleve, J. Watrous & R. de Wolf, Phys. Rev. Lett. **87**, 167902 (2001).

[139] *http://qist.lanl.gov* (Quantum Computing Roadmap Overview, Quantum Information Science and Technology Roadmap Project, Quantum Information Science Technology Experts Panel, Los Alamos National Lab, 1994).

[140] M.C. Gather, K. Meerholz, N. Danz & K. Leosson, Nature Photonics **4**, 457 (2010).

[141] D. E. Chang, A. S. Sørensen, E. A. Demler & M.D. Lukin, Nature Physics **3**, 807 (2010).

[142] E. Macia, Rep. Prog. Phys. **69**, 397 (2006).

[143] Michael D. McGehee, Rahul Gupta, Siegfried Veenstra, E. Kirk Miller, María A. Díaz-García, and Alan J. Heeger, Phys. Rev. B **58**, 7035 (1998).

[144] M. Fleischmann, P.J. Hendra& A.J. McQuillan, Chem. Phys. Lett. **26**, 163 (1974).

[145] G. Mie, Ann. Phys. **25**, 377 (1908).

[146] R. Dallapiccola , A. Gopinath, F. Stellacci & L. Dal Negro, Opt. Exp. **16**, 5261 (2008).

[147] S. Y. K. Lee, J. J. Amsden, S. V. Boriskina, A. Gopinath, A. Mitropoulos, D. L. Kaplan, F. G. Omenetto & L. Dal Negro, Proc. Natl. Acad. Sci. USA **107**, 12086 (2010).

[148] S. M. Sze & K. K. Ng, *Physics of Semiconductor Devices* (John Wiley & Sons, New Jersey, 2007).

[149] S. Knief & W. von Niessen, Phys. Rev. B **59**, 12940 (1999).

[150] A. Purwanto, W. Wang, T. Ogi, I.W. Lenggoro, E. Tanabe & K. Okuyama, J. of Alloys ans Compounds **463**, 350 (2008).

[151] G. Roger & A. Aspect P. Grangier, Europhys. Lett. **1**, 173 (1986).

[152] T.W. Ebbesen, H.J. Lezec, H.F. Ghaemi, T. Thio & P.A.Wolff, Nature **391**, 667 (1998).

[153] L. Dal Negro, P. Bettotti, M. Cazzanelli, D. Pacifici & L. Pavesi, Optics Communications **229**, 337 (2004).

[154] J. Pendry, Phys. Rev. Lett. **85**, 396 (2000).

[155] K. R.Catchpole & A. Polman, Appl. Phys. Lett. **93**, 191113 (2008).

[156] W. Shockley & H.J. Queisser, J. Appl. Phys. **32**, 510 (1961).

[157] Y. Li, H. Barry Harrison & G.K. Reeves, Microelectronics Journal **29**, 21 (1998).

[158] L. Kroon, E. Lennholm & R. Riklund, Phys. Rev. B **66**, 094204 (2002).

[159] R.H. Rithchie, Phys. Rev. **106**, 874 (1957).

[160] J.M. Elson & R.H. Ritchie, Phys. Rev. B **4**, 4129 (1971).

[161] A. Goetzberger, C. Hebling & H.W. Schock, Mater. Sci. Eng. **40**, 1 (2003).

[162] D. Haranath, H. Chander, P. Sharma & S. Singh, Appl. Phys. Lett **89**, 173118 (2006).

[163] J. Strong, *Procedures in Experimental Physics* (Prentice-Hall, New York, 1938).

[164] S. M. Sze, *Semiconductor devices physics and technology* (John Wiley & Sons, New York, 2001).

[165] M.L. Tarng, J. Appl. Phys. **49**, 4069 (1978).

[166] B.E.A. Saleh & M.C. Teich, *Fundamentals of photonics, Second edition* (Wiley, New York, 2007).

[167] R. Hanbury Brown & R. Q. Twiss, Nature **177**, 27 (1956).

[168] S.L. Cunningham, A.A. Maradudin & R.F. Wallis, Phys. Rev. B **10**, 3342 (1974).

[169] R.W. Wood, Phil. Mag. **4**, 396 (1902).

[170] U. Kreibig & P. Zacharias, Z. Phys. **231**, 128 (1970).

[171] A.V. Krasavin, T.P. Vo, W. Dickson, P.M. Bolger & A.V. Zayats, Nano Letters **11**, 6 (2011).

[172] A.V. Zayats , I.I. Smolyaninov & A.A. Maradudin, Phys. Rep. **408**, 131 (2005).

[173] M. Ambati, S.H. Nam, E. Ulin-Avila, D.A. Genov, G. Bartal & Xiang Zhang, Nano Letters **8**, 3998 (2008).

Appendices

The aim of this last chapter is to give a brief overview on the results obtained from side projects that were part of this PhD program. Since these projects have not represented the central topic of the PhD, we decided to include them in the appendix and not in the main body of this thesis.

The linking technique used in these works is the leakage radiation microscopy (LRM), briefly introduced in section 1.2.2.

Leakage radiation microscopy is a technique that allows imaging SPPs with an easier setup compared to SNOM and fluorescence imaging techniques. LRM can both be used to image the direct space and Fourier space, namely the SPP wave vectors [91]. The basic setup of LRM is as shown in Figure 5.1.

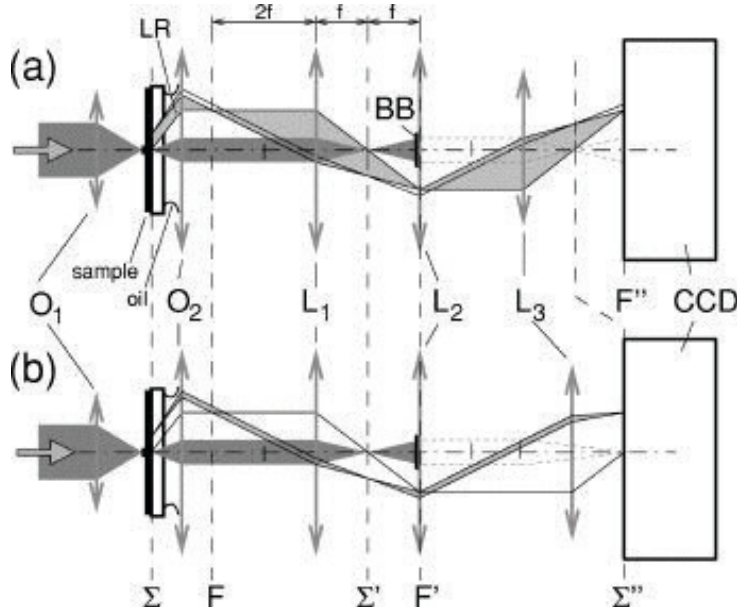


Figure 5.1: Leakage Radiation Microscopy setup [91].

The sample is illuminated by a low numerical aperture (NA) objective

O_1 (NA = 0.5). Index matching oil is used in the near vicinity of glass side in order to collect leakage radiation signal going out with a different angle than the incident beam. Since the leakage radiation beam direction is highly tilted from the optical axis, a high NA objective O_2 (NA = 1.45) is used after immersion oil. High NA is achieved by a Total Internal Reflection Fluorescence (TIRF) objective. The back focal point of this objective resides somewhere in the objective. Since the main goal of the leakage radiation microscopy is to block the incident beam in the Fourier plane in order to obtain a clear SPP signal, an optical system consisting of 3 lenses must be used to obtain a Fourier plane outside the objective and re-image it on a CCD camera.

The $2f$ point of the first lens L_1 coincides with the Fourier plane in the objective O_2 to obtain Sample plane Σ at the back focal plane of the lens L_1 and more importantly, Fourier plane F' at $2f$ distance where another lens L_2 resides. According to the position of the third lens L_3, either Fourier plane F'', see Figure 5.1(a), or Sample plane Σ'', see Figure 5.1(b), is imaged on the CCD camera. The lenses used all have the same focal distance f = 7.5 cm in our experiment. It is possible to select SPP beams propagating along specific directions, or the incident light, and block them with a mask in Fourier plane F' since it resides outside the objective unlike the Fourier plane F. For instance, it is desirable to block the incident laser beam after the excitation since it decreases the imaging quality due to over exposure and creates interference with the SPP signal. As it is not separable in the Sample plane image, it is feasible to block the designated beam in the Fourier plane. In order to take images from the Sample plane with white light illumination, a beam splitter is inserted before O_1 and illuminated by a light source.

A deeper understanding of the technique will be found in the following pages together with the main findings of these research projects. In particular, two main topic have been studied: directional excitation of surface plasmon polaritons via nanoslits under varied incidence and unidirectional side scattering of light by a single-element nanoantenna.

Directional excitation of surface plasmon polaritons *via* nanoslits under varied incidence observed using leakage radiation microscopy

Yannick Sonnefraud,* Sarp Kerman, Giuliana Di Martino, Dang Yuan Lei, and Stefan A. Maier

Experimental Solid State Group, Physics Department, Imperial College London, London SW7 2AZ, UK

*y.sonnefraud@imperial.ac.uk

Abstract: Surface Plasmon Polaritons (SPPs) are excited at the interface between a thin gold film and air *via* the illumination of nanoslits etched into the film. The coupling efficiency to the two propagation directions away from the slits is determined by leakage radiation microscopy, when the angle of incidence of the pump beam is changed from 0° to 20°. We find that preferential coupling of SPPs into one direction can be achieved for non-normal incidence in the case of single slits and slit pairs. The proportion of SPP excited into one direction can be in excess of 90%. We further provide a simple model of the process, and directly compare the performances of the two approaches.

© 2012 Optical Society of America

OCIS codes: (070.0070) Fourier optics and signal processing; (180.0180) Microscopy; (240.6680) Surface plasmons.

References and links

1. S. A. Maier, *Plasmonics: Fundamentals And Applications* (Springer-Verlag New York Inc., 2007).
2. S. Maier, "Effective mode volume of nanoscale plasmon cavities," Opt. Quantum Electron. **38**, 257–267 (2006).
3. M. L. Brongersma and V. M. Shalaev, "The case for plasmonics," Science **328**, 440–441 (2010).
4. D. Egorov, B. S. Dennis, G. Blumberg, and M. I. Haftel, "Two-dimensional control of surface plasmons and directional beaming from arrays of subwavelength apertures," Phys. Rev. B **70**, 033404 (2004).
5. J.-Y. Laluet, E. Devaux, C. Genet, T. W. Ebbesen, J.-C. Weeber, and A. Dereux, "Optimization of surface plasmons launching from subwavelength hole arrays: modelling and experiments," Opt. Express **15**, 3488–3495 (2007).
6. I. P. Radko, S. I. Bozhevolnyi, G. Brucoli, L. Martín-Moreno, F. J. García-Vidal, and A. Boltasseva, "Efficient unidirectional ridge excitation of surface plasmons," Opt. Express **17**, 7228–7232 (2009).
7. N. Bonod, E. Popov, L. Li, and B. Chernov, "Unidirectional excitation of surface plasmons by slanted gratings," Opt. Express **15**, 11427–11432 (2007).
8. B. Bai, X. Meng, J. Laukkanen, T. Sfez, L. Yu, W. Nakagawa, H. P. Herzig, L. Li, and J. Turunen, "Asymmetrical excitation of surface plasmon polaritons on blazed gratings at normal incidence," Phys. Rev. B **80**, 035407 (2009).
9. A. Roszkiewicz and W. Nasalski, "Unidirectional SPP excitation at asymmetrical two-layered metal gratings," J. Phys. B **43**, 185401 (2010).
10. A. Baron, E. Devaux, J.-C. Rodier, J.-P. Hugonin, E. Rousseau, C. Genet, T. W. Ebbesen, and P. Lalanne, "Compact antenna for efficient and unidirectional launching and decoupling of surface plasmons," Nano Lett. **11**, 4207–4212 (2011).
11. P. Lalanne, J. P. Hugonin, and J. C. Rodier, "Theory of surface plasmon generation at nanoslit apertures," Phys. Rev. Lett. **95**, 263902 (2005).

#159589 - $15.00 USD Received 9 Dec 2011; revised 5 Jan 2012; accepted 9 Jan 2012; published 13 Feb 2012
(C) 2012 OSA

12. H. Liu, P. Lalanne, X. Yang, and J.-P. Hugonin, "Surface plasmon generation by subwavelength isolated objects," IEEE J. Sel. Top. Quantum Electron. **14**, 1522 (2008).
13. M. W. Maqsood, R. Mehfuz, and K. J. Chau, "High-throughput diffraction-assisted surface-plasmon-polariton coupling by a super-wavelength slit," Opt. Express **18**, 21669–21677 (2010).
14. D.-S. Kim, J. Heo, S.-H. Ahn, S. W. Han, W. S. Yun, and Z. H. Kim, "Real-space mapping of the strongly coupled plasmons of nanoparticle dimers," Nano. Lett. **9**, 3619–3625 (2009).
15. J. Chen, Z. Li, S. Yue, and Q. Gong, "Efficient unidirectional generation of surface plasmon polaritons with asymmetric single-nanoslit," Appl. Phys. Lett. **97**, 041113 (2010).
16. J. Chen, Z. Li, S. Yue, and Q. Gong, "Ultracompact surface-plasmon-polariton splitter based on modulations of quasicylindrical waves to the total field," J. Appl. Phys. **109**, 073102 (2011).
17. F. López-Tejeira, S. G. Rodrigo, L. Martín-Moreno, F. J. García-Vidal, E. Devaux, T. W. Ebbesen, J. R. Krenn, I. P. Radko, S. I. Bozhevolnyi, M. U. González, J. C. Weeber, and A. Dereux, "Efficient unidirectional nanoslit couplers for surface plasmons," Nat. Phys. **3**, 324 (2007).
18. X. Li, Q. Tan, B. Bai, and G. Jin, "Experimental demonstration of tunable directional excitation of surface plasmon polaritons with a subwavelength metallic double slit," Appl. Phys. Lett. **98**, 251109 (2011).
19. T. Xu, Y. Zhao, D. Gan, C. Wang, C. Du, and X. Luo, "Directional excitation of surface plasmons with subwavelength slits," Appl. Phys. Lett. **92**, 101501 (2008).
20. Y. Wang, L. Wang, J. Liu, X. Zhai, L. Wang, D. Xiang, Q. Wan, and B. Meng, "Plasmonic surface-wave bidirectional splitter in different angles of incident light," Opt. Commun. **283**, 1777 – 1779 (2010).
21. G. Lerosey, D. F. P. Pile, P. Matheu, G. Bartal, and X. Zhang, "Controlling the phase and amplitude of plasmon sources at a subwavelength scale," Nano Lett. **9**, 327–331 (2009).
22. Y. Wang, X. Zhang, H. Tang, K. Yang, Y. Wang, Y. Song, T. huei Wei, and C. H. Wang, "A tunable unidirectional surface plasmon polaritons source," Opt. Express **17**, 20457–20464 (2009).
23. M.-D. He, Z.-Q. Gong, S. Li, Y.-F. Luo, J.-Q. Liu, and X. Chen, "Plasmonic coupler based on the nanoslit with bump," Opt. Commun. **284**, 368 – 372 (2011).
24. H. W. Kihm, K. G. Lee, D. S. Kim, J. H. Kang, and Q.-H. Park, "Control of surface plasmon generation efficiency by slit-width tuning," Appl. Phys. Lett. **92**, 051115 (2008).
25. B. Wang, L. Aigouy, E. Bourhis, J. Gierak, J. P. Hugonin, and P. Lalanne, "Efficient generation of surface plasmon by single-nanoslit illumination under highly oblique incidence," Appl. Phys. Lett. **94**, 011114 (2009).
26. H. F. Schouten, N. Kuzmin, G. Dubois, T. D. Visser, G. Gbur, P. F. A. Alkemade, H. Blok, G. W. t. Hooft, D. Lenstra, and E. R. Eliel, "Plasmon-assisted two-slit transmission: Young's experiment revisited," Phys. Rev. Lett. **94**, 053901 (2005).
27. A. Bouhelier, T. Huser, H. Tamaru, H.-J. Güntherodt, D. W. Pohl, F. I. Baida, and D. Van Labeke, "Plasmon optics of structured silver films," Phys. Rev. B **63**, 155404 (2001).
28. A. Drezet, A. Hohenau, A. L. Stepanov, H. Ditlbacher, B. Steinberger, N. Galler, F. R. Aussenegg, A. Leitner, and J. R. Krenn, "How to erase surface plasmon fringes," Appl. Phys. Lett. **89**, 091117 (2006).
29. A. Drezet, A. Hohenau, D. Koller, A. Stepanov, H. Ditlbacher, B. Steinberger, F. Aussenegg, A. Leitner, and J. Krenn, "Leakage radiation microscopy of surface plasmon polaritons," Mat. Sci. Eng. B **149**, 220 – 229 (2008).
30. J. Wang, C. Zhao, and J. Zhang, "Does the leakage radiation profile mirror the intensity profile of surface plasmon polaritons?" Opt. Lett. **35**, 1944–1946 (2010).
31. L. Li, T. Li, S. Wang, S. Zhu, and X. Zhang, "Broad band focusing and demultiplexing of in-plane propagating surface plasmons," Nano Lett. **11**, 4357–4361 (2011).
32. P. B. Johnson and R. W. Christy, "Optical constants of the noble metals," Phys. Rev. B **6**, 4370–4379 (1972).
33. P. Lalanne, J. P. Hugonin, and J. C. Rodier, "Approximate model for surface-plasmon generation at slit apertures," J. Opt. Soc. Am. A **23**, 1608–1615 (2006).
34. X. Y. Yang, H. T. Liu, and P. Lalanne, "Cross conversion between surface plasmon polaritons and quasicylindrical waves," Phys. Rev. Lett. **102**, 153903 (2009).
35. J. Le Perchec, A. Barbara, and P. Qumerais, "Near-, mesoscopic and far-field regimes of a subwavelength young's double-slit," New J. Phys. **13**, 083025 (2011).

1. Introduction

Using Surface Plasmon Polaritons (SPPs), confined electromagnetic waves at metal/dielectric interfaces, to transfer information, has the potential to bridge the gap between microelectronics and photonics, provided their intrinsically lossy character can be mitigated [1]. Indeed, as SPPs can transport optical signals on waveguides of truly nanoscale dimensions [2], they would allow for the use of the bandwidth and speed provided by optical systems, but on nanometric scales so far accessible only to semiconductor electronics [3]. In a context of information transfer and processing, it is important to design means to convert optical signals into SPPs to link long distance transfers, using standard low loss photonic devices, with miniaturised functions that

#159589 - $15.00 USD Received 9 Dec 2011; revised 5 Jan 2012; accepted 9 Jan 2012; published 13 Feb 2012
(C) 2012 OSA

would benefit from the use of SPPs. Such a converter should be compact and able to excite SPPs in a specific direction, towards the region of information processing.

SPPs have an in-plane momentum k_{SPP} larger than the momentum of free space propagating light, which means that converting light into SPPs requires the use of methods providing extra in-plane momentum to the photons. Many methods have been used to achieve this goal, but the ones relevant for nanoscale integration all use corrugations in the metal film sustaining the SPPs. Periodic arrangements of holes for instance allow for the excitation of SPPs and directionality of the excitation can be achieved when the pump beam impinges on the grating at oblique incidence [4–6]. Preferential SPP launch can be obtained under illumination at normal incidence of a grating provided the symmetry of the grating is broken [7–9]. A very efficient asymmetric grating coupler using concepts similar to the Yagi Uda antenna has been demonstrated recently [10]. Unfortunately, efficient gratings have a footprint of many wavelengths on the metal film: more compact approaches are desirable.

Schemes based on the use of one or two slits in the metal film are much more compact. A variety of such schemes have been proposed and studied theoretically [11, 12]. When a single slit is used to excite SPPs, the excitation efficiency depends on the width of the slit compared to the SPP wavelength [11–13], and directionality of the SPP excitation is possible for excitations at oblique incidence [14]. Similarly to the gratings, breaking the symmetry of a single slit can lead to a directional coupling of SPPs at normal incidence [15,16]. Furthermore, adding a Bragg reflector next to the slit allows for a directional coupling at normal illumination, but of course has the same drawback as for a grating: the footprint of the whole system represents many wavelengths [17]. Systems using two parallel nanoslits have been discussed as well and lead to directionality of SPP excitation at oblique incidence [18]. Filling each slit with dielectrics of different refractive index is expected to allow for directionality with excitation at normal incidence, although this has not been demonstrated experimentally so far [19, 20]. More schemes for directional coupling under normal incidence have been discussed theoretically [21–23].

To date, there is a lack of experimental demonstrations of all the schemes proposed. One report has shown that the SPP excitation efficiency of a single nanoslit depends on its width [24]. Another one demonstrated directional launch of SPP for one slit with illumination at 75° [25]. Both of these studies are performed using Scanning Near-field Optical Microscopy (SNOM), which is expensive, complex to implement, and SNOM images are long to acquire. The role of SPPs in the optical transmission of a pair of slits has been observed in the far-field, for slits separated by many wavelengths [26]. Eventually, the directional coupling of SPP under oblique incidence *via* a pair of nanoslits has been observed using gratings to out-couple the SPPs generated at the nanoslits – which allows for observations in a narrow wavelength range only [18].

In this article, we use leakage radiation microscopy (LRM) [27–31] to study comprehensively how light is coupled to SPPs *via* the use of arrangements of slits. LRM is extremely flexible and allows for a fast exploration of the full parameter space of the problem. In contrast to SNOM, it is cheap to implement, simple to operate and measurements are fast. Moreover, no out-coupling gratings are required to observe the SPPs: thanks to this LRM allows for the use of any wavelength without modification of the setup or sample. We show that single and double slits under oblique illumination allow for directional coupling of SPP, probing for the first time the whole parameter space of interest: angles up to 20°, slit widths/distances in the range 150 to 950 nm ($\lambda_0/4$ to $1.5\lambda_0$, with $\lambda_0 = 633$ nm). The experimental findings are well described by a simple model accounting for the diffraction of the incoming beam by the slits. Eventually, our approach allows for a direct comparison between the performances of single and double slit-based devices.

#159589 - $15.00 USD Received 9 Dec 2011; revised 5 Jan 2012; accepted 9 Jan 2012; published 13 Feb 2012
(C) 2012 OSA

2. Leakage radiation microscopy

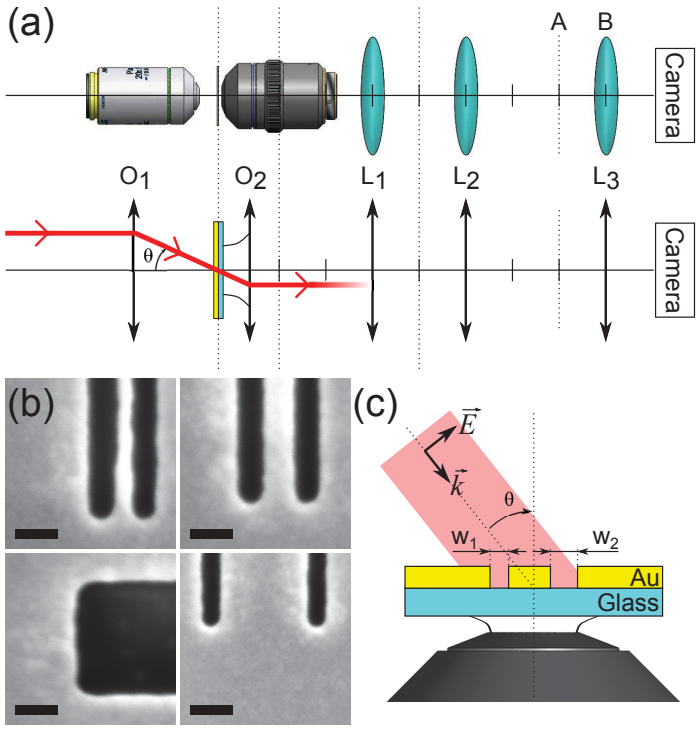


Fig. 1. Experimental configuration. (a) artistic and sketched views of the leakage radiation system. (b) SEM images of slit pairs and single slit etched in the gold film. The scale bars represent 200 nm. (c) SPPs are launched on the film by focusing an HeNe laser on the slits at an angle θ from the normal to the sample, from the gold side. The light is polarised perpendicularly to the slits. Leakage radiation is collected on the sample side by an oil immersion objective.

To conduct our studies, we use the fact that on a thin metal film (a few tens of nanometer thick) deposited on a glass substrate, the SPPs bound to the metal/air interface "leak" on the glass side [29], i.e. they are coupled back to a propagating light field on the glass side. This emission occurs at an angle larger than the total internal reflection angle of a glass/air interface. Therefore, collecting the leakage radiation requires the use of an oil immersion objective. Figure 1(a) presents the schematic of the leakage radiation microscope. Its design is similar to the one described in Ref. [28]. The beam from a polarised HeNe laser is focused on the sample by a 20×, NA 0.4 microscope objective (O_1). A polariser and half waveplate are inserted in the beam path before the objective, to align the polarisation of the beam perpendicularly to the slits (cf. Fig 1(c)). The width of the beam is much smaller than the pupil of the objective. This allows to change the angle of incidence of the beam onto the sample by translating the laser perpendicularly to the optical axis, keeping it parallel to it, as shown on Fig. 1(a) and 1(c). The spot size at the sample level is about 10 μm in diameter. The light then goes through a 100×, NA 1.49, oil immersion microscope objective (O_2), which allows for the collection of light leaking from the SPPs excited at the gold/air interface. The lens L_1 projects the back focal plane of O_2 (which is contained inside O_2) onto the lens L_2. Placing masks in front of L_2 could allow for a physical filtering in the Fourier space of the image from the sample's surface (we do not use this in the present study). The lens L_3 then images on a CCD camera either the surface of the sample, in position A, or the back focal plane of O_2, in position B.

#159589 - $15.00 USD Received 9 Dec 2011; revised 5 Jan 2012; accepted 9 Jan 2012; published 13 Feb 2012
(C) 2012 OSA

The samples are produced by thermal evaporation of a 3 nm thick germanium layer on Corning glass coverslips, followed by the evaporation of a 36 nm gold layer. The germanium serves as sticking layer for the gold, and its influence on the optical properties of the system are negligible. Slits of 20 μm length are then produced by Focused Ion Beam milling (Helios Nanolab 50 DualBeam). Figure 1(b) presents SEM micrographs of some of the slits used in this article.

The measurements of the SPP intensity are done in Fourier space, projected on the detector

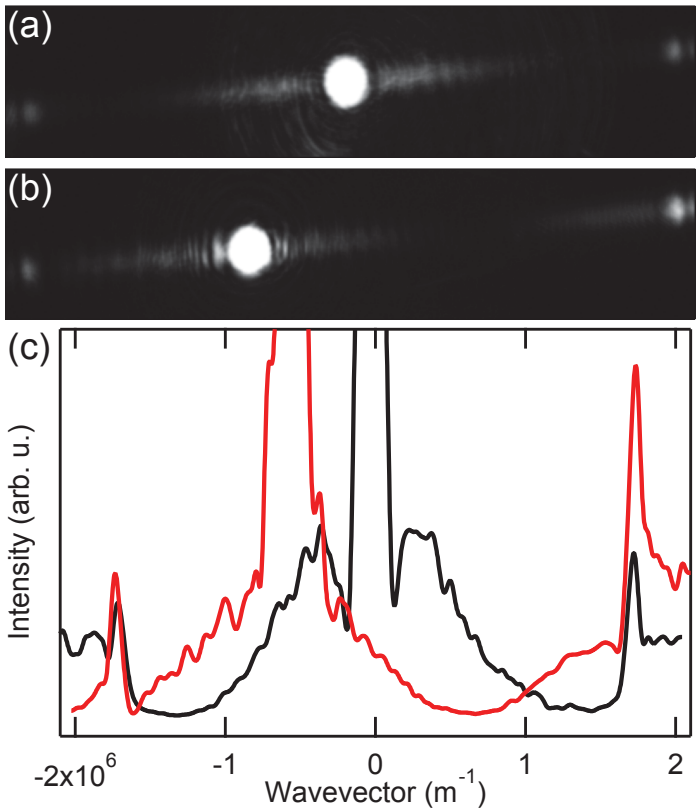


Fig. 2. Observations in the Fourier plane. (a) (resp. (b)) image of the Fourier plane when the laser is focused on a slit pair separated by 350 nm, at quasi-normal incidence (resp. at an angle $\theta = -18°$). Both images have been obtained under the same conditions. (c) Profiles taken along the images (a) black line, and (b) red line. The peaks at $\pm 1.66.10^6 \mathrm{m}^{-1}$ correspond to the SPPs. No preferential direction of coupling is observed at normal incidence, whereas at 18° mainly right-propagating SPPs are excited. Further analysis of this picture can be found in section 5.

by an appropriate arrangement of the lenses in the leakage microscope. Figure 2 presents a typical measurement in the Fourier plane: in the example presented, the laser is focused on a slit pair separated by 350 nm. In the Fourier plane, one can observe three elements: a disc of intense light, where the detector is saturated, a broad bright line, and two spots of light symmetrically positioned compared to the center of the image (Fig. 2(a) and 2(b)). The saturated spot corresponds to the pump light directly transmitted through the sample, which is partly transparent. The position of the spot indicates the angle of incidence. The broad line is the light diffracted by the slit. Its alignment is perpendicular to the slits. The twin spots placed symmetrically from the center of the image are due to the light leaking from the SPPs. The intensity of the left- and right-propagating plasmons are measured thanks to profiles taken along the Fourier images, as shown in Fig. 2(c).

#159589 - $15.00 USD Received 9 Dec 2011; revised 5 Jan 2012; accepted 9 Jan 2012; published 13 Feb 2012
(C) 2012 OSA

3. Theoretical model

The experimental results are compared to a simple analytical model to describe the efficiency of coupling of the incident light into SPPs. The underlying principle is that the pump light is diffracted by the slits, and the angular spectrum of the diffracted light can be calculated by a Fourier Transform of the field at the slit's position. We assume that the intensity of the SPPs excited is proportional to the intensity of the component of this angular spectrum matching the SPPs' wavevector [13, 14].

The slits are represented by the rectangular function $\mathrm{rect}(\frac{x-x_0}{w})$, with x_0 the position of the center of the slit considered and w its width. By definition:

$$\mathrm{rect}(\frac{x-x_0}{w}) = \begin{cases} 1 & \text{for } x_0 - \frac{w}{2} < x < x_0 + \frac{w}{2} \\ 0 & \text{for } x < x_0 - \frac{w}{2} \text{ or } x > x_0 + \frac{w}{2}. \end{cases} \quad (1)$$

The pump beam is a plane wave of wavelength λ_0 impinging on the sample at an angle θ. The field is polarized perpendicular to the slits, as illustrated on Fig. 1(c). The component of the electric field along the samples' surface at the surface of the glass substrate in the absence of the slits is $E(x) = \exp(i2\pi x\frac{sin\theta}{\lambda_0})$. When the slits are considered, we make the approximation, derived from the scalar diffraction theory of Fourier optics, that the metal film prevents the radiation from reaching the substrate, whereas it is not perturbed at the position of the slits. Once this assumption is made, at the sample surface and in the presence of the slits the component of the field along the sample surface becomes:

$$E(x) = e^{i2\pi x\frac{sin\theta}{\lambda_0}} \times \left\{ \mathrm{rect}(\frac{x-x_1}{w_1}) + \mathrm{rect}(\frac{x-x_2}{w_2}) \right\}, \quad (2)$$

with x_1 and x_2 the positions of slit 1 and 2, w_1 and w_2 their widths, as depicted in Fig. 1(c). In the following, to simplify the expression we will take x_1=0.

The angular spectrum of $E(x)$ at the slits position is obtained *via* a Fourier transform of the field $\tilde{E}(\alpha)$, where α is the coordinate of the angular spectrum corresponding to the x coordinate in real space. Using the properties of scaling, shifting in space and frequency domain of the Fourier transforms, it can be shown that:

$$\tilde{E}(\alpha) = \Pi(\alpha, w_1) + e^{-i2\pi x_2(\alpha - \frac{sin\theta}{\lambda_0})}\Pi(\alpha, w_2), \quad (3)$$

with $\Pi(\alpha, w_i) = w_1 sinc\left[w_1 \cdot (\alpha - \frac{sin\theta}{\lambda_0})\right]$. The intensity of the Fourier transform $\left|\tilde{E}(\alpha)\right|^2 = \tilde{E}(\alpha)\cdot\overline{\tilde{E}(\alpha)}$ is:

$$\left|\tilde{E}(\alpha)\right|^2 = \Pi(\alpha, w_1)^2 + \Pi(\alpha, w_2)^2 + \Pi(\alpha, w_1)\Pi(\alpha, w_2)\cdot 2cos\left[2\pi x_2(\alpha - \frac{sin\theta}{\lambda_0})\right]. \quad (4)$$

To estimate the SPP generation efficiency, we then calculate the intensity of the angular spectrum for $\alpha = \alpha_{\mathrm{SPP}}$, where α_{SPP} is derived from the dispersion relation of the leaky SPPs mode in our system. This dispersion relation is derived as described in Ref. [29], and the values of the dielectric function for gold $\varepsilon_{\mathrm{Au}}(\lambda)$ are taken from Ref. [32]. With a thickness of gold of 36 nm, λ_0=633 nm and ($\varepsilon_{\mathrm{Au}}(633\ \mathrm{nm}) = -11.43 + 1.19\mathrm{i}$), we find an effective index of $\mathrm{n_{SPP}} = 1.048$. Right-propagating SPPs and left-propagating SPPs are given by $I_{\mathrm{right}} = \left|\tilde{E}(\alpha_{\mathrm{SPP}})\right|^2$ and $I_{\mathrm{left}} = \left|\tilde{E}(-\alpha_{\mathrm{SPP}})\right|^2$, respectively.

From this expression, we can derive the maximum coupling efficiency for single slit width

#159589 - $15.00 USD Received 9 Dec 2011; revised 5 Jan 2012; accepted 9 Jan 2012; published 13 Feb 2012
(C) 2012 OSA

$w = w_{\mathrm{Max}}$. They happen to correspond to the conditions for distance between slits giving the weakest coupling in a double slit system, $x_2 = d_{\mathrm{Min}}$:

$$w_{\mathrm{Max}} = d_{\mathrm{Min}} = \frac{2m+1}{2(\alpha - \frac{sin\theta}{\lambda_0})}, \tag{5}$$

with m an integer. Similarly, on can derive the width for minimal coupling for individual slits w_{Min} and distance for optimal coupling in slit pairs d_{Max}

$$w_{\mathrm{Min}} = d_{\mathrm{Max}} = \frac{n}{(\alpha - \frac{sin\theta}{\lambda_0})}, \tag{6}$$

with n an integer. Further in the text, the extremal coupling conditions towards one direction will be indicated with the direction in superscript. For instance, the widths giving maximal coupling towards left-propagating SPPs in single slits will be denoted by $w_{\mathrm{Max}}^{\mathrm{Left}}$.

The directionality D of the SPP generation is then defined as:

$$D = \frac{I_{\mathrm{left}}}{I_{\mathrm{left}} + I_{\mathrm{right}}}. \tag{7}$$

The value of D reflects the proportion, from the total energy coupled into SPPs, of energy coupled into left propagating SPPs. Hence, it does not reflect the coupling efficiency. A value of 1 (resp. 0) indicates that only left-propagating (resp. right-propagating) SPPs are excited, and 0.5 corresponds to a symmetric excitation. The plots presented further use Eq. (4) and (7) to calculate the SPP generation efficiency and directionality.

As will be seen further, this model gives a qualitative description of the phenomenon, and is useful to identify simply the regions of high coupling efficiency as well as high directionality. We direct the reader to Ref. [11–13, 33–35] for more in-depth descriptions of the interplay between the scattering of slits and the generation of SPPs.

4. Single slits

Let us first turn our attention to the case of a single slits used to excite SPPs. In the experiment, slits of increasing widths have been milled into the gold film, by steps of 50 nm (100 nm, 150 nm,..., 950 nm). The experimental plots are generated by making a linear extrapolation of the values between measured values. Fig. 3(a) presents the intensity measured for the left propagating SPPs, normalised to the highest intensity, alongside with the results of Eq. (4) in Fig. 3(b). The agreement between experiment and the simple model is remarkable.

The directionality of SPP generation by single slits is presented in Fig. 3(c) and 3(d). As can be seen on these figures, regions showing directionality in excess of 90% can be found: more than 90% of the generated SPPs are launched preferentially in one direction. For the case presented here, such high directionality are obtained with slits of widths between 450 and 550 nm, and angles close to 20°.

Optimal directionality/excitation efficiency of SPP occur at the intersection of the curves of maximum coupling efficiency into one direction w_{Max} and the curves of minimum coupling efficiency into the other direction w_{Min} obtained thanks to Eq. (5) and (6). In Fig. 3(b) and 3(d), we highlight $w_{\mathrm{Max}}^{\mathrm{Left}}$ in solid black lines and the $w_{\mathrm{Min}}^{\mathrm{Right}}$ in solid green lines. From these considerations, it appears that there is a general trade-off to be found between angle of incidence and width of slits for optimal operation. To operate at small angles, one has to use wide slits (for instance in this case: operation for 10° is optimal for a slit width of 750 nm). Conversely, the optimal point with narrowest slit (455 nm width here) occurs at an angle of operation of -20.7°. A more complete picture of $w_{\mathrm{Max}}^{\mathrm{Left}}$ and $w_{\mathrm{Min}}^{\mathrm{Right}}$ can be found in Fig. 5(a).

#159589 - $15.00 USD Received 9 Dec 2011; revised 5 Jan 2012; accepted 9 Jan 2012; published 13 Feb 2012
(C) 2012 OSA

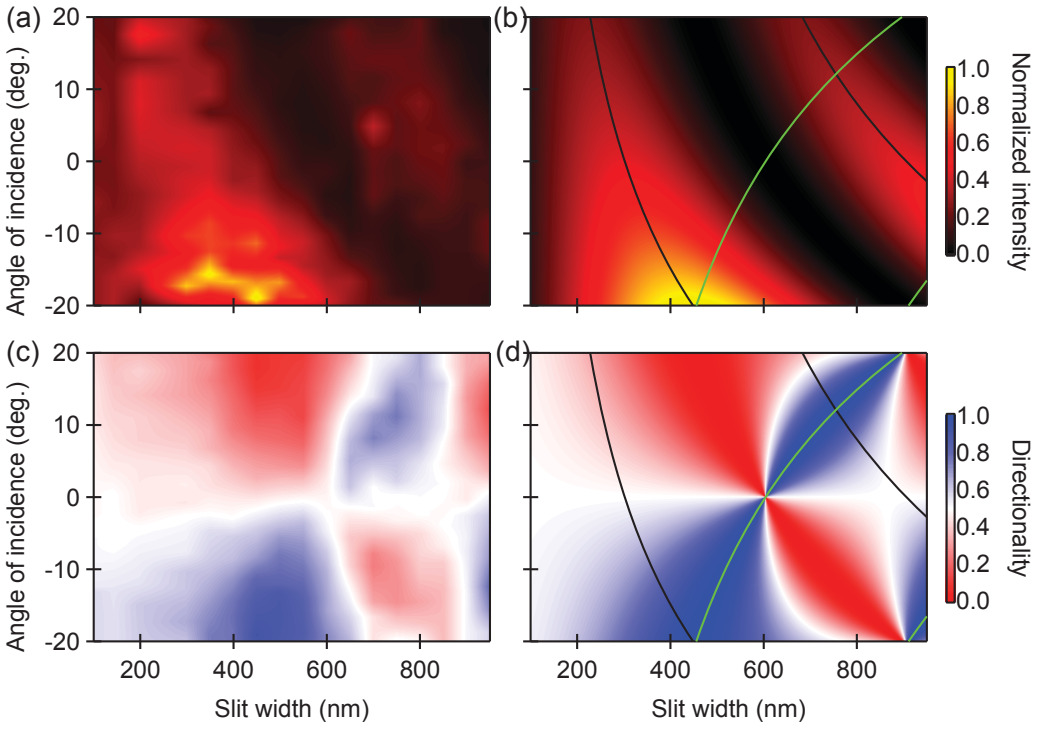


Fig. 3. Single slits, at $\lambda_0 = 633$ nm. (a) Experimental coupling efficiency into left propagating SPPs. (b) Theoretical results obtained from Eq. (4). Both intensity plots are normalized to their maximum intensity. (c) Measured directionality. (d) directionality calculated with the model explained in the text. Directionality=1 means that only left propagating SPPs are excited, 0: only right propagating, and 0.5 means equal excitation in both directions. The experimental plots are obtained by making a linear extrapolation between the points actually measured. In the theoretical plots (b) and (d), the black and green lines indicate $w_{\mathrm{Max}}^{\mathrm{Left}}$ and $w_{\mathrm{Min}}^{\mathrm{Right}}$, respectively.

5. Double slits

We now consider the case of parallel sub-wavelength slit pairs. The slits milled by FIB are 90 nm wide, and the distance between slits is varied between 150 nm and 700 nm by steps of 50 nm. Again here the experimental plots are generated by using a linear extrapolation between the values actually measured. Figure 4 presents the excitation efficiency of left propagating SPPs, as well as directionality, depending on slit distance and angle of incidence. Similarly to Fig. 3, the agreement between experiment and model is good, although the measurements here are slightly more noisy. The slits milled here have a width approaching the resolution limit of the fabrication method employed, which could explain the increased noise compared to the single slits. Indeed the quality of the milling varies more from one slit to the next when we operate close to the limits of the instrument, which can lead to variations in the optical transmission of the slits, and thus variations along the horizontal axis in Fig. 4(a). The directionality is not affected by this as it is a ratio of intensities, thus insensitive to variations in absolute coupling to SPPs. Indeed, Fig. 4(c) does not show the sharp variations visible in Fig. 4(a). The directionality depends little on the slit width (data not shown, but can be calculated using Eq. (4) and (7)), which means that the key parameter is the distance between the slits.

The specific situation shown in Fig. 2(c) (slit distance 350 nm, $\theta = -18^\circ$ and 0°) can be

#159589 - $15.00 USD Received 9 Dec 2011; revised 5 Jan 2012; accepted 9 Jan 2012; published 13 Feb 2012
(C) 2012 OSA

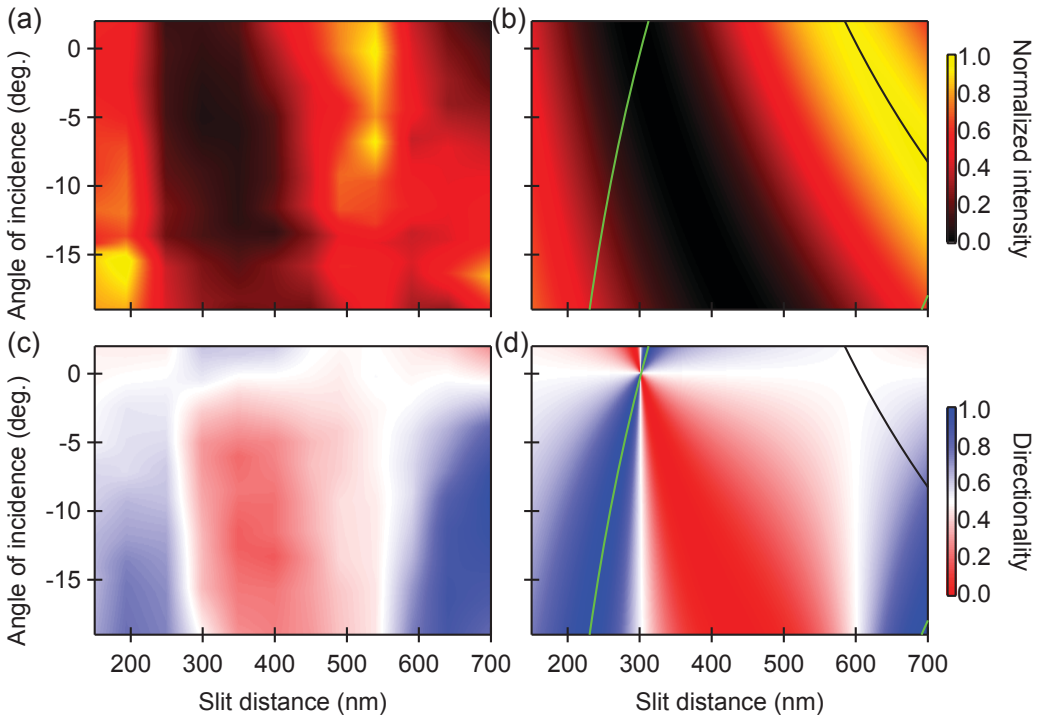


Fig. 4. Double slits – for $\lambda_0 = 633$ nm. (a) Experimental measurement of coupling efficiency into left-propagating SPPs. (b) Theoretical results obtained from Eq. (4). (c) Experimental directionality. (d) Theoretical results obtained from Eq. (7) for the directionality. In (b) and (d), the black and green lines indicate $d_{\mathrm{Max}}^{\mathrm{Left}}$ and $d_{\mathrm{Min}}^{\mathrm{Right}}$, respectively.

analyzed further in light of these considerations. The large directionality observed exists due to the fact that the coupling efficiency towards the left direction changes little between $\theta = -18^\circ$ and 0° (from 0.08 to 0.06 normalized units, Fig. 4(b)), whereas the coupling efficiency to right propagating SPP increases from 0.06 to 0.44.

To better compare the performances of single and double slits, we now introduce a Figure Of Merit (FOM). We define the FOM for left propagating SPPs as the product of the directionality D, rescaled between -1 and 1, and the left-propagating SPP intensity I_{left} (from the theoretical model). In this definition a majority of right-propagating SPPs are represented by a negative FOM:

$$\mathrm{FOM} = (2D - 1) \cdot I_{\mathrm{left}}. \tag{8}$$

With this definition, the FOM are large when the coupling efficiency *and* the directionality is large. Optimal performances for directional coupling of SPPs are obtained for the highest FOMs.

The base 10 logarithm of the FOM is plotted on Fig. 5. The purple regions represent regions where right-propagating SPPs are preferentially excited, or extremely inefficient coupling to a majority of left propagating SPPs. Figure 5 highlights the fact that high directionality combined with high SPP excitation occurs on different regions for single and double slits. These plots can be used to determine what system is best to achieve a specific goal. For instance, one can be interested to have a directional coupler with the smallest footprint possible. The footprint of a slit pair is the distance between slits, plus the width of one individual slit (in the case

#159589 - $15.00 USD Received 9 Dec 2011; revised 5 Jan 2012; accepted 9 Jan 2012; published 13 Feb 2012
(C) 2012 OSA

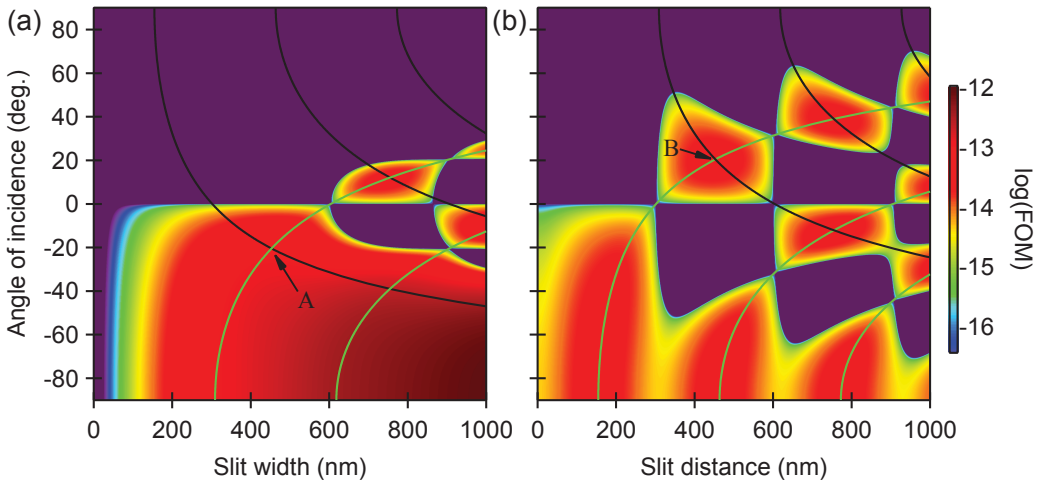


Fig. 5. Comparison of figures of merit (FOM) for single (a) and double slits (b). The log of the FOM is plotted (see text for the definition of the FOM). Here, $\lambda_0 = 633$ nm, $n_{SPP} = 1.048$, and the FOM is calculated for left propagating SPPs. The purple regions correspond to $D \leq 0.5$, i.e. a majority of right-propagating SPPs. In (a), the black and green lines indicate w_{Max}^{Left} and w_{Min}^{Right} respectively. In (b) they indicate d_{Max}^{Left} and d_{Min}^{Right}.

presented here, 90 nm). With these considerations, the point of optimal coupling for smallest device occurs for a footprint of ≈ 455 nm for single slits, and ≈ 545 nm for double slits (cf. Fig. 5, points A and B) – a single slit will always provide smaller footprint. Moreover, if one can sacrifice some coupling efficiency, single slits allow to work at smaller angles, as shown by the region lying between point A and the line $\theta = 0$.

6. Conclusions

In this study, we directly compare the directionality of SPP launch by single and double slits on a thin metal film. The measurements, using leakage radiation microscopy, allow for a rapid probing of the parameter space of this problem: slit width, distance, and angle of incidence of the pump beam. Moreover, the wavelength of illumination can be changed without modifications to the sample. The experimental findings are well described by a model using the angular spectrum of the light diffracted by the slits to estimate the SPP generation efficiency. Single as well as double slits allow for directional SPP excitation provided that the illumination is at oblique incidence. There is a general trade-off between size of the devices and the angle of incidence required for optimal coupling. Overall, single slits allow for better performances than double slits and have a smaller footprint. The approach developed here should allow for extensive studies of most of the other schemes proposed for unidirectional SPP coupling, and performs better than the ones used in all previous reports.

Acknowledgments

The authors gratefully acknowledge fruitful advices from Aurélien Drezet while building the leakage radiation microscope, and Markus Schmidt for the calculation of the effective index of the SPPs in our system. S.A.M. and Y.S. acknowledge support by the UK Engineering and Physical Sciences Research Council. Y.S., G.D. and D.Y.L. acknowledge funding from the Leverhulme Trust.

#159589 - $15.00 USD Received 9 Dec 2011; revised 5 Jan 2012; accepted 9 Jan 2012; published 13 Feb 2012
(C) 2012 OSA

NANO LETTERS

Letter

pubs.acs.org/NanoLett

Unidirectional Side Scattering of Light by a Single-Element Nanoantenna

Dries Vercruysse,*[,†,‡] Yannick Sonnefraud,[§] Niels Verellen,*[,‡,†] Fabian B. Fuchs,[§] Giuliana Di Martino,[§] Liesbet Lagae,[†,‡] Victor V. Moshchalkov,[‡] Stefan A. Maier,[§] and Pol Van Dorpe[†,‡]

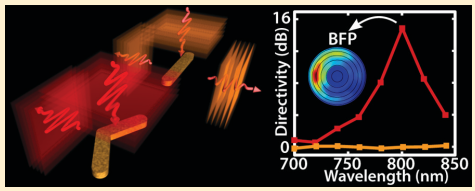
[†]IMEC, Kapeldreef 75, B-3001 Leuven, Belgium

[‡]INPAC and Department of Physics, KU Leuven, Celestijnenlaan 200 D, B-3001 Leuven, Belgium

[§]Experimental Solid State Group, Physics Department, Imperial College London, London SW7 2AZ, United Kingdom

S *Supporting Information*

ABSTRACT: Unidirectional side scattering of light by a single-element plasmonic nanoantenna is demonstrated using full-field simulations and back focal plane measurements. We show that the phase and amplitude matching that occurs at the Fano interference between two localized surface plasmon modes in a V-shaped nanoparticle lies at the origin of this effect. A detailed analysis of the V-antenna modeled as a system of two coherent point-dipole sources elucidates the mechanisms that give rise to a tunable experimental directivity as large as 15 dB. The understanding of Fano-based directional scattering opens a way to develop new directional optical antennas for subwavelength color routing and self-referenced directional sensing. In addition, the directionality of these nanoantennas can increase the detection efficiency of fluorescence and surface enhanced Raman scattering.



KEYWORDS: *Nanoantenna, surface plasmon resonance, directionality, Fano resonance, side scattering*

The interaction of light with metal nanoparticles is largely governed by resonant oscillations of the free electrons at the metal-dielectric interface. These so-called localized surface plasmon resonances (LSPR) can reach frequencies in the visible spectrum, have large extinction cross sections, are very sensitive to the surrounding medium, and lead to deep-subwavelength electromagnetic field confinement and enhancement. Plasmonic resonators, therefore, bring optics into the nanoscale and have already found applications in disease diagnostics and treatment, photovoltaics, and optical communications.[1−7]

One of the most determinative characteristics of a plasmonic resonator is its shape. It is well-known that the shape determines—to a large extent—the LSPR spectral positions.[8] Specific resonator designs, consisting of a single or multiple particles, also allow to control the LSPR quality-factor by scattering loss engineering based on plasmon hybridization,[9] sub- and superradiance, and Fano interference.[10−13] Additionally, similar to classical antennas, a proper plasmonic antenna design will impact its directionality—that is, the ability to direct scattered radiation in a particular direction. Achieving high directivities in combination with a high degree of flexibility for the direction is elementary to devise efficient subwavelength plasmonic transmitters, receivers, and sensors.

To obtain directional scattering, constructive and destructive interferences of multiple coherent radiation sources with carefully designed spatial separation and phase differences are required. Directional scattering of a plane wave *along* its propagation direction has recently been observed in core−shell nanoparticles,[14] as well as in nonmetallic silicon nanospheres.[15] The obtained large forward-to-backward scattering ratios were shown to result from interfering dipoles and quadrupoles where retardation of the incident light over the particle volume activates the higher order mode and induces the required phase differences.[16] Higher order modes in a tilted plasmonic nanocup can also rotate the scattering distribution away from the incident light direction.[17−19] To favor unidirectionality *perpendicular* to the incident plane wave direction—that is, side scattering—the antenna's mirror symmetry has to be broken relative to the light polarization. This is possible for particle assemblies. A well-known example is the plasmonic Yagi-Uda antenna.[20−23] A more compact alternative consisting of a bimetallic nanodisk dimer was recently shown to route different colors either left or right from the incident light direction as a result of material-induced phase shifts between the two disks' dipole modes.[24,25] Directional scattering under localized excitation of a plasmonic resonator, using, for example, fluorescent molecules or quantum dots, relaxes the structural requirements as the retardation of the excitation field over the particle volume introduces additional phase shifts and dipole-activation of dark modes.[20,26−29]

Received: May 22, 2013
Revised: July 12, 2013
Published: July 25, 2013

 © 2013 American Chemical Society dx.doi.org/10.1021/nl401877w | *Nano Lett.* 2013, 13, 3843−3849

In this Letter, we demonstrate strongly unidirectional side scattering of a plane wave by an individual V-shaped metal nanoparticle, as illustrated in Figure 1a. This simple planar

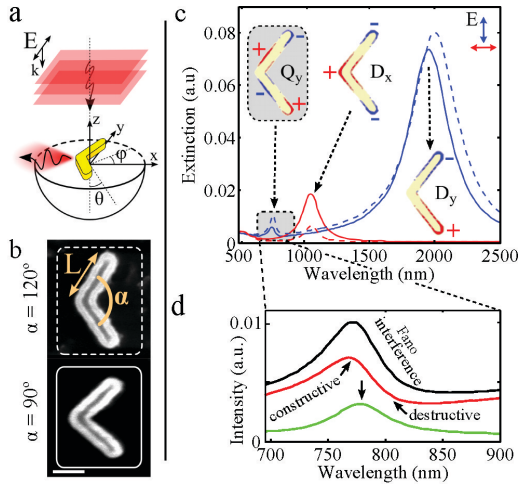


Figure 1. (a) Unidirectional side scattering of a plane wave with a plasmonic V-antenna. (b) SEM images of V-antennas with arm length L = 250 nm and opening angle α = 120° and 90°. Scale bar: 100 nm. (c) Simulated extinction spectra for the antennas in panel b (dashed curves: α = 120°, solid curves: α = 90°) for x- and y-polarization (red and blue, respectively). The insets show the charge density distributions of the observed V-antenna LSPR modes: Q_y, D_x, and D_y. (d) A zoom-in on the Q_y mode (α = 120°) in panel c reveals Fano interference when comparing the extinction (black), scattering (red), and absorption (green) intensity.

single-element antenna geometry has been used before as a tunable-phase antenna building block in birefringent metasurfaces and aberration-free ultrathin flat lenses at telecom frequencies.[30,31] While these applications rely on diffractive far-field interferences generated by carefully designed arrays, here, the broken mirror symmetry of a single V-antenna allows us to benefit directly from the characteristic phase shifts of an intrinsic Fano interference, arising from the coherent near-field coupling of a dipole and higher order LSPR mode—even at near-infrared and visible frequencies. We use finite difference time domain (FDTD) calculations to analyze the antenna modes and map the three-dimensional far-field scattering intensity distributions. These results are then compared with, and confirmed by, experimental extinction spectroscopy and angular resolved scattering distributions obtained with back focal plane (BFP) imaging.[20,24,32] The tunability of the V-antenna's directivity and scattering efficiency is further investigated using different V-shapes. Although being intimately related to the interference of coupled dipole and quadrupolar mode components, we will illustrate how a simple, intuitive two point-dipole model is capable of conveying the main aspects of the V-antenna's directional behavior.

Scanning electron beam microscopy (SEM) images of two V-antennas studied in this work are shown in Figure 1b. The arm length, L, and opening angle (V-angle) of the arms, α, define the antenna geometry. The nanostructures consist of sputtered gold with a thickness of 50 nm (= antenna thickness) and are supported by a glass substrate coated with 10 nm indium tin oxide (ITO) which facilitates SEM analysis. They were fabricated using electron beam lithography with negative-tone hydrogen silsesquioxane (HSQ) resist, subsequent Xe ion milling, and a sulfur hexafluoride + oxygen dry etch (Oxford instruments Plasmalab System 100 ICP 180).[33] This last step is applied to remove the remaining resist on top of the particles. The antennas are arranged in 50 × 50 μm^2 square arrays with a pitch of either 1.5 μm for extinction spectroscopy or 4.5 μm for BFP measurements.

Extinction (1 - Transmission) spectra are taken with a Fourier transform infrared (FTIR) microscope (Bruker vertex 80v + Hyperion) using two 15× magnification Cassegrain condensers. The scattering directions of the antennas are measured using back focal plane (BFP) imaging.[20,32] Monochromatic light, selected from a Fianium supercontinuum laser source using a prism system, is delivered to the BFP setup with an optical fiber and focused on the sample by a low NA objective, after passing through a polarizer. The resulting incident beam has a narrow angular distribution (i.e., nearly parallel beam) and creates an illumination spot of ±10 μm diameter on the sample. The light scattered and directly transmitted into the glass substrate is collected with a 100× magnification oil immersion objective with an NA of 1.49. The BFP, which contains the angular scatter information, forms inside the objective and is projected on an opaque disk that blocks the bright central spot corresponding to the unscattered light. This filtered image is then projected on a CCD camera. For more details and a schematic drawing of the setup, see Supporting Information.

A commercial FDTD solver[34] is used to calculate extinction, scattering, and absorption spectra, LSPR charge density distributions, and far-field scattering distributions. The latter are either obtained with the built-in far field projection calculator of the solver for antennas in a homogeneous medium (i.e., no substrate) or calculated from the electric field intensities on a 3 μm box surrounding the particle when the substrate is included (see Supporting Information for more details). The charge plots are obtained from evaluating the Poisson equation using the complex fields extracted from the simulations. The mesh size used in the simulations is 2 nm. The dielectric permittivity of gold is based on Johnson and Christy data,[35] and the refractive index of the substrate is n = 1.52. The 10 nm ITO layer was not included in the simulations.

The scattering behavior of a nanoantenna is determined by its LSPR modes. For the V-antennas in Figure 1b, three strong resonant modes are observed in the simulated extinction spectra (Figure 1c). Corresponding modal charge distributions in the insets reveal these as: a dipole mode, D_x, for x-polarized illumination (red curves), and for y-polarization (blue curves) the fundamental dipole mode, D_y, and first higher order mode, referred to as Q_y. The latter can be considered as the third order (l, m) = (3,0) nanorod LSPR mode with an additional quadrupole component (l, m) = (2, ± 1) introduced by the structural symmetry reduction. Here, l and m refer to the spherical harmonics Y_l^m in the Mie expansion of the modes.[36]

Spectral tunability of these antenna modes is most effectively achieved by varying the antenna length L and is similar as for the well-documented nanorod antennas (Figure S2a in the Supporting Information shows how the modes red-shift with increasing L).[37] As the spectra in Figure 1c show, however, changing the V-angle α from 120° (dashed curves) to 90° (solid curves) has little effect on the LSPR wavelengths (see also Figure S2b in the Supporting Information for different α).

dx.doi.org/10.1021/nl401877w | Nano Lett. 2013, 13, 3843−3849

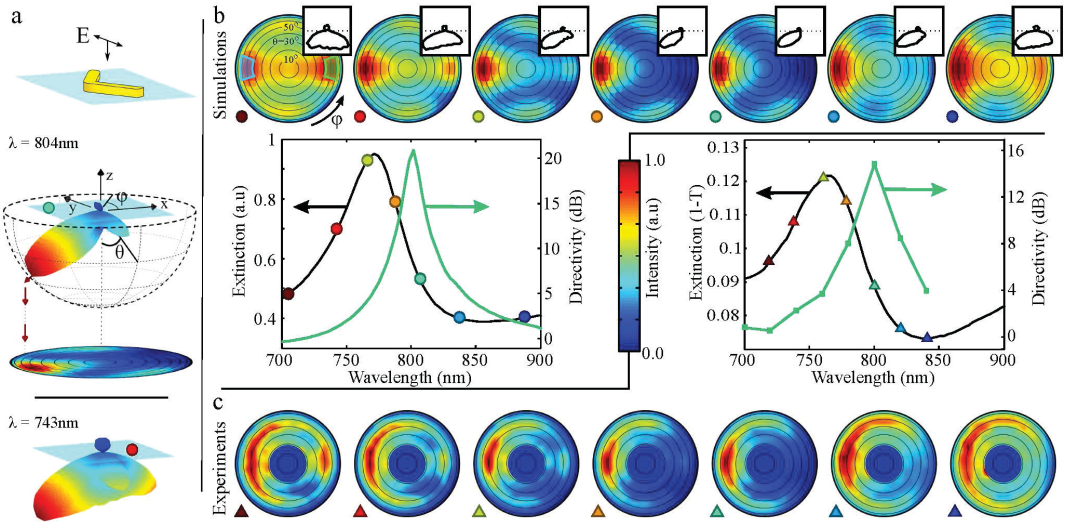


Figure 2. Scattering intensity distributions and directivity of a V-antenna on a substrate (L = 250 nm, α = 120°). (a) Simulated 3D distributions. Top: directional scattering at λ = 804 nm. Bottom: no directionality at λ = 743 nm. The light blue plane indicates the substrate interface. (b) Simulated 2D projections at several wavelengths throughout the Q_y-Fano resonance—indicated with the colored dots in the antenna's extinction spectrum (black curve). Insets show the cross-section of the 3D distribution at φ = 0 (x–z plane)—dotted line: substrate/air interface. Directivity, D, calculated from the 2D polar plots is shown together with the extinction spectrum (green curve, right axis). (c) Corresponding experimental back focal plane (BFP) measurements. Color scale indicates normalized intensity. All data presented is based on y-polarized light.

Changing α does, nevertheless, considerably influence the extinction intensities and quality factors (Q-factors). As can be seen in Figure 1c, when α decreases the extinction intensity of D_x increases, while decreasing for D_y and Q_y. This α dependence is a direct consequence of the changing effective dipole moments of the modes and their projection on the excitation field.[38] Here, a larger dipole moment leads to a stronger LSPR excitation and hence a larger extinction cross-section. In addition, the variable dipole moments also affect the radiative losses and therefore the Q-factor of the modes. The LSPR Q-factors as a function of L and α are shown in the Supporting Information, Figure S2c. We conclude that, although the V-angle α provides nearly no tunability of the LSPR spectral positions, it does affect the relative expression of the interfering y-polarized modes, and therefore, as will be discussed in Figure 3, the directionality of the antenna.

As already mentioned in the introduction, unidirectional side scattering requires an arrangement of multiple coherent radiation sources which, additionally, has broken mirror symmetry across the (E,k)-plane (Figure 1a). In the V-antenna this task can be fulfilled by the spectrally overlapping D_y mode and quadrupole $(l, m) = (2, \pm 1)$ component of the Q_y mode. As the spectral zoom-in in Figure 1d shows (α = 120°), the coherent excitation of these modes results in interference in the scattering tail (red line) of the D_y mode. On the shorter wavelength side of the Q_y absorption resonance (green curve) constructive interference leads to increased scattering intensity, while on the longer wavelength side both modes interfere destructively. This phenomenon, characterized by an asymmetric spectral line shape, is known as Fano resonance or Fano interference and mainly arises here from the Q_y mode's l = 3 component, as it is also observed for nanorods (α = 180°).[39]

The impact of this Fano interference on the angular distribution of the scattering intensity is illustrated in Figure 2. In this figure, simulated (panels a,b) and experimental (panel c) results for the L = 250 nm, α = 120° antenna in Figure 1 are provided, at several wavelengths around the Q_y-Fano resonance for y-polarized light. The strongest directionality in the simulations is reached at λ = 804 nm. The corresponding three-dimensional (3D) far-field scattering intensity distribution in panel a (with azimuthal angle φ and polar angle θ) allows us to evaluate the scattering in every direction. Strong lateral directionality is clearly observed. Since, in general, plasmonic nanoparticles scatter most of the light into the higher index substrate, indicated by the light blue plane, the *ideal* scattering pattern expected for a particle in free space is disturbed. If no substrate were present here, the maximum scattering direction would shift up to $(\varphi, \theta) = (\pi, (\pi/2))$, i.e., in the direction of the tip of the V-antenna (negative x-direction). This means that we obtain directionality which is perfectly perpendicular to the incident light. A scattering plot near a quadrupolar resonance typically comprises four lobes. For the Q_y mode of the V-antenna, this is most clearly seen in the 3D scattering plot at λ = 743 nm (Figure 2a, bottom): two lobes in x-, and two in y-direction. However, radiation in the y-direction $(\varphi = \pm (\pi/2))$ is much weaker and not unidirectional because the antenna geometry, and hence the mode, has y = 0 as symmetry plane.

To facilitate comparison with the experimental BFP images, the 3D-plots are transformed into 2D projections, as shown in Figure 2a. The color scale indicates the normalized scattering intensity. The finite NA = 1.49 of the collection objective and the refractive index of the glass substrate (n = 1.52) were taken into account in the calculation of these projections by including only scattering up to an angle $\theta = a \sin(1.49/1.52) = 78°$.

dx.doi.org/10.1021/nl401877w | *Nano Lett.* 2013, 13, 3843–3849

Simulated BFP projections at different wavelengths are shown in Figure 2b. The colored dots indicate their spectral position in the corresponding extinction spectrum. The insets show the scattering intensity in a cross-section at $\varphi = 0$ (x–z plane) taken from the 3D distribution. The dotted line indicates the substrate/air interface.

To quantify the directionality of the antenna, we introduce the directivity, D, as the ratio of the light intensity scattered in the negative x-direction to the intensity scattered in the positive direction:

$$D = 10\log_{10}\frac{\iint_{(\theta_m-\delta,\pi-\delta)}^{(\theta_m+\delta,\pi+\delta)} S(\varphi,\theta)\sin(\theta)\mathrm{d}\varphi\mathrm{d}\theta}{\iint_{(\theta_m-\delta,-\delta)}^{(\theta_m+\delta,+\delta)} S(\varphi,\theta)\sin(\theta)\mathrm{d}\varphi\mathrm{d}\theta}$$

with $S(\varphi,\theta)$ as the intensity in the BFP image. The considered integration intervals are indicated in Figure 2b (brown dot). $\delta = 10°$, and $(\varphi, \theta) = (\pi, \theta_m)$ corresponds to the maximum scattering intensity direction which is close to $\theta_m = 55°$ for the simulations and $\theta_m = 45°$ for the measurements. Alternative directivity calculations are provided in the Supporting Information. Directivity values derived from the polar plots in panel b are shown together with the antenna's extinction spectrum (green line, right axis).

Far away from the Q_y extinction resonance (brown and blue dots) very little directionality is observed. A nearly equal amount of light is scattered in the positive and negative x-direction. When approaching the LSPR resonance, gradually more power is scattered into the negative x-direction. The directivity reaches a maximum of more than 20 dB at $\lambda = 804$ nm, on the longer wavelength flank of the Q_y absorption resonance peak.

An excellent qualitative agreement with the experimental BFP images, and derived directivities, in Figure 2c is observed. Again, the colored triangles indicate in the experimental extinction spectrum the wavelengths at which the images where taken. Clear unidirectional side scattering is seen from 760 to 820 nm, while wavelengths on the blue side of the Q_y mode show an increasing amount of scattering in the positive x-direction. An experimental directivity of 15 dB is reached at $\lambda = 800$ nm. This value is comparable to directivities observed for bimetallic nanodisk dimers.[24] Since the antennas are fabricated in a square grid with a 4.5 μm pitch, the raw images are the combination of a square diffraction pattern with the scattering pattern of an individual antenna. Therefore, for clarity, values in between the diffraction spots were interpolated (see Supporting Information for more details).

The influence of a varying opening angle α on the total scattering cross-section of the V-antenna was already discussed in Figure 1c. Spectral shifts of the Q_y mode were found to be very small. Nevertheless, the distribution of the oscillating charges (approximate arrangement of the coherent radiation sources: Q_y and D_y) changes, and consequent changes in the directionality are expected. Indeed, as Figure 3a shows, scattering distributions of antennas with decreasing α, taken at their most directive wavelength, present important differences. For $\alpha = 180°$ the antenna is symmetric, and an equal amount of light is scattered left and right. In addition to the central scattering lobe ($\varphi = 0, \pi$), side lobes expected for the $l = 3$ nanorod LSPR mode near $\varphi = \pm(\pi/2)$ are observed.[40] Once the antenna symmetry is broken ($\alpha < 180°$), the right scattering lobe disappears. Figure 3b shows the spectral behavior of the directivity for the antennas in panel a. It is seen that each

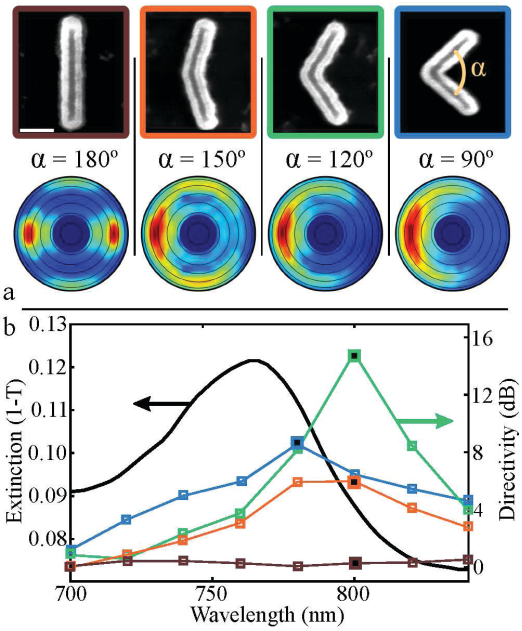


Figure 3. Directivity tunability with V-antennas of varying opening angle α ($L = 250$ nm). (a) Back focal plane (BFP) images of the antennas shown in the SEM images at their most directive wavelengths, indicated in panel b. Scale bar: 100 nm. (b) Spectral behavior of the directivity for $\alpha = 180°$ (brown), 150° (orange), 120° (green), and 90° (blue). The black curve is the experimental extinction spectrum for $\alpha = 120°$.

asymmetric antenna can scatter directionally and reaches a maximum directivity at the longer wavelength flank of the Q_y extinction resonance (black curve). The highest directivity of more than 15 dB is reached for $\alpha = 120°$. Further optimization of the antenna shape could push this value to even higher dB. As, for decreasing α, the antenna arms align with the x-axis, their individual x-oriented dipole moments, p_x, increase. This allows the antenna to radiate more power in the side lobes. Consequently, we see that for $\alpha = 90°$ scattering in the y-direction becomes again more prominent (panel a). As a result of the decreasing Q_y extinction cross-section for decreasing V-angles (Figure 1c), antennas with $\alpha < 90°$ were not measured.

The observed directionality of the V-antenna arises from the interference of two coherent radiation sources: D_y and Q_y. It is in fact possible to substitute this coupled dipole–quadrupole system with two coherent dipole sources. The advantage of this representation is that it allows us to understand and describe the antenna's directional behavior with an intuitive two-dipole model (Figure 4a).[24] The emission from two coherent point dipoles, separated by a distance d, is the sum of their individual waves. For two dipoles of equal strength, the power radiated in the two opposite directions along the axis that connects them, is proportional to $\cos[(\Delta\phi + kd)/2]$ in one direction, while proportional to $\cos[(\Delta\phi - kd)/2]$ in the other. Here, $\Delta\phi$ is the phase difference between the dipoles and the wavenumber $k = 2\pi/\lambda$. The phase difference, kd, as a result of the spatial separation adds to $\Delta\phi$ and when either $(\Delta\phi + kd)$ or $(\Delta\phi - kd)$ becomes equal to π, the sources interfere destructively in

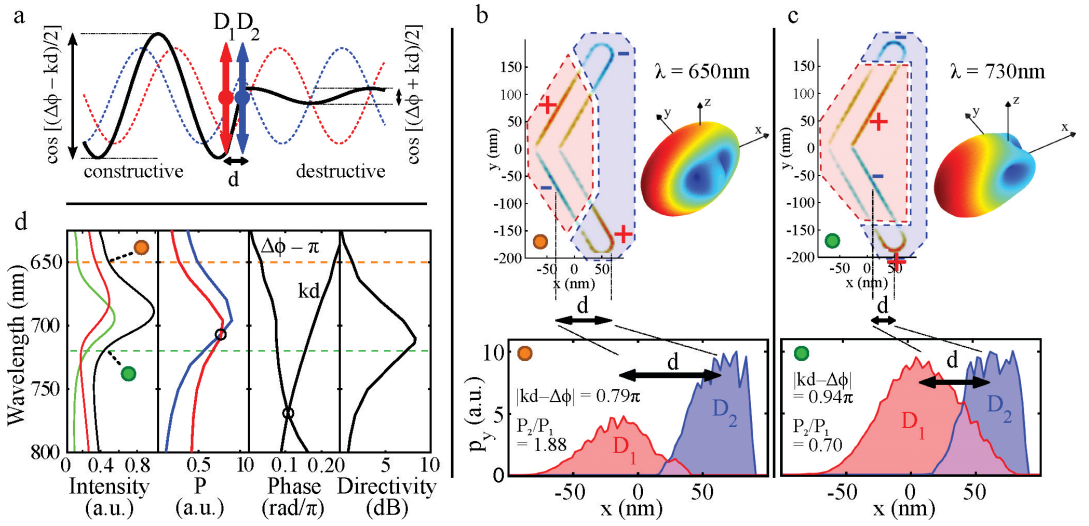


Figure 4. Two-dipole representation of the V-antenna Q_y-Fano mode. (a) Illustration of directional emission (black line) from two point-dipole sources D_1 (red) and D_2 (blue) separated by a distance d. (b) Top: Simulated charge density distribution and 3D scattering distribution of a V-antenna (L = 250 nm, α = 120°) in a homogeneous medium (n = 1) at λ = 650 nm (low directivity, orange dot). Bottom: Dipole moment p_y as a function of the position x along the antenna, calculated from the charge distribution. The dashed areas indicate the regions in which D_1 and D_2 are evaluated. d indicates the distance between the center of D_1 and D_2. (c) Same as panel b, but λ = 730 nm (strongly directional scattering, green dot). (d) Spectral dependence of, from left to right: The antenna's extinction (black), absorption (green), and scattering (red) intensity at the Q_y-Fano resonance; dipole moment strength, P, for D_1 (red line) and D_2 (blue line); phase difference $\Delta\phi - \pi$ of dipole moments P_1 and P_2, and phase shift kd introduced by distance between D_1 and D_2; directivity derived from the two-dipole model.

the corresponding direction. Simultaneously, in the opposite direction the phase difference is lowered, resulting in constructive interference. Therefore, to obtain complete suppression of radiation in one direction, first, the dipole sources must have dipole moments of equal magnitude, and second, their phase difference must match the spatial separation such that $|kd \pm \Delta\phi| = \pi$.

The two-dipoles representation of the V-antenna's Q_y-Fano mode is based on the associated charge distributions. Figure 4 shows the charge distribution in a spectral region with low directivity (panel b, orange dot) and in one with high directivity (panel c, green dot), together with the corresponding 3D scattering plots. The antenna's spectral properties are shown in the left graph of panel d. In contrast to Figure 2, here, the substrate was not included in the simulation (V-antenna in vacuum, n = 1). Consequently, the forward/backward scattering symmetry along the z-axis is restored (panels b,c). From the charge distributions two regions, D_1 and D_2, can be defined for each wavelength. These regions are indicated with the dashed areas in Figure 4b,c and represent the two dipole sources in the model. To determine the strength, phase, and position of D_1 and D_2, their respective dipole moments p_y as a function of the position x along the antenna are calculated:

$$p_y^i(x, \lambda) = \int\int_{D_i(x,\lambda)} \rho(x, y, z, \lambda) y \mathrm{d}y\mathrm{d}z$$

with ρ the complex charge density and i = 1,2 referring to the two dipoles. $p_y^i(x)$ for D_1 (red curve) and D_2 (blue curve) are shown at the bottom of panels b and c. From these curves we obtain, first of all, the positions of D_1 and D_2 as the average position weighted by $p_y^i(x)$, and consequently their separation distance d. By calculating the total dipole moment, P, given by

$$P_i(\lambda) = \int_{D_i(\lambda)} p_y^i(x, \lambda) \mathrm{d}x$$

for both dipoles, their relative strength and phase difference $\Delta\phi$ can be evaluated as well. The full spectral dependence of the dipole strength P is shown in the second graph of Figure 4d—D_1 (red curve) and D_2 (blue curve). The next graph depicts $\Delta\phi - \pi$ and kd.

On the shorter wavelength side of the Fano resonance (orange dots), the increased scattering intensity can be attributed to the dominating D_2 (P_2/P_1 = 1.88). Simultaneously, panel b shows charge accumulation on the outer edges of the antenna, resulting in a large separation with $kd = 0.24\pi$ rad. Since $\Delta\phi$ is only 1.03π rad, it cannot compensate the large spatial phase difference kd. We get at best $|kd - \Delta\phi| = 0.79\pi$ rad, and almost no directionality is obtained. On the longer wavelength side of the Fano resonance, very different behavior is observed (green dots). The destructive Fano interference translates into dipoles D_1 and D_2 with comparable moments (P_2/P_1 = 0.70), as can be seen again in panel d. Furthermore, the charges that makes up D_1 and D_2 are now located near the center of the antenna, giving rise to a small separation ($kd = 0.14\pi$ rad). Additionally, $\Delta\phi$ rises gradually with the wavelength, up to $\Delta\phi = 1.08\pi$ rad. The spatial phase shift now closely matches $\Delta\phi$ such that $|kd - \Delta\phi| = 0.94\pi$ rad. Consequently, the requirements for directional emission are met, and a highly unidirectional 3D scattering distribution is observed (panel c). For wavelengths above ~750 nm, not much of the Fano interference remains as we are far from the Q_y mode. Only the D_y contribution remains, and as expected, one of the dipoles in the model, D_2, disappears.

dx.doi.org/10.1021/nl401877w | Nano Lett. 2013, 13, 3843−3849

Finally, also the directivity can be derived from the two-dipole model:

$$D(\lambda) = \left| 10 \log_{10} \frac{|P_1 + e^{+ikd} P_2|^2}{|P_1 + e^{-ikd} P_2|^2} \right|$$

$D(\lambda)$—plotted in Figure 4d, right graph—reproduces the spectral behavior of the directivity observed in the experiments and as calculated from the simulated far-field projections (Figure 2) very well. The maximum directivity is reached at λ = 710 nm ($P_1/P_2 = 0.95 \approx 1$, $|kd - \Delta\phi| = 0.91\pi$ rad). This is very close to the amplitude matching point (intersection of red and blue curves—circle, panel d), yet shifted slightly toward the phase matching point (intersection of kd and $\Delta\phi - \pi$ curves—circle) at λ = 770 nm. Both the amplitude matching point and phase matching point are red-shifted relative to the extinction resonance. This is expected since both the amplitude and phase matching are conducive to a low net dipole moment which is provided by the destructive interference located at the longer wavelength side of the Fano resonance. The overall scattering cross-section of the antenna is therefore reduced at the maximum directivity. From the two point-dipoles model (panel a) it furthermore follows that varying the spectral distance between the amplitude and phase matching points results in a tunable maximum directivity. Since these points are ultimately determined by the exact distribution of the oscillating charges throughout the Fano resonance, and since these charges are bound by the antenna shape, it can be understood that changing the V-angle of the antenna will affect the consequent achievable directivities, as was indeed observed in Figure 3.

To summarize, we have experimentally investigated the scattering properties of V-shaped metallic nanoantennas. Unidirectional scattering of a plane wave in a direction perpendicular to the incident light direction was observed in FDTD simulations and back focal plane measurements, showing excellent mutual agreement. Tuning of the directivity was experimentally demonstrated by changing the V-angle. An experimental left/right directional gain as large as 15 dB was achieved. In contrast to previous reports on directional side scattering, here the directionality phenomenon has been reduced to the single nanoparticle level. The antenna's reduced structural symmetry was shown to give rise to Fano interference of spectrally, and spatially, overlapping quadrupolar and dipolar LSPR antenna modes. Decomposing the antenna's charge oscillations in two dipole sources of variable amplitude, phase, and spatial separation, illustrated how this Fano interference can result in a tunable directivity that peaks in the resonance flank where the interference is destructive. Other asymmetric particle geometries supporting Fano resonances are expected to exhibit similar directional scattering properties, allowing further optimization. We believe that this concept can give rise to improvements in plasmon-based chemical and biological sensing, as well as surface enhanced spectroscopy. In addition, small ($<\lambda^3/100$) plasmonic directional antennas as these can form a promising base for compact directional emitters and constitute a single-element Yagi-Uda antenna.

■ ASSOCIATED CONTENT

Supporting Information

More details on the BFP setup, BFP image processing, and calculation of the scattering distributions. Experimental spectral tunability data of the V-antenna. Alternative directivity calculations. This material is available free of charge via the Internet at http://pubs.acs.org.

■ AUTHOR INFORMATION

Corresponding Author

*E-mail: Dries.Vercruysse@imec.be; Niels.Verellen@fys.kuleuven.be.

Notes

The authors declare no competing financial interest.

■ ACKNOWLEDGMENTS

D.V. acknowledges the I.W.T. Flanders, and N.V. acknowledges the F.W.O. (Flanders) for financial support. N.V. and V.V.M. are supported by the Methusalem funding by the Flemish Government. S.A.M and Y.S. acknowledge funding from the EPSRC, the Leverhulme trust, and the European Science Foundation. The authors thank Jos Moonens for e-beam assistance and Hector Sanchez for preliminary measurements with the BFP microscopy setup.

■ REFERENCES

(1) Loo, C.; Lowery, A.; Halas, N.; West, J.; Drezek, R. *Nano Lett.* **2005**, *5*, 709−711.
(2) Hu, M.; Chen, J.; Li, Z.-Y.; Au, L.; Hartland, G. V.; Li, X.; Marquez, M.; Xia, Y. *Chem. Soc. Rev.* **2006**, *35*, 1084.
(3) Mayer, K. M.; Hafner, J. H. *Chem. Rev.* **2011**, *111*, 3828−3857.
(4) Atwater, H. A.; Polman, A. *Nat. Mater.* **2010**, *9*, 205−213.
(5) Schuller, J. A.; Barnard, E. S.; Cai, W.; Jun, Y. C.; White, J. S.; Brongersma, M. L. *Nat. Mater.* **2010**, *9*, 193−204.
(6) Niesen, B.; Rand, B. P.; Van Dorpe, P.; Cheyns, D.; Tong, L.; Dmitriev, A.; Heremans, P. *Adv. Energy Mater.* **2012**, *3*, 145−150.
(7) Neutens, P.; Van Dorpe, P.; De Vlaminck, I.; Lagae, L.; Borghs, G. *Nat. Photonics* **2009**, *3*, 283−286.
(8) Lal, S.; Link, S.; Halas, N. J. *Nat. Photonics* **2007**, *1*, 641−648.
(9) Nordlander, P.; Oubre, C.; Prodan, E.; Li, K.; Stockman, M. I. *Nano Lett.* **2004**, *4*, 899−903.
(10) Verellen, N.; Sonnefraud, Y.; Sobhani, H.; Hao, F.; Moshchalkov, V. V.; Van Dorpe, P.; Nordlander, P.; Maier, S. A. *Nano Lett.* **2009**, *9*, 1663−1667.
(11) Luk'yanchuk, B.; Zheludev, N. I.; Maier, S. A.; Halas, N. J.; Nordlander, P.; Giessen, H.; Chong, C. T. *Nat. Mater.* **2010**, *9*, 707−715.
(12) Fan, J. A.; Wu, C.; Bao, K.; Bao, J.; Bardhan, R.; Halas, N. J.; Manoharan, V. N.; Peter, N.; Shvets, G.; Capasso, F. *Science* **2010**, *328*, 1135−1138.
(13) Sonnefraud, Y.; Koh, A. L.; McComb, D. W.; Maier, S. A. *Laser Photonics Rev.* **2012**, *6*, 277−295.
(14) Liu, W.; Miroshnichenko, A. E.; Neshev, D. N.; Kivshar, Y. S. *ACS Nano* **2012**, *6*, 5489−5497.
(15) Fu, Y. H.; Kuznetsov, A. I.; Miroshnichenko, A. E.; Yu, Y. F.; Lukyanchuk, B. *Nat. Commun.* **2013**, *4*, 1527.
(16) Luk'yanchuk, B. S.; Tribelsky, M. I.; Wang, Z. B.; Zhou, Y.; Hong, M. H.; Shi, L. P.; Chong, T. C. *Appl. Phys. A: Mater. Sci.* **2007**, *89*, 259−264.
(17) Mirin, N. A.; Halas, N. J. *Nano Lett.* **2009**, *9*, 1255−1259.
(18) Zhang, Y.; Barhoumi, A.; Lassiter, J. B.; Halas, N. J. *Nano Lett.* **2011**, *11*, 1838−1844.
(19) Van Dorpe, P.; Ye, J. *ACS Nano* **2011**, *9*, 6774−6778.
(20) Curto, A. G.; Volpe, G.; Taminiau, T. H.; Kreuzer, M. P.; Quidant, R.; van Hulst, N. F. *Science* **2010**, *329*, 930−933.
(21) Kosako, T.; Kadoya, Y.; Hofmann, H. F. *Nat. Photonics* **2010**, *4*, 312−315.
(22) Maksymov, I. S.; Staude, I.; Miroshnichenko, A. E.; Kivshar, Y. S. *Nanophotonics* **2012**, *1*, 65−81.
(23) Dregely, D.; Taubert, R.; Dorfmüller, J.; Vogelgesang, R.; Kern, K.; Giessen, H. *Nat. Commun.* **2011**, *2*, 267.

(24) Shegai, T.; Chen, S.; Miljković, V. D.; Zengin, G.; Johansson, P.; Käll, M. *Nat. Commun.* **2011**, *2*, 481.
(25) Shegai, T.; Johansson, P.; Langhammer, C.; Käll, M. *Nano Lett.* **2012**, *12*, 2464−2469.
(26) Pakizeh, T.; Käll, M. *Nano Lett.* **2009**, *9*, 2343−2349.
(27) Li, Z.; Hao, F.; Huang, Y.; Fang, Y.; Nordlander, P.; Xu, H. *Nano Lett.* **2009**, *9*, 4383−4386.
(28) Shegai, T.; Miljković, V. D.; Bao, K.; Xu, H.; Nordlander, P.; Johansson, P.; Käll, M. *Nano Lett.* **2011**, *11*, 706−711.
(29) Pellegrini, G.; Mazzoldi, P.; Mattei, G. *J. Phys. Chem. C* **2012**, *116*, 21536−21546.
(30) Kats, M. A.; Genevet, P.; Aoust, G.; Yu, N.; Blanchard, R.; Aieta, F.; Gaburro, Z.; Capasso, F. *Proc. Natl. Acad. Sci. U.S.A.* **2012**, *109*, 12364−12368.
(31) Aieta, F.; Genevet, P.; Kats, M. A.; Yu, N.; Blanchard, R.; Gaburro, Z.; Capasso, F. *Nano Lett.* **2012**, *12*, 4932−4936.
(32) Sonnefraud, Y.; Kerman, S.; Di Martino, G.; Lei, D. Y.; Maier, S. A. *Opt. Express* **2012**, *20*, 4893−4902.
(33) Verellen, N.; Van Dorpe, P.; Huang, C.; Lodewijks, K.; Vandenbosch, G. A. E.; Lagae, L.; Moshchalkov, V. V. *Nano Lett.* **2011**, *11*, 391−397.
(34) Lumerical Solutions, Inc. http://www.lumerical.com.
(35) Johnson, P. B.; Christy, R. W. *Phys. Rev. B* **1972**, *6*, 4370.
(36) Bohren, C. F.; Huffman, D. R. *Absorption and Scattering of Light by Small Particles*; John Wiley & Sons: New York, 1983.
(37) Khlebtsov, B. N.; Khlebtsov, N. G. *J. Phys. Chem. C* **2007**, *111*, 11516−11527.
(38) Verellen, N.; Van Dorpe, P.; Vercruysse, D.; Vandenbosch, G. A. E.; Moshchalkov, V. V. *Opt. Express* **2011**, *19*, 11034−11051.
(39) López-Tejeira, F.; Paniagua-Domínguez, R.; Rodríguez-Oliveros, R.; Sánchez-Gil, J. A. *New J. Phys.* **2012**, *14*, 023035.
(40) Taminiau, T. H.; Stefani, F. D.; van Hulst, N. F. *Nano Lett.* **2011**, *11*, 1020−1024.

Acknowledgments

Three years passed in no time. During this period of intense work at Imperial College, a vast experience and scientific knowledge have been built.

I would like to thank Prof. Stefan Maier whose guidance and expertise have been paramount throughout the course of my PhD studies. He welcomed me in his group and he has provided the necessary infrastructure, funding and scientific guidance.

A special thank you goes to Dr. Yannick Sonnefraud. He helped me to develop the ability to plan a project systematically, and be efficient. I need to thank him for his guidance, for his help, for his teachings and especially for his friendship.

I am grateful to my collaborators Dr. Mark Tame and Dr. Stephane Kena Cohen. Without their support and their insights, the material presented in this Thesis could never have come into existence.

Thank you to my colleague and friend Vincenzo for our fruitful scientific discussions and for his role of elder brother.

I wish to thank all my colleagues, Binghao, Enrico, Kostas, Roberto, Antonio Fernandez, Sasha, Pablo, Tyler, Nick, Steven who have helped make my time here at Imperial College an enjoyable experience.

I cannot express enough the thankfulness I have for Antonio for his massive support and encouragement during these last years. I need to thank him for our long talks, for our dreams and for his love.

Finally, thanks to my family for their support in this adventure. In particular, I wish to thank my mother for the enormous courage she gave me and my father for his valuable advises.